IMPROVED IMAGING OF BRAIN WHITE MATTER USING DIFFUSION WEIGHTED MAGNETIC RESONANCE IMAGING

By

HA-KYU JEONG

Dissertation

Submitted to the Faculty of the

Graduate School of Vanderbilt University

in partial fulfillment of the requirements

for the degree of

DOCTOR OF PHILOSOPHY

in

Biomedical Engineering

August, 2008

Nashville, Tennessee

Approved:

Professor Adam W. Anderson

Professor Bruce M. Damon

Professor John C. Gore

Professor Mark D. Does

Professor Zhaohua Ding

Copyright © 2008 by Ha-Kyu Jeong
All Rights Reserved

ACKNOWLEDGEMENTS

First of all, I would like to express foremost thanks to my advisor Dr. Adam Anderson. Needless to say, this work would not have been possible without his invaluable advices and supports. He also showed me how to be a nice and good scientist, simultaneously, through his devotion and inspiration to me and others. I would also like to thank all my dissertation committee members Drs. Ding, Does, Damon, and Gore for their support and helpful comments as well as their patience. I am also indebted to many scientists and fellow graduate students in the Vanderbilt Institute of Imaging Science (VUIIS). Having been a trainee in VUIIS requires ardor for imaging science as well as taking an active role as an interactive researcher. As a trainee I feel so lucky having my time in VUIIS during the period of rapid growth under the direction of Dr. John Gore, and, evidently, it has been rewarding and worth while. As a happy debtor, thanks are also due to Dr. Gatenby and Chen who helped in my 7T experiment, and Jay Moore for gladly volunteering to be scanned. I would like to give special thanks to all DTI group members Lori, Ann, Xin, Craig, Qing, Nicole, and others for invaluable discussions and sharing novel ideas, and fellow graduate students Junzhong and Mariam, and Dr. Barros a former post-doctoral fellow at VUIIS whose mind is full of science and who discussed with me mostly non-scientific topics and jokes. Also my heartful appreciations are given to all the current and previous members of NKUMC and pastor Kang who lives in the sincere belief and love of God and humans and also ping-pong. I would never have completed this work if there had not been the love, support and prayers of my family in Korea. Especially, I would like to express my deep appreciation to my wife Si-Hyoung Lee who always believed in me with full support and love and to her American mom Molly Glenn who always prayed for my family and advised with wisdom, though it is not so pleasant for me to have two mother in laws. Finally, I would like to acknowledge the support that I have received during the time I have been at Vanderbilt and the research grant (NIH RO1EB002777). This dissertation is sincerely dedicated to all listed above and any mistakes remaining are my own.

TABLE OF CONTENTS

Page

Chapter

Appendix

LIST OF TABLES

Table Page

LIST OF FIGURES

CHAPTER Ⅰ

OBJECTIVES AND SPECIFIC AIMS

1.1. Objectives

The overall purpose of this study is to characterize and improve methods for imaging brain white matter using diffusion weighted magnetic resonance imaging (DW-MRI). DW-MRI can provide a measure of local tissue microstructure based on the molecular diffusion of water. Recently, however, the major limitations of this imaging technique have been identified. In diffusion tensor MRI (DT-MRI), image noise produces both noise and bias in the estimated tensor, and leads to errors in estimated fiber paths. Moreover the single-tensor model is inappropriate in regions with complicated (e.g., non-parallel) fiber structure. High angular resolution diffusion imaging (HARDI) methods, e.g., Gaussian mixture, q-ball imaging (QBI), diffusion spectrum imaging (DSI), spherical deconvolution (SD) etc., have been proposed as alternative tools for resolving multiple fiber structure within a voxel. At low SNR, however, fiber information from HARDI becomes unreliable. Also, none of the methods can provide estimates of the intrinsic diffusion properties of more than one fiber.

This dissertation presents experimental and theoretical studies of uncertainty in fiber orientation using DT-MRI. It also proposes methods for estimation of intrinsic diffusion properties, as well as reliable fiber orientation distribution (FOD) functions using HARDI. These methods are then applied to the environment with ultra high B0 field strength for improved imaging of brain white matter for human and/or non-human primates. Following specific aims describe this study in detail.

1.2. Specific Aims

1.2.1. Specific aim 1: Characterization of fiber directional uncertainty

The directional uncertainty of a local fiber is analyzed by constructing the cone of uncertainty (CU) using bootstrap analysis and perturbation theory. The amount of uncertainty, which defines the cone angle, is quantified as a function of image SNR, tensor anisotropy and eigenvalue contrast. Also the effect of gradient encoding scheme is studied, focusing on the coherence angle which describes the angular difference between the second (third) eigenvector of a diffusion tensor and the major (minor) axis of fiber directional dispersion.

1.2.2. Specific aim 2: Characterization of the properties of multiple fibers

1.2.2.1. Robust estimation of multiple fiber orientation distributions

In the presence of noise, conventional pseudoinverse calculation often produces inaccurate fiber orientations with spurious or smeared peaks in the FOD function. This problem can be described as ill-posed, and the use of regularization can provide robust and reliable solutions. In this study, various regularization methods have been studied using singular value decomposition (SVD) under various conditions, such as number of fibers, SNR, expansion order, diffusion weighting gradient direction, *b*-value, separation angle between fibers and side constraints to determine optimal methods for accurate FOD representation.

1.2.2.2. Estimation of multiple fiber intrinsic diffusion properties

The requirements for accurate determination of the diffusion properties of multiple fibers are established. Various imaging parameters are simulated to determine the optimal imaging conditions, and the diffusion properties are found by searching over the property space (volume fraction and radial diffusivity). Individual fiber FODs are compared in the regions of known fiber structures using simulation and experiment.

1.2.3. Specific aim 3: Application to high field imaging

At ultra high field strength, e.g., 7 Tesla, there is a significant B0 inhomogeneity artifact which spatially distorts DW and non-DW echo planar images. The correction for the B0 inhomogeneity is done by acquiring a ΔB0 fieldmap and then calculating the voxel displacement map. The feasibility of DW-MRI in a human 7 Tesla scanner is verified by forming FA and FOD maps, using the optimized methods studied in specific aim 2.

CHAPTER Ⅱ

BACKGROUND AND SIGNIFICANCE

2.1. Diffusion weighted magnetic resonance imaging

In 1828, Robert Brown observed the random, thermal motion of microscopic particles in a fluid medium. Molecular diffusion, a manifestation of what is now known as Brownian motion, is described by Fick's first law, relating the spatial gradient of the concentration of a particle to a flux **J** [1],

$$\mathbf{J} = -D\nabla' P(\mathbf{r} \mid \mathbf{r}', t) . \tag{2.1}$$

Here, the diffusion propagator $P(\mathbf{r} \mid \mathbf{r}', t)$ gives the probability of a spin moving from position $\mathbf{r}$ to $\mathbf{r}'$ during the diffusion time t [2,3] and D is the molecular self-diffusion coefficient. With the application of the continuity theorem,

$$\nabla' \cdot \mathbf{J} = -\frac{\partial P}{\partial t} , \tag{2.2}$$

$$\frac{\partial P}{\partial t} = D\nabla'^2 P , \tag{2.3}$$

one finds Equation (2.3) known as Fick's second law. The self-diffusion coefficient is defined as the diffusion coefficient of a species when there is no chemical potential gradient [4]. Fick's law describes the likelihood of finding a particle in a specific place at a certain time.

If there are no barriers to diffusion (i.e., diffusion is not restricted or hindered), the diffusion process is said to be free and the solution of (2.3) has a Gaussian dependence on displacement,

$$P(\mathbf{R},t) = \left(4\pi Dt\right)^{-3/2} \exp\left\{-\mathbf{R}^2 / 4Dt\right\}, \tag{2.4}$$

here $\mathbf{R} = (\mathbf{r}' - \mathbf{r})$, is the dynamic displacement [2]. The function P provides the average probability for any particle to have a dynamic displacement $\mathbf{R}$ over a time t and is defined as the 'propagator' averaged over all initial positions,

$$P(\mathbf{R},t) = \int P(\mathbf{r} \mid \mathbf{r}',t)\rho(\mathbf{r})d\mathbf{r}. \tag{2.5}$$

For the case of free self-diffusion, $P(\mathbf{r} \mid \mathbf{r}',t)$ is only a function of **R**, and the average propagator in (2.5) is common to all molecules in the environment. The average propagator allows us to infer the underlying microgeometry of a structure [5].

In the nuclear magnetic resonance (NMR) experiment we can measure the movement of water molecules by applying a spatial label to the nuclei at one instant of time, and then measure the shift of the label at a later time in order to deduce the molecules' movement. One simple labeling scheme is to apply a pair of bipolar gradient pulses (one positive and one negative) to dephase then rephase spins as in Figure 2.1.

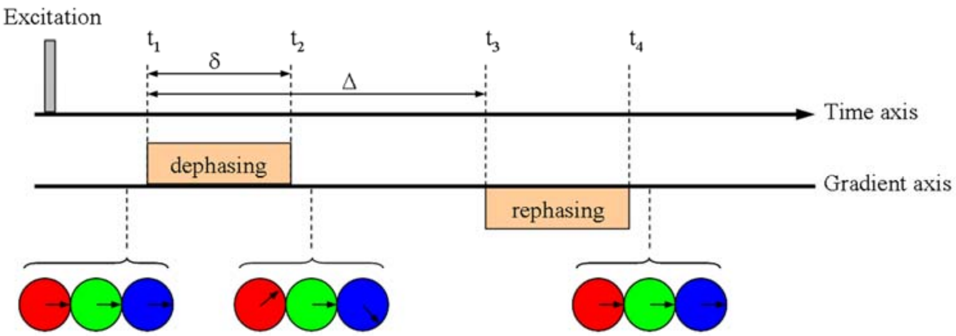

Figure 2.1. An example of a dephase-rephase experiment using bipolar gradient pulses. Three circles and an arrow inside each circle indicate the phase of the NMR signal at different positions over a sample.

In this experiment, however, the spin motion due to diffusion and flow generates different outcomes. Coherent motions such as flow or bulk motions of the subject provide a perfect rephasing with no loss of the NMR signal but a shift of the signal phase. If spins move by incoherent motion, say, diffusion, between the first and the second gradients, then the phase of the spin doesn't return to the original orientation giving loss of the signal. Therefore, basically the coherent and incoherent motion can be distinguished in the NMR diffusion experiment. However, coherent motion can lead to signal loss and interfere with the diffusion measurement when the flow occurs in multiple orientations (e.g., network structure of capillaries) within a voxel. In most *in vivo* experiments, however, water molecular movement by blood flow is much faster than that by diffusion, and the signal from blood water (which composes 5% of water in the brain) dephases almost completely

[6].

One drawback of using bipolar gradient pulses is the significant signal loss due to T2* decay between the two gradient pulses. Therefore it is more common to use spin-echo sequences in which the signal decays by T2 (in here T2≥T2*) during diffusion weighting. The spin-echo experiment including the effects of diffusion on the echo has been described by Hahn [7] and Carr et al. [8]. The pulsed gradient spin-echo (PGSE) shown in Figure 2.2 was pioneered by Stejskal and Tanner [9] and it is now the classical method for the measurement of diffusion using NMR.

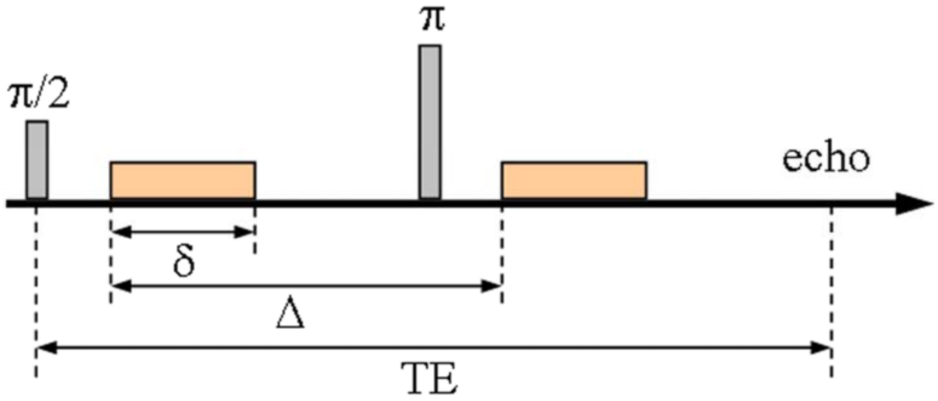

Figure 2.2. A PGSE sequence diagram. The pulse sequence excites the spin system with a π/2 pulse, encodes the spin position with a constant magnetic field gradient of duration δ, inverts the phase of spins with a π pulse, applies the same gradient with the same duration at the time Δ after the first gradient pulse, and then the echo signal is acquired at the time TE.

In their study, Stejskal and Tanner used the Bloch-Torrey equation [10], i.e., Bloch equation [11] including diffusion terms (2.6) to relate the spin echo amplitude, $A(TE)$, to the diffusion coefficient:

$$\begin{aligned}\ln\left(\frac{A(TE)}{A(0)}\right) &= -\gamma^2\int_0^{TE} D\cdot\left[\mathbf{F}(t)+(\xi-1)\mathbf{f}\right]^2 dt \\ &= -\gamma^2\delta^2G^2\left(\Delta-\frac{\delta}{3}\right)\cdot D \qquad , \\ &= -b\cdot D\end{aligned} \tag{2.6}$$

here $\mathbf{F}(t)=\int_0^t \mathbf{G}(t')\,dt'$, $\mathbf{f}=\mathbf{F}\left(\frac{TE}{2}\right)$, $\xi = 1$ ($0 < t < TE/2$) and $\xi = -1$ ($t > TE/2$) and $A(t)$ is the echo amplitude at time t after a 90 degree excitation pulse.

Considering that the NMR signal depends on the spin phase distribution, we can write the signal using (2.4), e.g., along one dimension [6],

$$\begin{aligned} S &= S_0\int_x P(x,t)\Phi(x)dx \\ &= S_0\left(\frac{1}{\sqrt{4\pi Dt}}\int_x e^{-x^2/4Dt}e^{i\gamma G\delta x}dx\right)^{,} \end{aligned} \tag{2.7}$$

here $\Phi(x)$ is the phase term for spins displaced by x and $P(x,t)$ is the population of water at position x and diffusion time t. Solving (2.7) becomes,

$$\begin{aligned} &\frac{S_0}{\sqrt{4\pi Dt}}\int_x e^{-x^2/4Dt}e^{i\gamma G\delta x}dx \\ &= \frac{S_0}{\sqrt{4\pi Dt}}\left(\int_x e^{-x^2/4Dt}\cos(\gamma G\delta x)dx + i\int_x e^{-x^2/4Dt}\sin(\gamma G\delta x)dx\right). \\ &= S_0 e^{-\gamma^2G^2\delta^2Dt} \end{aligned} \tag{2.8}$$

However (2.8) is not valid when the diffusion gradient G is a function of time. Let’s consider a simple diffusion weighting sequence as shown in Figure 2.1, and then (2.8) is,

$$\ln\left(\frac{S}{S_0}\right) = -\gamma^2 D \int_{t_1}^{t_4} \left(\int_0^t G(t')dt'\right)^2 dt . \qquad (2.9)$$

In this sequence, the time period t_1-t_4 is divided into discrete time segments and $\int_0^t G(t')dt'$ in (2.9) becomes

$$\int_0^t G(t')dt' = \begin{cases} Gt, & t_1 \le t \le t_2 \\ G\delta, & t_2 \le t \le t_3 \\ G\delta - G(t-t_3), & t_3 \le t \le t_4 \end{cases} .$$

Hence (2.9) is,

$$\ln\left(\frac{S}{S_0}\right) = -\gamma^2 D \left\{ \int_{t_1}^{t_2} G^2 t^2 dt + \int_{t_2}^{t_3} G^2 \delta^2 dt + \int_{t_3}^{t_4} \left[G\delta - G(t-t_3)\right]^2 dt \right\} . \qquad (2.10)$$

Letting $t_1 = 0$, $t_2 = \delta$, $t_3 = \Delta$ and $t_4 = \delta+\Delta$ as shown in Figure 2.1 and solving (2.10) gives,

$$\ln\left(\frac{S}{S_0}\right) = -\gamma^2 G^2 \delta^2 \left(\Delta - \frac{\delta}{3}\right) \cdot D . \qquad (2.11)$$

The signal attenuation due to diffusion in (2.11) is the same as in (2.6). This expression explicitly relates NMR signal attenuation and the self-diffusion coefficient in the case of Gaussian diffusion. The final result in (2.6) or (2.11) is also based on the assumption that there is no diffusion barrier or hindrance - an assumption which is easily violated in most of the *in vivo* diffusion measurements of ‘restricted’ or ‘anisotropic’ diffusion [12-15]. The primary sources of apparent anisotropic diffusion are susceptibility variations [15] and ordered cellular structures [16-18], otherwise they are restricted mostly due to cellular membranes.

Assuming that the effect of susceptibility-induced gradients can be ignored (because it is negligible or can be canceled by appropriate experimental setup), the water molecular diffusion measured *in vivo* reflects the presence of spatially ordered macromolecular, membranous, or cellular structures which can be heterogeneous on microscopic length scales but homogeneous and anisotropic on a macroscopic scale (i.e., in a voxel) [19,20]. To this end the effective self-diffusion tensor (or simply the diffusion tensor) has been introduced to generalize (2.6) [19-22] leading to a simple expression as in (2.12)

$$\ln\left(\frac{A(TE)}{A(0)}\right) = -\sum_{i=1}^{3}\sum_{j=1}^{3} b_{ij}D_{ij} = -\mathbf{b}:\mathbf{D}, \tag{2.12}$$

here : is the generalized dot product and **b** and **D** are symmetric matrices. Equation (2.12) suggests that we can estimate the signal attenuation mediated by each of the diagonal and off-diagonal components of **D** by applying the diffusion weighting gradient in various directions. To fully construct the diffusion tensor with diagonal as well as off-diagonal terms, at least six non-colinear diffusion weighting directions are required [23] using optimized imaging parameters [24] or fitting algorithms [25] when necessary.

The diagonal and off-diagonal elements are essential in determining the orientation, shape and size of the diffusion ellipsoid which characterizes the molecular diffusion in anisotropic media. By diagonalizing the diffusion tensor we can get three mutually perpendicular directions (principal directions) and diffusivities along the preferred directions (principal diffusivities).

The most powerful and useful information that can be extracted from the diffusion tensor is the dimensionless diffusion anisotropy, i.e., fractional anisotropy (FA) and relative anisotropy (RA) [26] and axonal fiber tract trajectory [27-30]. The ability to make these measurements opened a new window on many issues of brain connectivity in normal subjects [31], various brain dysfunctions such as cancer, multiple sclerosis and schizophrenia [32] and even outside of the brain such as heart [33], skeletal muscle [34,35], kidney [36] and the whole body [37].

2.2. Uncertainty in the diffusion tensor model

Diffusion tensor MRI (DT-MRI or DTI) can provide microstructural information on a tissue based on water molecular diffusion *in vivo* [19,20,23,26]. This directional information can be used to estimate the local direction of brain fiber bundles in order to infer axonal connectivity [29]. The principal eigenvector of a diffusion tensor, $\mathbf{v}_1$, is considered to be parallel to the local fiber direction. However, image noise produces perturbations in the tensor field and causes errors in the estimated diffusion anisotropy [38-40] and fiber path [41,42].

The dependence of $\mathbf{v}_1$ on tensor errors has been found from first order perturbation theory [41,43-45] or simple error analysis [46]. With this approach the $\mathbf{v}_1$ error ($\delta\mathbf{v}_1$) in the $\mathbf{v}_2$ (second eigenvector) and $\mathbf{v}_3$ (third eigenvector) directions can be expressed as,

$$\mathbf{v}_2^{\mathbf{T}} \cdot \delta\mathbf{v}_1 = \frac{\mathbf{v}_2^{\mathbf{T}} \cdot \delta\mathbf{D} \cdot \mathbf{v}_1}{\lambda_1 - \lambda_2}, \tag{2.13}$$

$$\mathbf{v}_3^{\mathbf{T}} \cdot \delta\mathbf{v}_1 = \frac{\mathbf{v}_3^{\mathbf{T}} \cdot \delta\mathbf{D} \cdot \mathbf{v}_1}{\lambda_1 - \lambda_3}, \tag{2.14}$$

corresponding to a given tensor error, $\delta\mathbf{D}$. This error in $\mathbf{v}_1$ can be more easily understood in the $\{\mathbf{v}_2, \mathbf{v}_3\}$ plane. The covariance matrix, $\mathbf{\Sigma}_{\mathbf{v}_1}$ as in (2.15), for $\mathbf{v}_1$ in the $\{\mathbf{v}_2, \mathbf{v}_3\}$ plane gives the variance of $\delta\mathbf{v}_1$ along $\mathbf{v}_2$ and $\mathbf{v}_3$ on the diagonal and the covariance of these components in the off-diagonal elements:

$$\mathbf{\Sigma}_{\mathbf{v}_1} = \begin{bmatrix} \dfrac{\left\langle \left(\mathbf{v}_2^{\mathbf{T}} \cdot \delta\mathbf{D} \cdot \mathbf{v}_1\right)^2 \right\rangle}{\left(\lambda_1 - \lambda_2\right)^2} & \dfrac{\left\langle \left(\mathbf{v}_2^{\mathbf{T}} \cdot \delta\mathbf{D} \cdot \mathbf{v}_1\right)\left(\mathbf{v}_3^{\mathbf{T}} \cdot \delta\mathbf{D} \cdot \mathbf{v}_1\right) \right\rangle}{\left(\lambda_1 - \lambda_2\right)\left(\lambda_1 - \lambda_3\right)} \\ \dfrac{\left\langle \left(\mathbf{v}_2^{\mathbf{T}} \cdot \delta\mathbf{D} \cdot \mathbf{v}_1\right)\left(\mathbf{v}_3^{\mathbf{T}} \cdot \delta\mathbf{D} \cdot \mathbf{v}_1\right) \right\rangle}{\left(\lambda_1 - \lambda_2\right)\left(\lambda_1 - \lambda_3\right)} & \dfrac{\left\langle \left(\mathbf{v}_3^{\mathbf{T}} \cdot \delta\mathbf{D} \cdot \mathbf{v}_1\right)^2 \right\rangle}{\left(\lambda_1 - \lambda_3\right)^2} \end{bmatrix}. \tag{2.15}$$

using (2.13) and (2.14).

Diagonalizing this covariance matrix provides the principal components of $\mathbf{v}_1$ variation, i.e., the directional uncertainty, on the plane perpendicular to the local direction of fiber propagation [47], and this has been characterized by the ‘cone of uncertainty’ [43,48]. Lazar et al. [49,50], Koay et al. [45] and Jeong et al. [47] showed that errors in MR tractography typically have an elliptical distribution, and noted that an elliptical CU is expected in voxels that lack axially symmetric diffusion. Figure 2.3 demonstrates the construction scheme of the CU as in [47].

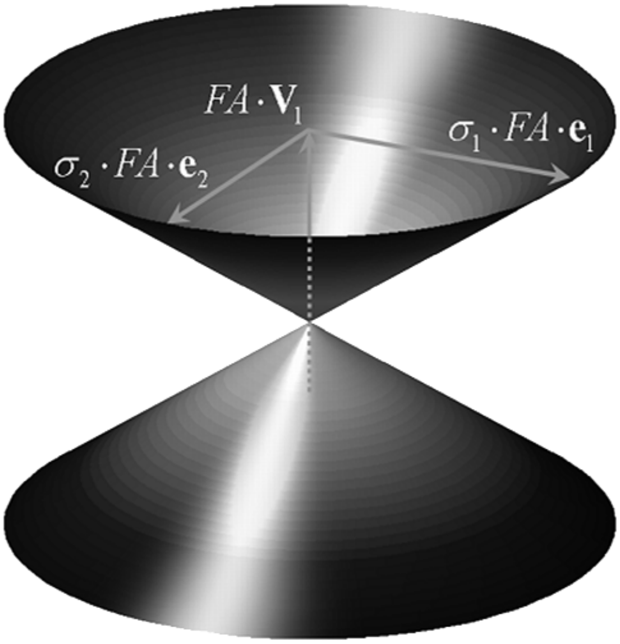

Figure 2.3. An example of a construction scheme of the CU. The variation of $\mathbf{v}_1$ is projected onto the perpendicular plane. The major and minor axes of the CU are represented with the error (σ_j) in the principal direction (e_j), where j = 1,2. The size of cone is scaled by FA.

Lazar et al. [49,50] measured the dispersion of fiber paths in a plane perpendicular to the local fiber axis at some distance from the seed points using the bootstrap method [51]. By randomly selecting individual diffusion weighted images with replacement from a set of measurements, the bootstrap estimates of a given statistic can be used to obtain a measure of uncertainty [48,52]. With this technique, they noted a strong correlation between the direction of the greatest dispersion of fiber tracks and the second eigenvector of the tensor. However there has been no general explanation for this observation, and few experimental and theoretical studies on the properties of the CU.

The characterization of the CU is critical for understanding and improving fiber tractography. Some of the key properties are fiber directional uncertainty, symmetry and multivariate normality of principal eigenvector errors and the dependence of the CU on image noise, diffusion anisotropy and eigenvalue contrast. Only a few studies have been published on the properties of the CU and the reduction of image noise, using methods such as time domain signal averaging [40,41] or anisotropic smoothing [53-55].

2.3. Beyond the diffusion tensor

2.3.1. Pitfalls in the diffusion tensor model

Although DTI has been remarkably successful in detecting subtle changes in white matter tissue structure, the tensor model based on the assumption of Gaussian diffusion is inappropriate within complex human tissues [20,56-58]. The presence of multiple fiber directions within a single imaging voxel, i.e., a partial volume effect, cannot be characterized by a single tensor because a tensor possesses only a single orientational maximum, i.e., it describes a single fiber diffusion [28-30,59-67]. This is particularly true for DT-MRI studies that use EPI techniques with relatively large voxels, about 1.5-5.0 mm on a side [59].

2.3.2. High angular resolution diffusion imaging (HARDI) with Gaussian mixtures

A new approach proposed by Tuch et al. [64,65] uses high angular resolution diffusion imaging (HARDI) with large *b*-values in order to detect more accurately variations in diffusion along different directions. At the lower *b*-values conventionally employed by DT-MRI, the signal contrast is insufficient between the fast diffusion component of one fiber and slow diffusion component of another fiber to effectively resolve the two fibers [59,64,65]. To resolve multiple fiber orientations in the presence of intravoxel orientational heterogeneity (IVOH), the diffusion signal was modeled as arising from a discrete mixture of Gaussian diffusion processes as follows [64].

The signal from a single compartment, assuming Gaussian diffusion, is given by

(2.16)

$$E(\mathbf{q}_k) = e^{-\mathbf{q}_k{}^T \mathbf{D} \mathbf{q}_k \tau}, \tag{2.16}$$

where $E(\mathbf{q}_k)$ is the normalized diffusion signal magnitude for the diffusion gradient wave vector $\mathbf{q}_k = \gamma\delta\mathbf{g}_k$, γ is the gyromagnetic ratio, δ is the diffusion gradient duration, $\mathbf{g}_k$ is the k$^{\text{th}}$ diffusion gradient, τ is the effective diffusion time and $\mathbf{D}$ is the diffusion tensor. The Gaussian mixture model is based on the following assumptions: 1) the region with IVOH consists of discrete homogeneous compartments; 2) each compartment has Gaussian diffusion described by a tensor; 3) exchange between the compartments is very slow [64]. Then the diffusion weighted signal can be expressed as a finite mixture of Gaussians as in (2.17),

$$E(\mathbf{q}_k) = \sum_i f_i e^{-\mathbf{q}_k{}^T \mathbf{D}_i \mathbf{q}_k \tau}. \tag{2.17}$$

However, *a priori* information about the number of diffusion compartments and intrinsic diffusion properties, e.g., eigenvalues for each compartment, is critical in this mixture model, which has been impossible to obtain using other methods.

2.3.3. Diffusion spectrum imaging (DSI)

This high angular resolution sampling scheme was extended by Wedeen et al. [66,68] to the central volume of 3D q-space. This method, referred to as diffusion spectrum imaging (DSI), can be used to infer the distribution of fiber orientations.

However the DSI technique requires long acquisition times and strong magnetic field gradients using, for example, 515 q-encoding steps [68].

2.3.4. q-Ball imaging (QBI)

An alternative method by Tuch et al. [69] requires samples only on a spherical shell in q space. The method, named q-ball imaging (QBI), characterizes the angular structure of tissue with a diffusion orientation distribution function (ODF), which is defined as the spherical Radon transform of diffusion weighted signal [69,70]. The ODF gives the probability for a spin to diffuse any distance in the direction $\mathbf{u}$ at the experimental diffusion time τ [69]. The ODF, ψ, can be simply represented using the spherical Radon transform of the diffusion weighted signal, known as the Funk-Radon transform [69,70], as in (2.18)

$$\psi(\mathbf{u}) = \int_{\mathbf{q}\perp\mathbf{u}} E(\mathbf{q})\, d\mathbf{q}, \tag{2.18}$$

where $\mathbf{u}$ is the diffusion direction of interest. In this study, relatively low *b*-value (4000 s/mm^2) and 252 gradient samples were used to reconstruct the ODF. Crossing fiber structures, e.g., Meyer’s loop, which were impossible to represent using DT-MRI, were clearly resolved [70].

2.3.5. Spherical harmonic decomposition (SHD)

Frank [57,62] and Alexander [71] used spherical harmonic decomposition (SHD) to represent the measured apparent diffusion coefficient (ADC) as a function of orientation. Considering the general case of HARD measurements for a voxel with unknown fiber structure, the measured ADC, $D(\theta,\phi)$, is a (symmetric) real function and the spherical harmonics form a complete orthonormal basis on a sphere. Hence, the function can be expanded by Laplace series [57] as in (2.19)

$$D(\theta,\phi)=\sum_{l=0}^{\infty}\sum_{m=-l}^{l} d_{lm}Y_{lm}(\theta,\phi)\,, \tag{2.19}$$

and the coefficient d_l^m is determined using the orthogonality condition as

$$\int_0^{2\pi}\int_0^{\pi} Y_{lm}(\theta,\phi)Y_{l'm'}{}^{*}(\theta,\phi)\sin(\theta)d\theta d\phi=\delta_{ll'}\delta_{mm'}\,. \tag{2.20}$$

The coefficients d_l^m, which are the spherical harmonic transform (SHT) of $D(\theta,\phi)$, are given by

$$d_{lm}=\int_0^{2\pi}\int_0^{\pi} D(\theta,\phi)Y_{lm}{}^{*}(\theta,\phi)\sin(\theta)d\theta d\phi\,. \tag{2.21}$$

Using the SHT, the ADC profile can be represented using SHD as shown in (2.19). The SHD calculates ADC components up to a user-defined order l (maximum expansion order, $l_{\max}$), for all the $2l+1$ values of the degree m associated with each l ($m = -l, -l+1, \ldots 0, \ldots l-1, l$) [57,71]. However, the local diffusion, in general, including the magnitude and orientation can be described by a sum of spherical harmonics of even order, i.e. $l = 0, 2,$

4, ... The order $l_{\max}$ required to characterize the diffusion in a voxel with multiple fibers depends on the relative orientation of the fibers [57]. This means that for more closely aligned fibers, higher order l will be required. Figure 2.4 shows the results of a simulation of the contributions to ADC from the different orders l of the SHD as shown in [57]. It shows that the SHD of ADC contains contributions from the spherical harmonic components at various orders of l depending on the fiber architecture.

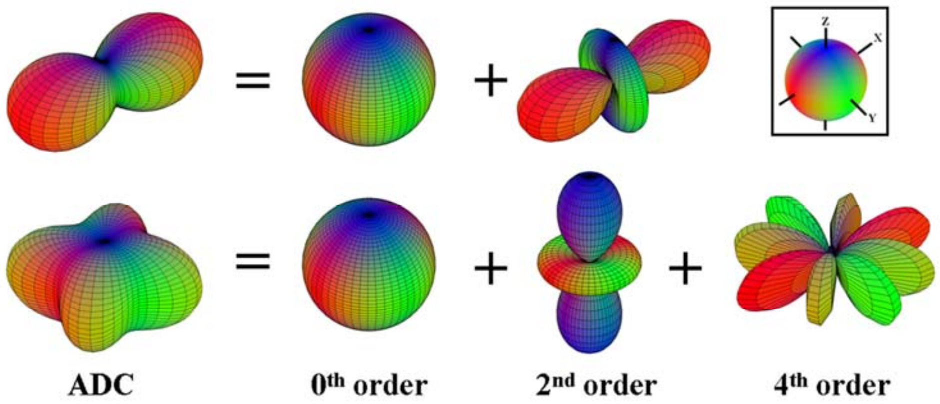

Figure 2.4. The single fiber ADC contains contributions from $l = 0$ (sphere) and $l = 2$ spherical harmonic components (upper row). The two fiber ADC in 90 degrees has an $l = 4$ component as well as $l = 0$ and $l = 2$ (lower row). The fiber directional colormap onto a unit sphere is shown in the upper right corner with coordinate axes.

2.3.5.1. Maximum expansion order using SHD

Alexander et al. [71] showed typical ADC profiles from each of three regions, e.g., pons, optic radiation and corona radiata, with the order $l_{\max} = 0, 2, 4, 6$ and 8. Each region has crossing or clusters of fibers, e.g., right-left and inferior-superior in the pons, anterior-posterior and right-left in the optic radiation and large mixing fiber clusters in the corona radiata. They demonstrated that there was a significant difference between the $l_{\max} = 2$ and $l_{\max} = 4$ models indicating significant non-Gaussian diffusion. At order $l_{\max}$ greater than 4, the overall ADC profile does not change significantly, and just the effect of noise is increased [71]. This observation illustrates the importance of choosing an appropriate value for $l_{\max}$.

More elaborate simulations related to this subject were done by Hess et al. [72] for QBI reconstruction using spherical harmonics. In this simulation, a large number of measurements (n = 282) and 1000 uniformly distributed random orientations for each fiber (up to three fibers) were used to show the contribution of $l_{\max}$ by calculating the fractional power spectrum using spherical harmonic coefficients of HARDI signal with orders up to $l_{\max} = 10$ [72]. In the results, the fractional spectral energy was concentrated at lower angular frequencies, and hence accurate reconstruction of the ODF was possible using relatively small values of $l_{\max}$. With b-value of 3000 s/mm^2, the harmonics up to order $l_{\max} = 4$ represent greater than 99.3 % of the spectral energy of the series for all three synthetic fiber architectures [72]. As higher b-values are used, such as 5000 and 7000 s/mm^2, the fractional total energy contributed by harmonic orders up to $l_{\max} = 4$

decreases to 96.9 % and 92.9 %, respectively [72]. Although the order up to 4 contains most of the energy for up to three fiber structures, higher order is required for more closely aligned fibers, in general [57].

2.3.6. Spherical deconvolution (SD) method

It is generally assumed that the peak in the spin displacement profile corresponds to the direction of a fiber population, but the relationship between spin displacement and fiber orientation has not yet been fully explored [73]. Anderson and Ding [60] and Tournier et al. [73] suggested a method that is able to estimate directly the distribution of fiber orientations within a voxel from the HARDI signal using the spherical deconvolution (SD) technique. This is based on the assumptions that there is negligible exchange between distinct fiber bundles and the diffusion characteristics of all fiber populations in the brain [73] or within a voxel [60] are identical. The diffusion weighted signal can be expressed as the convolution over the unit sphere of the response function $R(\theta)$ with a fiber orientation distribution (FOD) function $F(\theta,\phi)$ as in (2.22)

$$S(\theta,\phi) = R(\theta) \otimes F(\theta,\phi)\,. \tag{2.22}$$

Figure 2.5 shows a simple 2-D illustration of the deconvolution method for a voxel with two fiber bundles with distinct orientations and volume fractions as shown in [73].

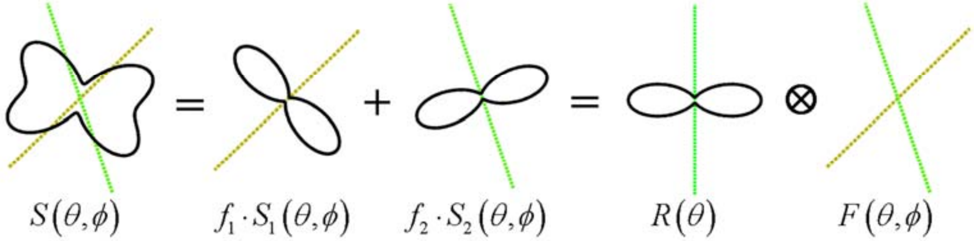

Figure 2.5. The measured DW signal $S(\theta,\phi)$ is the sum of the individual fiber's (dotted line) attenuation profile (continuous line) weighted by its volume fraction, $f_j\, S_j(\theta,\phi)$, $j=1,2$. This can be expressed as a convolution over a unit sphere of an axially symmetric response function $R(\theta)$, giving the signal attenuation for a single fiber population with a fiber orientation distribution function $F(\theta,\phi)$, here $F(\theta,\phi)$ is the sum of two delta functions.

The measured DW signal is the sum of each fiber population's characteristic attenuation profile weighted by its respective volume fraction. This can be represented as a convolution of a single fiber response function with the FOD function as shown in Figure 2.5 [73]. Using spherical harmonics, the measured DW signal can be expressed as (2.23)

$$s_{lm} = r_l\, f_{lm}, \tag{2.23}$$

here, s_{lm}, r_l and f_{lm} are spherical harmonic coefficients of the DW signal, response function and FOD function, respectively. In this method, the response function was found directly from data by measuring the DW signal profile in regions likely to contain a single and coherently oriented fiber population, i.e., where diffusion anisotropy is high.

2.3.7. Fiber orientation estimated using continuous axially symmetric tensors method

The SD method proposed by Anderson and Ding [60] and Anderson [74] provides more information on fiber structure than the other SD techniques. The new method, named fiber orientation estimated using continuous axially symmetric tensors (FORECAST), provides an analytic expression for the response function using the assumption that each fiber bundle has axially symmetric diffusion and shared mean and radial diffusivity within a voxel. This model uses a spherical harmonic expansion of the DW signal and FOD as in (2.24) and (2.25)

$$S(\theta,\phi)=\sum_{l=0}^{\infty}\sum_{m=-l}^{l} s_{lm}Y_{lm}(\theta,\phi)\,, \tag{2.24}$$

$$P(\theta,\phi)=\sum_{l=0}^{\infty}\sum_{m=-l}^{l} p_{lm}Y_{lm}(\theta,\phi)\,. \tag{2.25}$$

Spherical harmonic coefficients for the above functions can be obtained using the relationship in (2.21). The relationship between the DW signal and FOD can be expressed similarly to (2.23) as in (2.26)-(2.28)

$$s_{lm}=S_0\cdot c_l\cdot p_{lm}\,, \tag{2.26}$$

here

$$c_l\equiv\frac{4\pi}{2l+1}e^{-b\lambda_\perp}A_l\,, \tag{2.27}$$

$$A_l=\frac{2l+1}{2}\int_{-1}^{1}e^{-3b(\lambda_{avg}-\lambda_\perp)\cos^2\alpha}P_l(\cos\alpha)d(\cos\alpha)\,. \tag{2.28}$$

In (2.26)-(2.28), S_0 is the non-DW signal, $\lambda_\perp$ is the radial diffusivity and α is the measurement angle relative to a fiber axis. This method successfully demonstrated that the FOD measurement was possible at relatively low *b*-value (1480 s/mm^2) with much lower angular resolution (92 directions) for the FOD than other methods. In this study, two representative voxels were chosen, one in the corpus callosum and the other at the junction of fronto-occipital fasciculus and lateral fibers, and the FORECAST FOD function, FORECAST ODF, QBI ODF, SHD of ADC and single tensor model were displayed using the *b*-value of 1480 s/mm^2, 92 diffusion encoding directions and 4th order expansion [74]. It clearly showed that the FORECAST FOD generated higher angular resolution for the fibers than the other methods. The FORECAST, QBI, and DSI produce very similar ODFs, although they are not identical [74,75].

2.4. Optimal representation of complex fiber structures

The SD method [73] has been widely used to characterize multiple fiber orientations within a single voxel, whereas the diffusion tensor imaging method cannot. However, the reliable estimation of the FOD function is difficult in the presence of noise in the DW-MRI data. Noise results in spurious peaks or lower angular resolution in the FOD. Recently, low-pass filtering [73], minimum entropy [76], minimizing the magnitude of negative peaks [77] and super-resolved spherical deconvolution [78] have been suggested for more reliable estimation of the FOD. However, those methods require *a priori* information about the filter factors [73], regularization parameter [77,78] or a nonlinear optimization [76] which may take relatively large amounts of time. Sakaie et al. [79] recently presented the combined use of the generalized cross validation (GCV) with damped generalized singular value decomposition (DGSVD) for the objective determination of the regularization parameter and robust estimation of the FOD without *a priori* information or user interaction. In their study, two voxels in gray and white matter with crossing fibers were chosen, and FODs were compared using regularization and low-pass filtering. The FOD plot with the regularization shows a nearly uniform sphere representing isotropic diffusion in the gray matter, but that from the low-pass filtering shows an isotropic arrangement of many sharp peaks for the same voxel. For the voxel with crossing fibers, the two results show similar FOD shape.

However, comparisons of various regularization methods and combined side constraints are still required for optimized and robust representation of the FOD. Hansen [80] reviewed a large class of regularization methods and provided a software package which is readily available in MATLAB (Mathworks, Natick, MA).

2.5. Measurement of fiber intrinsic diffusion properties

Although HARDI methods can identify multiple fiber directions, they do not generally provide information about the intrinsic diffusion properties of any of the fibers, and estimates of those properties (such as radial and parallel diffusivities and/or volume fraction) within a single voxel have not been studied extensively. Alternative models have been suggested using multi-component models [81-85], such as two (fast and slow) diffusion compartments, and two-tensor models using six [86,87] or higher [64] non-collinear diffusion gradient directions. However those methods provide only limited information among many diffusion properties.

Tournier et al [73] showed the possibility of estimating volume fraction of a known number of fiber compartments, e.g., two compartments using the SD method within a voxel from HARDI data. Jeong et al. [88] suggested a method for estimating the radial diffusivity and volume fraction of individual fiber bundles in voxels with known two crossing fiber structures, e.g., the cingulum and corpus callosum. Though there have not been many studies of the fiber-specific method, this approach will be helpful in explaining microscopic changes of fiber bundles within a single voxel.

2.6. Application to high field MRI data

Seven Tesla imaging systems have been recently used to demonstrate the feasibility of high field DT-MRI and HARDI for improved visualization of white matter anatomy [89-92]. In a QBI experiment performed at 7 Tesla with higher order shimming and parallel imaging, typical echo planar imaging (EPI) distortions in the anterior and posterior regions of the supratentorial brain were not severe generally and were negligible in the center [92]. However, it is well known that there are increased artifacts from B0 and B1 inhomogeneity and susceptibility at high field strengths. No other reconstruction methods, e.g., FORECAST, have been published or optimized for use at high field, nor have these studies fully addressed the correction of artifacts.

2.6.1. B0 field inhomogeneity correction

The correction of B0 inhomogeneity artifact using the reverse gradient method was suggested by Chang et al. [93] using spin-warp images and applied to EPI data [94,95] and EPI DTI data [96]. This method adopts two separate acquisitions of MRI data using forward and reverse gradients (e.g., using anterior-posterior and posterior-anterior phase encoding directions for brain EPI acquisition). When voxel dimensions are similar in all imaging axes, the slice selective gradient (G_z) is usually several times larger than either the frequency encoding (G_x) or phase encoding (G_y) gradient in a 2D spin-warp MRI acquisition [95]. Hence, the spatial distortion along the slice selective axis is significantly smaller than in-plane, and its effect can be ignored [93]. In addition, for a 2D EPI acquisition with N phase encoding lines, the time taken to span k-space in the phase encoding direction is at least N times larger than the time taken in the frequency encoding direction, resulting in the bandwidth per point in the phase encoding direction being $1/N$ of that in frequency encoding direction [95]. Therefore, the spatial distortion along the phase encoding direction will be the dominant effect in an EPI acquisition [95]. However, the forward-reverse correction algorithm requires accurate edge detection to segment the imaged object from the background. This can be difficult, especially for DW images whose SNR is typically much lower than other, e.g., T1 or T2 weighted images, or images containing ghosts or regions with relatively large susceptibility artifacts. Also this method is sensitive to noise if the imaged object has regions of low SNR, since errors accumulate along each line integral affecting the correction of all points along the particular line [95].

Jezzard et al. [97] suggested the use of a field map to correct geometric distortion caused by inhomogeneous B0 fields, especially for EPI acquisitions. It calculates the phase map from each of two gradient echo images acquired with slightly different echo times (ΔTE), and the field inhomogeneity map is then calculated. The field map is converted into a voxel shift map which is simply the ratio between field inhomogeneity (Hz) and effective bandwidth per voxel in phase-encode direction. In their study, large field inhomogeneities observed around the frontal lobe, temporal lobe and cerebellum were reduced after field inhomogeneity correction using the field map. Like the forward-reverse method, low SNR also affects each voxel in a field map correction, but the error is not accumulated from one voxel to another. Other sources of artifacts, B1 inhomogeneity [98] or gradient nonlinearity, may be reduced by using multi-channel excitation [99] or estimating a gradient coil tensor [100], but these are not addressed in this work.

CHAPTER Ⅲ

CHARACTERIZING FIBER DIRECTIONAL UNCERTAINTY IN DT-MRI

3.1. Overview

Image noise in diffusion tensor MRI (DT-MRI) causes errors in the measured tensor, and hence variance in the estimated fiber orientation. Uncertainty in fiber orientation has been described using a circular "cone of uncertainty” (CU) around the principal eigenvector of the diffusion tensor. The cone of uncertainty has proved to be a useful construct for quantifying and visualizing the variability of DT-MRI parameters and fiber tractography. The assumption of circularity of the CU has not been tested directly, however. In this work, bootstrap analysis and simple theoretical arguments were used to show that the cone of uncertainty is elliptical and multivariate normal in the vast majority of white matter voxels for typical measurement conditions. The dependence of the cone angle on signal-to-noise ratio and eigenvalue contrast was established. The major and minor cone axes are shown to be coincident with the second and third eigenvectors of the tensor, respectively, in the limit of many uniformly spaced diffusion encoding directions. The deviation between the major cone axis and the second eigenvector was quantified for typical sets of diffusion weighting directions. The elliptical cone of uncertainty provides more realistic error information for fiber tracking algorithms and a quantitative basis for selecting diffusion tensor imaging acquisition protocols.

3.2. Introduction

Diffusion tensor MRI (DT-MRI) provides information on water molecular diffusion based on a series of images with diffusion weighting applied in at least six non-collinear directions [19,20]. Given the effective diffusion tensor, it is possible to characterize tissue microstructure using the directional dependence of diffusion *in vivo* [26,58]. In addition, this directional information has been exploited to estimate the paths of fiber bundles in the brain in order to infer axonal connectivity [29]. In this case, the principal eigenvector (i.e., the estimated direction of maximum diffusivity), $\mathbf{v}_1$, is taken to be parallel to the local fiber bundle. In the presence of image noise, however, perturbations of the diffusion tensor field introduce errors in the estimated diffusion anisotropy [38-40] and fiber direction [41,42].

The directional uncertainty in $\mathbf{v}_1$ has been characterized by the 'cone of uncertainty' [43,48]. This was defined as a circular cone with axis along the expectation value of $\mathbf{v}_1$ and cone angle equal to the uncertainty (i.e., confidence interval) in the orientation of $\mathbf{v}_1$. The cone of uncertainty (CU) is particularly useful for visualizing the uncertainty in fiber orientation and predicting error in MR fiber tractography. However, Lazar and Alexander [49,50] showed that errors in MR tractography typically have an elliptical distribution, and noted that an elliptical CU is expected in voxels that lack axially symmetric diffusion. They measured the dispersion of fiber tracking errors in a plane perpendicular to the fiber axis at some distance from the seed points. They noted a strong correlation between the direction of the greatest dispersion of tracking errors and the second eigenvector of the tensor (corresponding to the second largest diffusivity). The same relationship existed between the direction of the smallest dispersion of tracking errors and the third eigenvector of the tensor (corresponding to the smallest diffusivity).

In this chapter, we provide a general explanation for this observation, and present results of experimental and theoretical studies of the properties of the CU. In particular, we tested the symmetry and multivariate normality of principal eigenvector errors, and characterized the dependence of the associated CU on image noise, diffusion anisotropy and eigenvalue contrast. In addition, we investigated the coincidence between the tensor eigenvectors and the axes of the elliptical cone, and how this correspondence depends on the diffusion gradient encoding scheme. Some of this work has appeared previously in abstract form [47]. Koay et al have recently proposed a similar construction of the elliptical cone of uncertainty [45].

3.3. Theory

The dependence of the major eigenvector (i.e., the eigenvector corresponding to the largest eigenvalue), $\mathbf{v}_1$, on tensor errors can be found from first order perturbation theory [41,43,44] or simple error analysis [46]. The major eigenvector of the diffusion tensor satisfies the eigenvalue equation

$$\mathbf{D}\mathbf{v}_1 = \lambda_1 \mathbf{v}_1 , \tag{3.1}$$

where $\mathbf{D}$ and λ_1 are the true tensor and major eigenvalue (i.e., $\lambda_1 > \lambda_2 \geq \lambda_3$), respectively. Taking the differential of both sides of (3.1) gives a relation among the errors in these quantities:

$$\delta\mathbf{D} \cdot \mathbf{v}_1 + \mathbf{D} \cdot \delta\mathbf{v}_1 = \delta\lambda_1 \cdot \mathbf{v}_1 + \lambda_1 \cdot \delta\mathbf{v}_1 . \tag{3.2}$$

The tensor is represented by a 3 × 3 symmetric matrix and the principal eigenvector is a 3 × 1 column vector. Multiplying (3.2) by the transpose of the middle eigenvector $\mathbf{v}_2$, denoted by $\mathbf{v}_2^{\mathrm{T}}$, yields

$$\mathbf{v}_2^{\mathrm{T}} \cdot \delta\mathbf{D} \cdot \mathbf{v}_1 + \mathbf{v}_2^{\mathrm{T}}\mathbf{D} \cdot \delta\mathbf{v}_1 = \delta\lambda_1 \cdot \mathbf{v}_2^{\mathrm{T}}\mathbf{v}_1 + \lambda_1 \mathbf{v}_2^{\mathrm{T}} \cdot \delta\mathbf{v}_1 . \tag{3.3}$$

Since the eigenvectors are orthogonal,

$$\mathbf{v}_2^{\mathrm{T}}\mathbf{v}_1 = 0 . \tag{3.4}$$

The eigenvalue equation for $\mathbf{v}_2$ is

$$\mathbf{D}\mathbf{v}_2 = \lambda_2 \mathbf{v}_2 ,$$

and the transpose of this relation is

$$\mathbf{v}_2^{\mathrm{T}}\mathbf{D} = \lambda_2 \mathbf{v}_2^{\mathrm{T}} ,$$

since **D** is symmetric. Multiplying on the right by $\delta\mathbf{v}_1$, the error in $\mathbf{v}_1$, gives

$$\mathbf{v}_2^{\mathrm{T}}\mathbf{D}\cdot\delta\mathbf{v}_1 = \lambda_2 \mathbf{v}_2^{\mathrm{T}}\cdot\delta\mathbf{v}_1 . \tag{3.5}$$

Substituting (3.4) and (3.5) into (3.3) gives

$$\mathbf{v}_2^{\mathrm{T}}\cdot\delta\mathbf{D}\cdot\mathbf{v}_1 + \lambda_2 \mathbf{v}_2^{\mathrm{T}}\cdot\delta\mathbf{v}_1 = \lambda_1 \mathbf{v}_2^{\mathrm{T}}\cdot\delta\mathbf{v}_1 .$$

The component of the $\mathbf{v}_1$ error ($\delta\mathbf{v}_1$) in the $\mathbf{v}_2$ direction is therefore

$$\mathbf{v}_2^{\mathrm{T}}\cdot\delta\mathbf{v}_1 = \frac{\mathbf{v}_2^{\mathrm{T}}\cdot\delta\mathbf{D}\cdot\mathbf{v}_1}{\lambda_1 - \lambda_2} . \tag{3.6}$$

Replacing $\mathbf{v}_2$ by $\mathbf{v}_3$ in (3.3) leads to an analogous expression for the component of the $\mathbf{v}_1$ error in the $\mathbf{v}_3$ direction:

$$\mathbf{v}_3^{\mathrm{T}}\cdot\delta\mathbf{v}_1 = \frac{\mathbf{v}_3^{\mathrm{T}}\cdot\delta\mathbf{D}\cdot\mathbf{v}_1}{\lambda_1 - \lambda_3} . \tag{3.7}$$

The eigenvectors have unit length, so for example,

$$\mathbf{v}_1^{\mathrm{T}}\cdot\mathbf{v}_1 = 1 .$$

Differentiating both sides of this equation yields

$$\delta\mathbf{v}_1^{\mathrm{T}}\cdot\mathbf{v}_1 + \mathbf{v}_1^{\mathrm{T}}\cdot\delta\mathbf{v}_1 = 0 .$$

Since the two terms on the left are scalars and each is the transpose of the other, they must be equal. Hence,

$$\mathbf{v}_1^{\mathrm{T}} \cdot \delta\mathbf{v}_1 = 0 . \tag{3.8}$$

The $\mathbf{v}_1$ error, $\delta\mathbf{v}_1$, is perpendicular to the $\mathbf{v}_1$ direction. Taken together, (3.6), (3.7) and (3.8) specify the three orthogonal components of the error in the major eigenvector corresponding to a given tensor error, $\delta\mathbf{D}$.

The covariance matrix, $\mathbf{\Sigma}_{\mathbf{v}_1}$, for $\mathbf{v}_1$ in the $\{\mathbf{v}_2, \mathbf{v}_3\}$ plane gives the variance of $\delta\mathbf{v}_1$ along $\mathbf{v}_2$ and $\mathbf{v}_3$ on the diagonal and the covariance of these components in the off-diagonal elements:

$$\begin{aligned}\mathbf{\Sigma}_{\mathbf{v}_1} &= \begin{bmatrix} \left\langle \left(\mathbf{v}_2^{\mathrm{T}} \cdot \delta\mathbf{v}_1\right)^2 \right\rangle & \left\langle \left(\mathbf{v}_2^{\mathrm{T}} \cdot \delta\mathbf{v}_1\right) \cdot \left(\mathbf{v}_3^{\mathrm{T}} \cdot \delta\mathbf{v}_1\right) \right\rangle \\ \left\langle \left(\mathbf{v}_2^{\mathrm{T}} \cdot \delta\mathbf{v}_1\right) \cdot \left(\mathbf{v}_3^{\mathbf{T}} \cdot \delta\mathbf{v}_1\right) \right\rangle & \left\langle \left(\mathbf{v}_3^{\mathrm{T}} \cdot \delta\mathbf{v}_1\right)^2 \right\rangle \end{bmatrix} \\ &= \begin{bmatrix} \dfrac{\left\langle \left(\mathbf{v}_2^{\mathrm{T}} \cdot \delta\mathbf{D} \cdot \mathbf{v}_1\right)^2 \right\rangle}{\left(\lambda_1 - \lambda_2\right)^2} & \dfrac{\left\langle \left(\mathbf{v}_2^{\mathrm{T}} \cdot \delta\mathbf{D} \cdot \mathbf{v}_1\right)\left(\mathbf{v}_3^{\mathrm{T}} \cdot \delta\mathbf{D} \cdot \mathbf{v}_1\right) \right\rangle}{\left(\lambda_1 - \lambda_2\right)\left(\lambda_1 - \lambda_3\right)} \\ \dfrac{\left\langle \left(\mathbf{v}_2^{\mathrm{T}} \cdot \delta\mathbf{D} \cdot \mathbf{v}_1\right)\left(\mathbf{v}_3^{\mathrm{T}} \cdot \delta\mathbf{D} \cdot \mathbf{v}_1\right) \right\rangle}{\left(\lambda_1 - \lambda_2\right)\left(\lambda_1 - \lambda_3\right)} & \dfrac{\left\langle \left(\mathbf{v}_3^{\mathrm{T}} \cdot \delta\mathbf{D} \cdot \mathbf{v}_1\right)^2 \right\rangle}{\left(\lambda_1 - \lambda_3\right)^2} \end{bmatrix},\end{aligned} \tag{3.9}$$

using (3.6) and (3.7). Diagonalizing the covariance matrix identifies the principal components of $\mathbf{v}_1$ variation. To be explicit, suppose the z axis is chosen to be parallel to $\mathbf{v}_1$. For convenience we choose the x and y axes to be parallel to $\mathbf{v}_2$ and $\mathbf{v}_3$, respectively. Because of measurement errors in **D**, the estimated principal eigenvector will have components in the x and y directions. Let the coordinates of $\delta\mathbf{v}_1$ be (x, y). In this case, (3.9) can be written as

$$\begin{aligned}\mathbf{\Sigma}_{\mathbf{v}_1} &= \begin{bmatrix} \left\langle x^2 \right\rangle & \left\langle x \cdot y \right\rangle \\ \left\langle x \cdot y \right\rangle & \left\langle y^2 \right\rangle \end{bmatrix} \\ &= \begin{bmatrix} \dfrac{\left\langle \delta D_{xz}^2 \right\rangle}{\left(\lambda_z - \lambda_x\right)^2} & \dfrac{\left\langle \delta D_{xz} \cdot \delta D_{yz} \right\rangle}{\left(\lambda_z - \lambda_x\right)\left(\lambda_z - \lambda_y\right)} \\ \dfrac{\left\langle \delta D_{xz} \cdot \delta D_{yz} \right\rangle}{\left(\lambda_z - \lambda_x\right)\left(\lambda_z - \lambda_y\right)} & \dfrac{\left\langle \delta D_{yz}^2 \right\rangle}{\left(\lambda_z - \lambda_y\right)^2} \end{bmatrix},\end{aligned} \tag{3.10}$$

where $\delta D_{xy} \equiv \mathbf{e}_x^{\mathrm{T}} \cdot \delta\mathbf{D} \cdot \mathbf{e}_y$, $\delta D_{xz} \equiv \mathbf{e}_x^{\mathrm{T}} \cdot \delta\mathbf{D} \cdot \mathbf{e}_z$, $\delta D_{yz} \equiv \mathbf{e}_y^{\mathrm{T}} \cdot \delta\mathbf{D} \cdot \mathbf{e}_z$ and $\mathbf{e}_x$, $\mathbf{e}_y$, and $\mathbf{e}_z$ are unit vectors along the coordinate axes. If the errors $\delta\mathbf{v}_1$ have a multivariate normal distribution then they can be characterized concisely using the eigenvalues σ_1 and σ_2 $\left(\sigma_1 \geq \sigma_2\right)$ and corresponding eigenvectors $\mathbf{e}_1$ and $\mathbf{e}_2$ of the covariance matrix. In this case, the probability density function for $\delta\mathbf{v}_1$ is

$$P\left(\delta\mathbf{v}_1\right) = \frac{1}{2\pi\left|\mathbf{\Sigma}_{\mathbf{v}_1}\right|^{1/2}} \cdot \exp\left(-\frac{1}{2}\delta\mathbf{v}_1^{\mathrm{T}} \cdot \mathbf{\Sigma}_{\mathbf{v}_1}^{-1} \cdot \delta\mathbf{v}_1\right), \tag{3.11}$$

assuming the mean value of $\delta\mathbf{v}_1$ is zero. A contour of constant probability density is defined by the set of coordinates $\left(x, y\right)$ that satisfies the relation

$$\begin{bmatrix} x & y \end{bmatrix} \cdot \mathbf{\Sigma}_{\mathbf{v}_1}^{-1} \cdot \begin{bmatrix} x \\ y \end{bmatrix} = c^2, \tag{3.12}$$

with constant c. The solution to this equation is an ellipse with semi-major axis of length $c\sqrt{\sigma_1}$ parallel to $\mathbf{e}_1$ and semi-minor axis of length $c\sqrt{\sigma_2}$ parallel to $\mathbf{e}_2$ [101]. If the eigenvalues of the covariance matrix are not equal, then the errors are not circularly symmetric in the (x, y) plane. In the general multivariate normal case, the errors have an ellipsoidal distribution, the major and minor axes of the ellipse given by the eigenvectors of the covariance matrix. In the limit of many uniformly distributed diffusion measurement directions, the off-diagonal terms go to zero, $\left\langle \delta D_{xz} \cdot \delta D_{yz} \right\rangle = 0$, so $\mathbf{\Sigma}_{\mathbf{v}_1}$ is diagonal in the eigenframe of the tensor (see Appendix). Further, it is shown that if $\lambda_2 > \lambda_3$ then $\left\langle \delta D_{xz}^2 \right\rangle > \left\langle \delta D_{yz}^2 \right\rangle$. This implies that the upper-left element in (3.10) is the largest eigenvalue of $\mathbf{\Sigma}_{\mathbf{v}_1}$, and hence the major axis of the ellipsoidal distribution is parallel to $\mathbf{v}_2$. To test whether this relation holds for practical (i.e., finite) diffusion encoding schemes, we performed the experiments described below. Before leaving this topic, however, we should note that if the tensor eigenvalues are equal ($\lambda_1 = \lambda_2$ or $\lambda_1 = \lambda_2 = \lambda_3$), then (3.6) and (3.7) fail. In this case, degenerate perturbation theory must be used to evaluate the $\delta\mathbf{v}_1$ errors [41]. However, the exactly degenerate situation is unlikely to arise in routine white matter tractography.

3.4. Methods

3.4.1. DT-MRI acquisition

The study protocol was approved by Vanderbilt University's institutional review board. Diffusion weighted images were acquired in a healthy adult using a 3 Tesla whole body GE scanner (40 mT/m maximum gradient strength, 150 mT/m/ms maximum slew rate). A dual spin echo EPI pulse sequence was used to acquire images with diffusion weighting (1000 s/mm^2), applied in six non-collinear directions [23] as well as a set of images with no diffusion weighting. All images (7 images in each of 30 slice locations) had an 89 ms echo time, 9 s repetition time, 128×128 acquisition reconstructed to a 256×256 image matrix, and 2×2×4 mm^3 voxel size. A total of 37 identical scans were acquired in one imaging session. Image alignment was assessed by visual inspection of the difference between the first and the last images of each slice during the session (this revealed no significant differences in head position). All of the image data were averaged in order to estimate the 'true' diffusion tensor, and 'true' orientation of the principal eigenvector, $\mathbf{v}_1$, in each voxel with high precision. Smaller sets of the image data were also averaged to investigate the dependence of $\mathbf{v}_1$ errors on net image SNR.

3.4.2. Generation of principal components and CU

Bootstrap resampling [51] was used to select N_A acquisitions to average ($N_A \leq 37$). Each set of N_A acquisitions is one *sample*. We formed 100, 200, 500 and 1000 samples with replacement, then calculated the diffusion tensor and major eigenvector for each sample in each voxel. The eigenvalue-eigenvector pairs were sorted according to their similarity with the estimated ‘true’ values using a tensor overlap measure [42]. Each estimate, $\hat{\mathbf{v}}_1$, of the major eigenvector was projected onto the plane perpendicular to the ‘true’ $\mathbf{v}_1$ (i.e., the plane defined by the best estimates of the two other eigenvectors, $\mathbf{v}_2$ and $\mathbf{v}_3$):

$$\mathrm{Proj}_{\mathbf{v}_j}\left(\hat{\mathbf{v}}_1\right)=\left(\mathbf{v}_j^{\mathrm{T}}\hat{\mathbf{v}}_1\right)\mathbf{v}_j, \qquad j=2,3. \tag{3.13}$$

A principal component (PC) analysis was used to analyze the distribution of $\hat{\mathbf{v}}_1$ projections on the $\{\mathbf{v}_2,\mathbf{v}_3\}$ plane and hence determine the major and minor axes of the CU. The covariance matrix of projection coordinates was diagonalized. The eigenvalues, σ_1 and σ_2, and corresponding (normalized) eigenvectors, $\mathbf{e}_1$ and $\mathbf{e}_2$, of the covariance matrix were used to construct an ellipse parallel to the $\{\mathbf{v}_2,\mathbf{v}_3\}$ plane and centered on $\mathbf{v}_1$:

$$\vec{\mathbf{r}}\left(\varphi\right)=\mathbf{v}_1+\sigma_1\cos\varphi\,\mathbf{e}_1+\sigma_2\sin\varphi\,\mathbf{e}_2. \tag{3.14}$$

The eigenvectors, $\mathbf{e}_1$ and $\mathbf{e}_2$, define the major and minor axes of the ellipse. The CU was then defined as the set of line segments from the origin to the ellipse, which is the *directrix* of the conical surface (3.14). For display purposes, all dimensions were scaled by the tensor’s fractional anisotropy (FA) [26] (see Figure 3.1a).

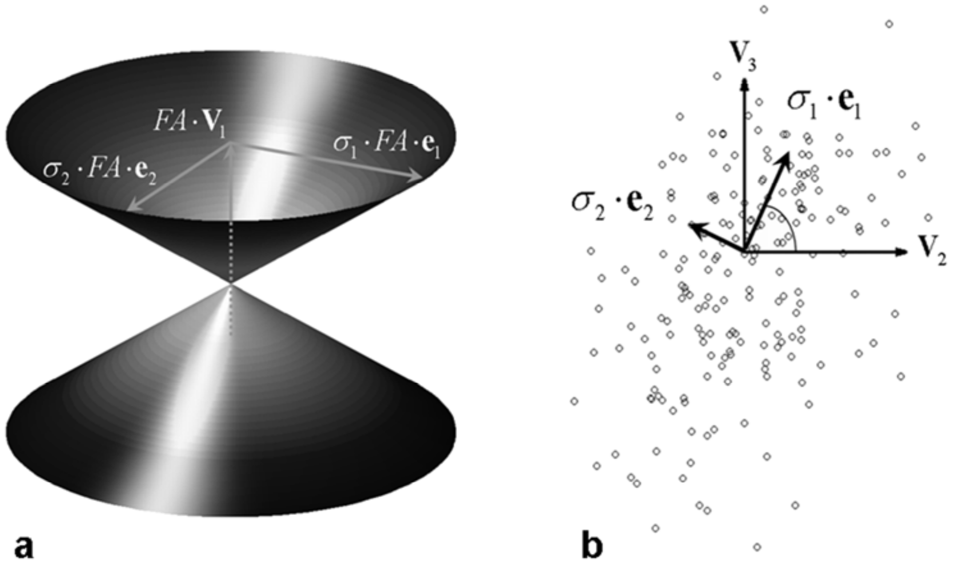

Figure 3.1. Construction of the cone of uncertainty (a) based on the projection of $\hat{\mathbf{v}}_1$ (circles) onto the $\{\mathbf{v}_2, \mathbf{v}_3\}$ plane (b) for a representative white matter voxel with 6 scans averaged (FA = 0.73, 200 bootstrap samples). The size of the cone (i.e., its height and major and minor axes) is scaled by FA, and the directions of the major and minor cone axes (denoted by $\mathbf{e}_1$ and $\mathbf{e}_2$, respectively) are given by the principal components ($\sigma_1\cdot\mathbf{e}_1$ and $\sigma_2\cdot\mathbf{e}_2$) of the $\mathbf{v}_1$ error distribution shown as circles in (b). The coincidence angle ($\angle$) between $\mathbf{e}_1$ and $\mathbf{v}_2$ is also shown (b).

3.4.3. Symmetry, normality and cone angles of the CU

The equality of the major and minor axes of the ellipse (i.e., the standard deviations of the PCs') was tested using the method by Bartlett [102]. The multivariate normality of the distribution of $\hat{\mathbf{v}}_1$ projections was tested using the method of Mardia [103,104] for multivariate skewness and kurtosis and mapped for 200 bootstrap samples with two levels of image SNR (i.e., N_A). We define the cone angles as $\theta_i \equiv \tan^{-1}(\sigma_i)$,

$i = 1,2$. In the limit of many uniformly distributed gradients, the cone angle can be approximated using (3.9) as

$$\theta_i \approx \frac{\left[\left\langle \left(\mathbf{v}_{i+1}^{\mathrm{T}} \cdot \delta\mathbf{D} \cdot \mathbf{v}_1\right)^2 \right\rangle\right]^{1/2}}{\lambda_1 - \lambda_{i+1}}, \quad i = 1,2 . \tag{3.15}$$

Bootstrap estimates of the cone angles were compared to this expression to verify the simple theoretical model of fiber directional uncertainty. The cone angles were also compared in voxels with different levels of FA and image SNR.

3.4.4. Coincidence between the CU and tensor principal axes

To quantify the alignment of the major cone axis with the tensor eigenvectors, we defined the *coincidence angle* to be the angle between $\mathbf{e}_1$ and $\mathbf{v}_2$ (see Figure 3.1b). Because we used the same 6 direction gradient vector set [23] during the entire experiment, simulations were used to study how the coincidence angle depends on the choice of gradient vector set. Several gradient sets were used, these were labeled 'original #' (# is the number of gradient vectors) and included 'original 6' [23], 'original 12' [105], 'original 21' (second order icosahedral tessellation of the unit sphere), 'original 92' (46 directions, given by third order icosahedral tessellation, and their opposites). The 'original #' scheme is the set of gradient vectors originally described in the corresponding references or determined numerically [106]. The ‘rotated #’ scheme is labeled similarly, e.g., ‘rotated 6’, after 45 degrees rotation of the ‘original’ scheme around the Z axis in the gradient coordinate system. For the simulation, we used the measured noise standard deviation and ‘true’ diffusion tensor (obtained by averaging the entire data set) to generate diffusion weighted and non-weighted signals, including simulated random noise, for each gradient vector scheme listed above. This simulation was repeated 200 times, and the simulated data were then analyzed to determine the coincidence angle between the major axis of the CU and the second eigenvector of the ‘true’ tensor. Hence, for this part of the study, the axes of the CU were estimated via Monte Carlo simulation for each gradient vector set.

The dependence of the coincidence angle on the choice of gradient vector scheme can be understood in terms of the $\hat{\mathbf{v}}_1$ covariance matrix elements, as in (3.9) in the tensor eigenvector frame. We selected a representative voxel in the splenium of corpus callosum and simulated diffusion weighted signals (as described above) in the tensor eigenframe based on the gradient schemes listed above. In the simulation, we used the coordinate naming convention of the Appendix: $\hat{x} \parallel \hat{\mathbf{v}}_2$, $\hat{y} \parallel \hat{\mathbf{v}}_3$, and $\hat{z} \parallel \hat{\mathbf{v}}_1$ and simulated the effect of noise using Monte Carlo simulations. In each trial, the errors δD_{ij} of the diffusion tensor elements were calculated. The covariance matrix elements of (3.9) were then plotted to show the dependence of the matrix elements on the choice of gradient scheme.

3.5. Results

3.5.1. Comparison of bootstrap and theoretical results

Bootstrap estimates of the projection of $\hat{\mathbf{v}}_1$ onto the $\{\mathbf{v}_2, \mathbf{v}_3\}$ plane (i.e., the $\mathbf{v}_1$ error) are shown schematically for a representative white matter voxel in the splenium of the corpus callosum in Figure 3.1b. The principal components of the distribution are also shown. The principal components of $\mathbf{v}_1$ errors can be estimated from this distribution or from (3.9). These two estimates were compared in order to test the accuracy of the simple theoretical model applied to *in vivo* data. The standard deviation of $\mathbf{v}_1$ errors for the minor principal component calculated using perturbation theory (σ_{PT}, the square root of the smaller eigenvalue of the covariance matrix in (3.9)) was correlated with the bootstrap estimate (σ_{BS}). The correlation was calculated for those voxels whose linearity index [107] $C_l > 0.3$, to exclude voxels with nearly isotropic diffusion, for example in the CSF ($N_A = 6$ and 200 bootstrap samples were used). The correlation was excellent ($R^2 = 0.998$ and slope = 0.99 with offset ≈ 0). Results were similar for the major principal component (R^2 = 0.994 and slope = 0.98 with offset $\approx$ 0). The agreement between the two estimates of $\mathbf{v}_1$ errors is excellent (for $C_l > 0.3$), with the R^2 and slope of the fit nearly equal to one.

3.5.2. Test for symmetry and multivariate normality of CU

The directional uncertainty in $\hat{\mathbf{v}}_1$ is represented by the cone of uncertainty centered on $\mathbf{v}_1$ as shown in Figure 3.2. The CUs for voxels in the outlined region of Figures 3.2a and 3.2b are shown in Figure 3.2c for $N_A = 6$ and 200 bootstrap samples. The CUs for voxels in the outlined region of Figure 2c are redrawn (inset in the lower right corner) as viewed along the local $\mathbf{v}_1$ axis to show the cones' eccentricity clearly. Each cone is color coded according to base 10 logarithm of the p-value from the test of the circular symmetry of $\hat{\mathbf{v}}_1$ errors in the $\{\mathbf{v}_2, \mathbf{v}_3\}$ plane (i.e., the test of equality of the principal component variances). Hence, color indicates the statistical significance of CU eccentricity. As the color varies from red to blue, the cones of uncertainty change from nearly circular (for $p > 0.05$, $\log_{10}(p) = \log_{10}(0.05) > -1.3$) to highly eccentric. Most of the voxels in the ROI exhibit non-circular CUs (Table 3.1) based on bootstrap comparisons of major and minor cone axes.

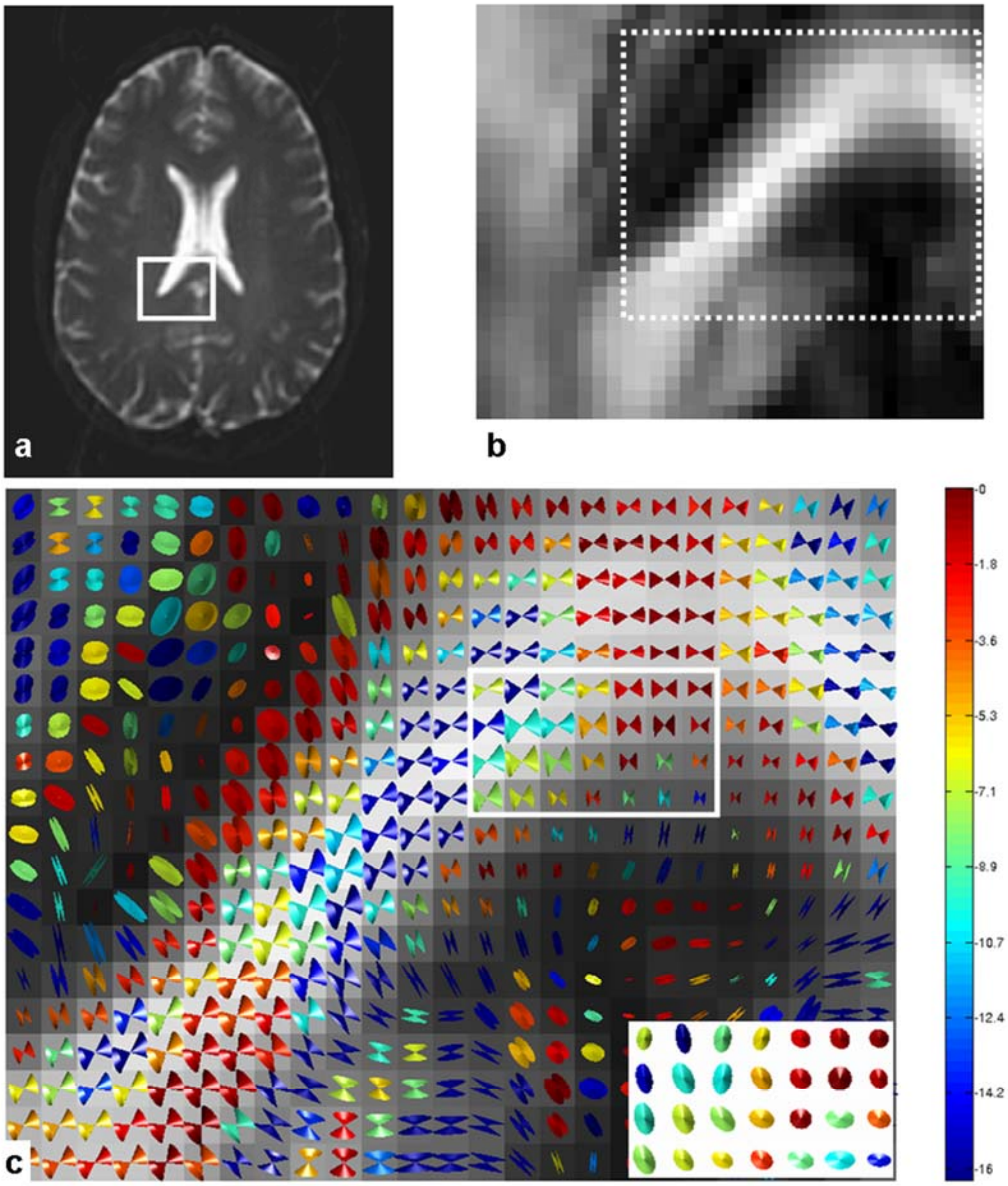

Figure 3.2. A T2-weighted image (a) showing an ROI and its FA map (b). The white dotted area in (b) is used in (c) for CU visualization. The CUs (using 6 averages, 200 bootstrap samples) are color coded according to base 10 logarithm of the p-value from the test for zero eccentricity. Low probability of circularity (zero eccentricity) is shown as dark blue, while high probability is shown as red (c). The base of each cone in the rectangular region in (c) is shown in the local $\mathbf{v}_2$ (horizontal in the inset) - $\mathbf{v}_3$ (vertical) plane at the lower right corner in (c). Those cones are uniformly scaled for clear visualization.

Table 3.1. Percentage of voxels in the ROI (Figure 3.2a) with eccentric cones of uncertainty (p-value ≤ 0.05) from bootstrap results.

Number of acquisitions averaged	Number of bootstrap samples			
	100	200	500	1000
2	67.9	81.1	90.5	94.8
4	76.0	84.8	93.6	96.2
6	77.4	86.3	93.6	96.3
12	79.1	88.0	95.0	97.0
24	81.5	88.4	94.4	97.3

In the second analysis, every voxel in the ROI was tested for multivariate normality of $\hat{\mathbf{v}}_1$ errors using the test of multivariate skewness and kurtosis [103,104]. Figure 3.3 shows that most white matter voxels exhibit multivariate normality of the error distribution based on this test.

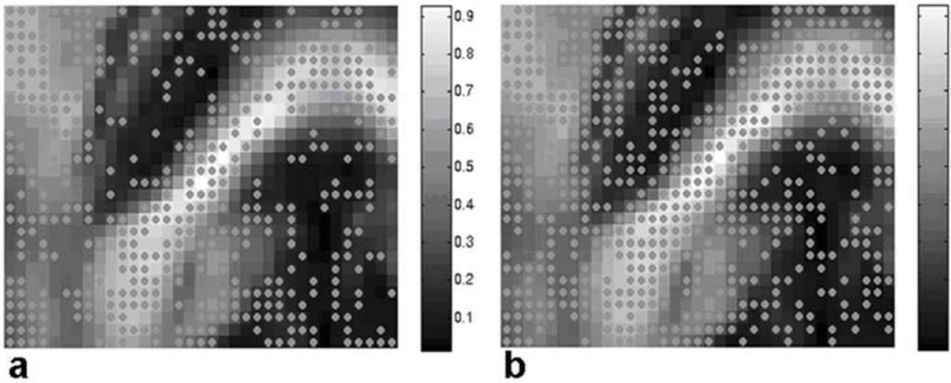

Figure 3.3. Mapped results of the test of multivariate normality (skewness and kurtosis) for the ROI (Figure 3.2a) superimposed on the FA map. Dots indicate multivariate

(Figure 3.3. Continued.)
normality in fiber directional error with 4 (a) and 12 (b) averaged scans and 200 bootstrap samples for p-value of 0.05. The fractional number of voxels with multivariate normal error over the whole ROI is approximately 47 % (a) and 64 % (b), and increases as N_A increases.

According to the circular symmetry test, the estimated fraction of cones with significant eccentricity increases as the number of bootstrap samples and N_A increase (Table 3.1) and the fraction of voxels with normally distributed error increases with increasing N_A (Figure 3.3).

3.5.3. Characterization of fiber directional uncertainty as a cone angle

The cone angle, θ, was defined for both the major and minor axes of the cone base (θ_1 and θ_2, respectively). The cone angle is the arc tangent of the standard deviation of the $\hat{\mathbf{v}}_1$ error in the corresponding principal component direction (see Figure 3.1a). The dependence of the cone angle on image SNR is shown for a representative voxel in the splenium of the corpus callosum in Figure 3.4.

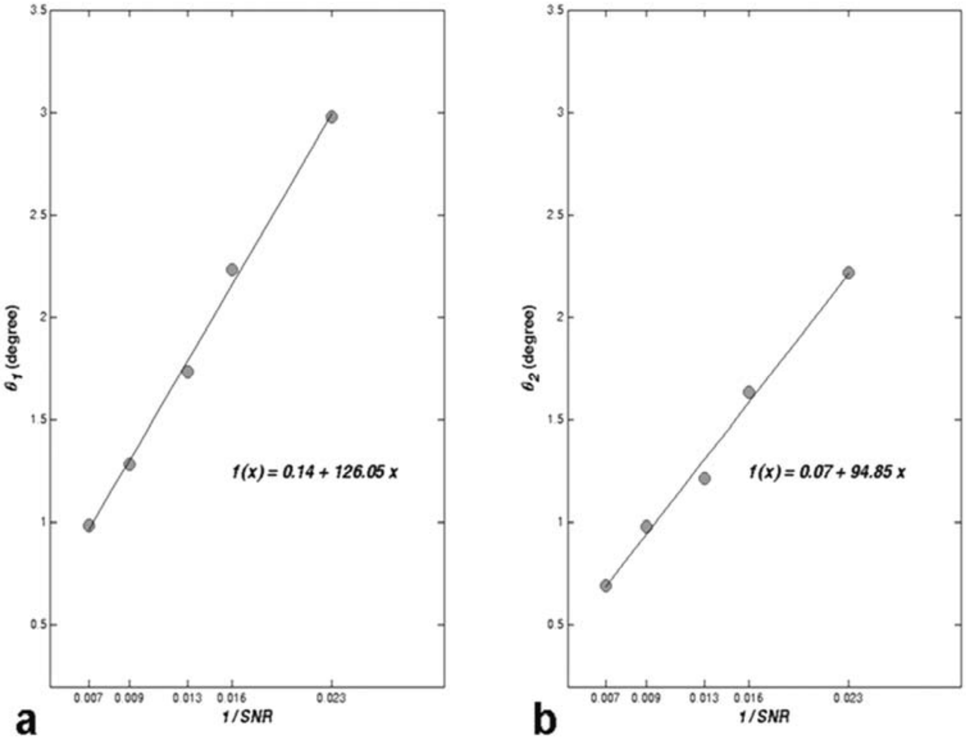

Figure 3.4. Cone angle of the major (θ_1) and minor (θ_2) axes fit to a linear function of SNR^{-1} (SNR = $N_A^{1/2}$ ·SNR$_0$) for a typical white matter voxel (FA = 0.71 and 200 bootstrap samples). SNR$_0$ is measured using the non-weighted image. The equation of the line is shown as a function of x = SNR^{-1}. As SNR decreases, the cone angle increases in proportion to SNR^{-1}.

Here the cone angle is plotted as a function of 1/SNR, where SNR = $N_A^{1/2}$ ·SNR$_0$, and SNR$_0$ is measured on a single non-weighted image (SNR$_0$ = 31.3). As expected, the cone angle is proportional to the standard deviation of image noise (i.e., to SNR^{-1}). All voxels tested showed similar dependence on SNR (data not shown).

The dependence of the cone angle on the eigenvalue contrast and tensor error is shown in Figure 3.5.

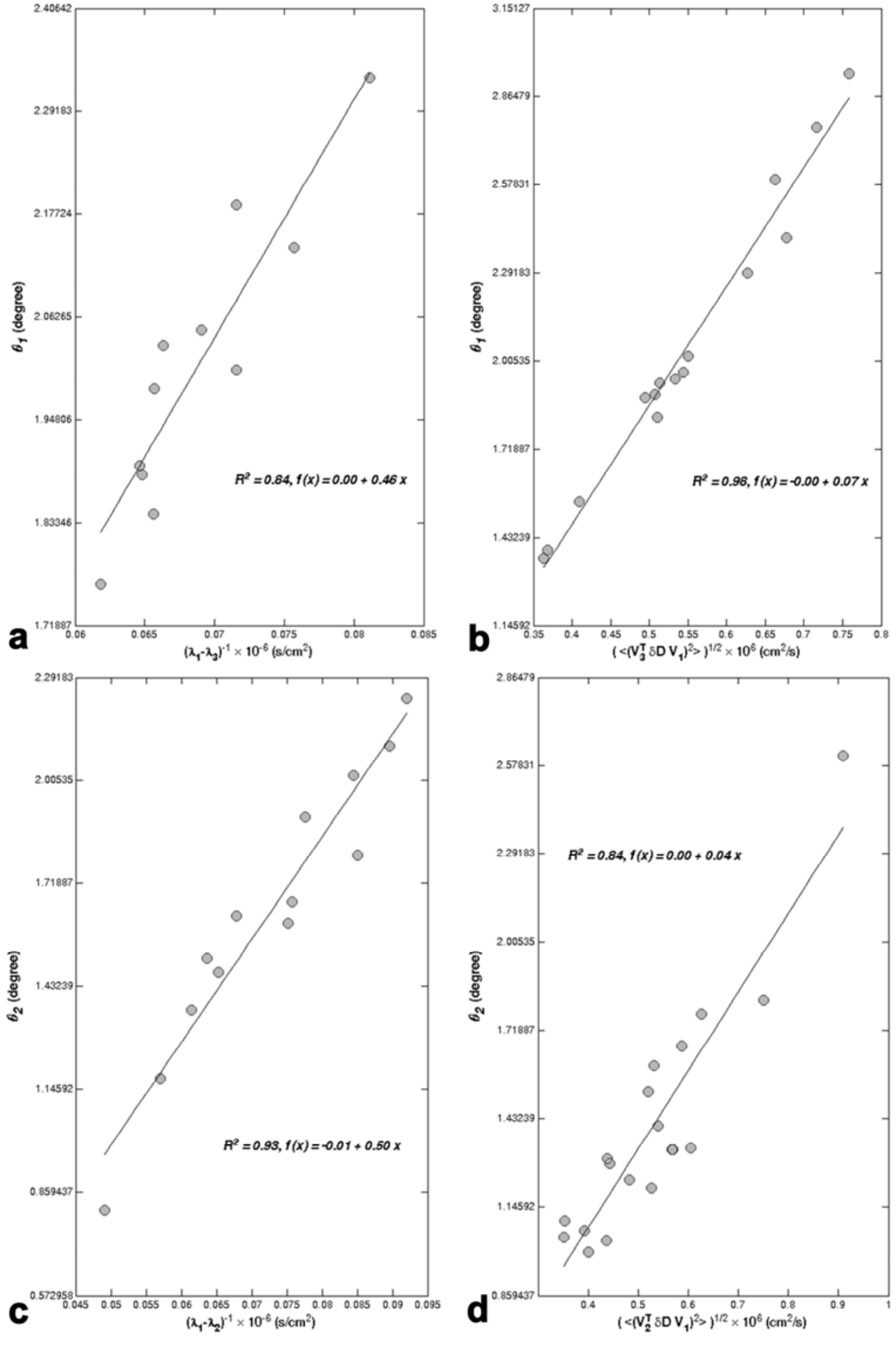

Figure 3.5. The major (a and b) and minor (c and d) cone angles (θ_1 and θ_2) are calculated over the ROI (Figure 3.2a) and plotted as a function of the reciprocal of the eigenvalue contrast (with fixed tensor error, ε_{31} for (a) and ε_{21} for (c)) and as a function

(Figure 3.5. Continued.)
of the tensor error ε_{31} for (b) and ε_{21} for (d) (with fixed eigenvalue contrast). The slope for the linear fit is 0.46 (a), 0.07 (b), 0.5 (c) and 0.04 (d) with R^2 values close to one. The 95 % confidence interval for the slope is (0.31, 0.61) (a), (0.062, 0.073) (b), (0.41, 0.59) (c) and (0.035, 0.054) (d). These intervals include the nearly constant values of $\varepsilon_{31} \cong 0.50$ (a) and $\varepsilon_{21} \cong 0.42$ (c), and $1/(\lambda_1 - \lambda_3) \cong 0.064$ (b) and $1/(\lambda_1 - \lambda_2) \cong 0.054$ (d). Hence, the data are consistent with the relations $\theta_1 \cong \varepsilon_{31}/(\lambda_1 - \lambda_3)$ and $\theta_2 \cong \varepsilon_{21}/(\lambda_1 - \lambda_2)$.

To isolate the effect of eigenvalue contrast, we fixed other relevant parameters within narrow ranges. Under the conditions of our experiment, the coincidence angle between the major cone axis and the second principal eigenvector is near 90 degrees for the most of the white matter voxels in the ROI (Figure 3.2a) as shown in Figure 3.6a (this means that the upper-left element of the covariance matrix, $\left(\Sigma_{\mathbf{v_1}}\right)_{11}$, in (3.9) is generally smaller than the lower-right element, $\left(\Sigma_{\mathbf{v_1}}\right)_{22}$).

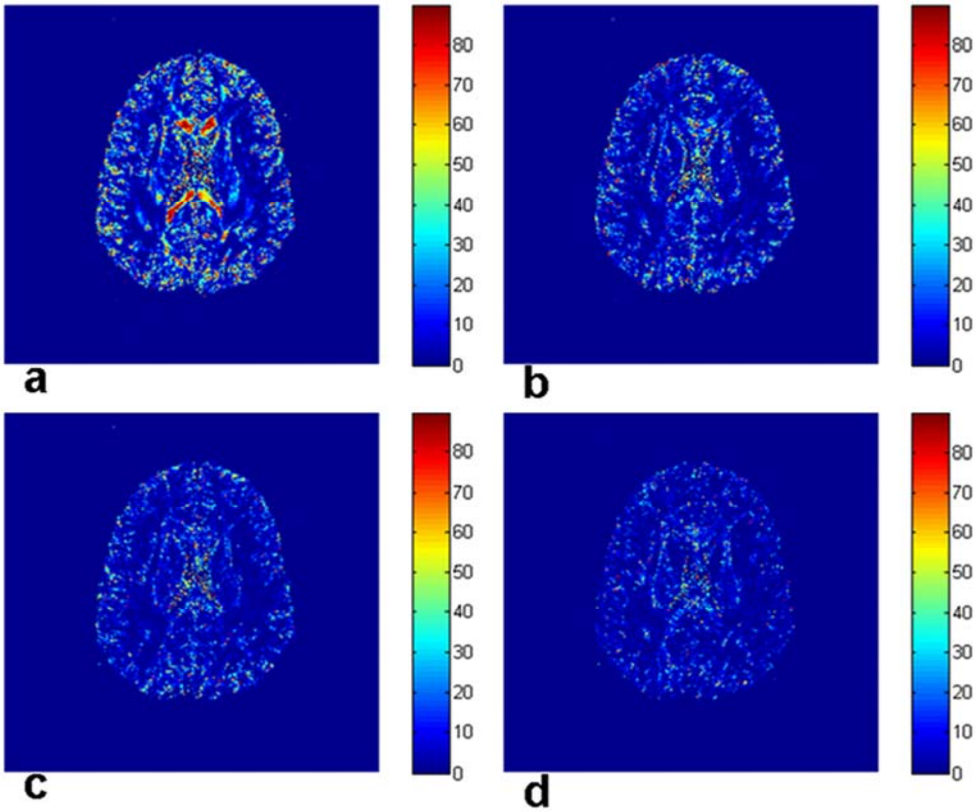

Figure 3.6. Simulated coincidence angles are shown for the whole brain slice with gradient schemes ‘original 6’ (a), ‘original 12’ (b), ‘original 21’ (c) and ‘original 92’ (d). The simulation is repeated 200 times by generating DW signals using the ‘true’ diffusion tensor with simulated random noise. The coincidence angle measures the difference in orientation between the major cone axis and the second eigenvector of the diffusion tensor (see Figure 3.1b). As the number of gradient directions (i.e., angular resolution) increases, the directional coincidence increases (i.e., the coincidence angle decreases).

Therefore, we selected voxels with similar CU orientation (i.e., $\left(\boldsymbol{\Sigma}_{\mathbf{v}_1}\right)_{11} < \left(\boldsymbol{\Sigma}_{\mathbf{v}_1}\right)_{22}$) and C_l > 0.3 (to exclude nearly isotropic voxels). For the selected voxels, a histogram of $\varepsilon_{31} \equiv \left[\left\langle \left(\mathbf{v}_3^{\mathrm{T}} \cdot \delta\mathbf{D} \cdot \mathbf{v}_1\right)^2 \right\rangle\right]^{1/2}$, the root-mean-square (RMS) error in the D_{31} tensor element, was constructed (using N_{A} = 6 with 200 bootstrap samples). The peak of the histogram (i.e., the most likely value) was identified, and all voxels with ε_{31} within 5% of this value were selected. A plot of the major cone angle (θ_1) versus $(\lambda_1 - \lambda_3)^{-1}$ for nearly constant ε_{31} is shown in Figure 3.5a. Similarly, a histogram was constructed for the eigenvalue contrast, $\lambda_1 - \lambda_3$. The peak of the histogram was identified and voxels with eigenvalue contrast within 5% of this value were selected. A plot of θ_1 versus ε_{31} for nearly constant eigenvalue contrast is shown in Figure 3.5b.

The two plots taken together verify the dependence of the major cone angle predicted by (3.15), i.e., the major cone angle should be proportional to ε_{31} and inversely proportional to $\lambda_1 - \lambda_3$. Furthermore, the slope of the line for θ_1 versus $(\lambda_1 - \lambda_3)^{-1}$ should be nearly equal to the value at the peak of the ε_{31} histogram. Similarly, the slope of the line for θ_1 versus ε_{31} should be nearly equal to $(\lambda_1 - \lambda_3)^{-1}$ for the peak of the eigenvalue contrast histogram. In fact, the 95% confidence interval for the slope contains the predicted value in both cases. Hence, the data are consistent with the relation $\theta_1 = \varepsilon_{31} / (\lambda_1 - \lambda_3)$. Analogous results were obtained for the minor cone angle using $\varepsilon_{21} \equiv \left[\left\langle \left(\mathbf{v}_2^{\mathrm{T}} \cdot \delta\mathbf{D} \cdot \mathbf{v}_1 \right)^2 \right\rangle \right]^{1/2}$ and $(\lambda_1 - \lambda_2)^{-1}$ (Figures 3.5c and d). The predictions of first order perturbation theory and bootstrap analysis are in good agreement. However, for the conditions of this experiment both methods make the opposite assignment of major and minor cone axes relative to the case of uniform angular sampling, (3.15). This is elaborated on below.

Figure 3.7 shows the dependence of the cone angles on FA and the number of averages (N_A). For all bootstrap samples, the maximum cone angles (N_A = 2, low FA) lie between 24 and 25 degrees and 20 to 22 degrees for the major and minor axes, respectively. With increasing numbers of averaged diffusion weighted signals (N_A = 2, 6 and 24) and FA, the directional uncertainty is reduced significantly as shown in Figure 3.7.

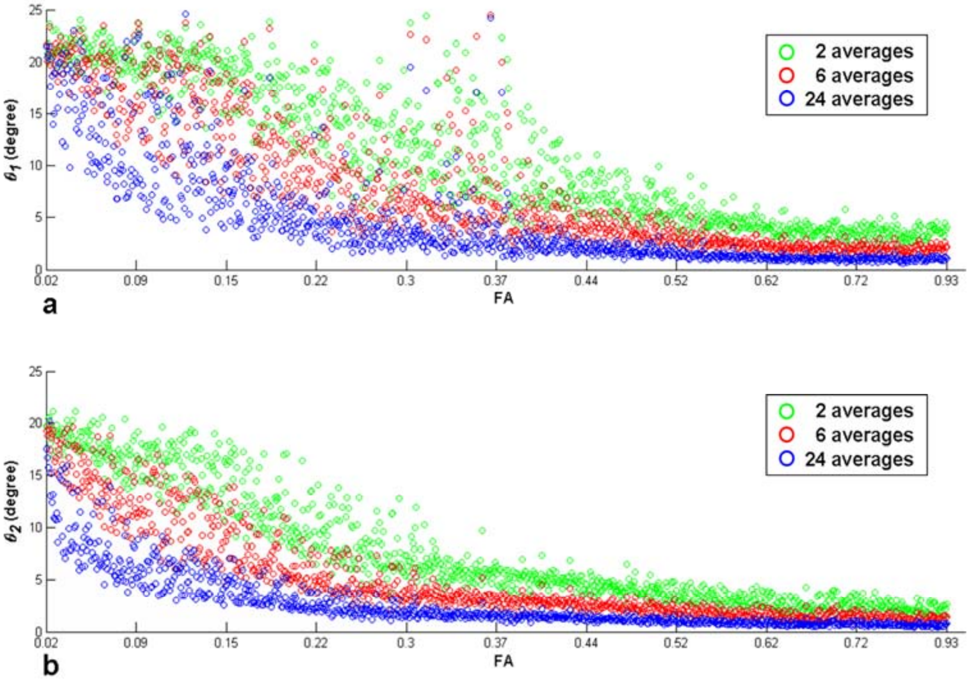

Figure 3.7. Fiber directional uncertainty quantified as cone angles for the major (θ_1, a) and minor axis (θ_2, b) and N_A = 2 (green), 6 (red) and 24 (blue) acquisitions with 200 bootstrap samples are shown over the ROI (Figure 3.2a). The cone angle decreases with increasing N_A (i.e., SNR) and FA for both axes.

3.5.4. Coincidence of the tensor and $\mathbf{v}_1$ *covariance matrix eigenvectors*

The *coincidence angle* is defined as the angle between the major cone axis and the second eigenvector of the ‘true’ diffusion tensor. The simulation results for all voxels in the slice are shown in Figure 3.6 for four different gradient sets, ‘original 6’, ‘original 12’, ‘original 21’ and ’original 92’. Because the major and minor cone axes are orthogonal to each other and lie in the $\{\mathbf{v}_2, \mathbf{v}_3\}$ plane, only the angle between the major cone axis and the second eigenvector is presented. In Figure 3.6(a-d), most of the white matter regions have small coincidence angles, which means the direction of the major cone axis is closer to the second than the third eigenvector of ‘true’ diffusion tensor. Especially large coincidence angles (near 90 degrees) are observed in the genu and splenium of corpus callosum in Figure 3.6a using the ‘original 6’ scheme, however these also become small as the number of gradient vector directions increases, as shown in Figure 3.6(b-d).

Figure 3.8 shows the map of the coincidence angle in the ROI calculated using bootstrap and simulated data. Simulation results (Figure 3.8b) based on the same gradient vector set used to acquire the image data agree closely with the bootstrap results (‘original 6’ with 200 sample and 6 averages; Figure 3.8a).

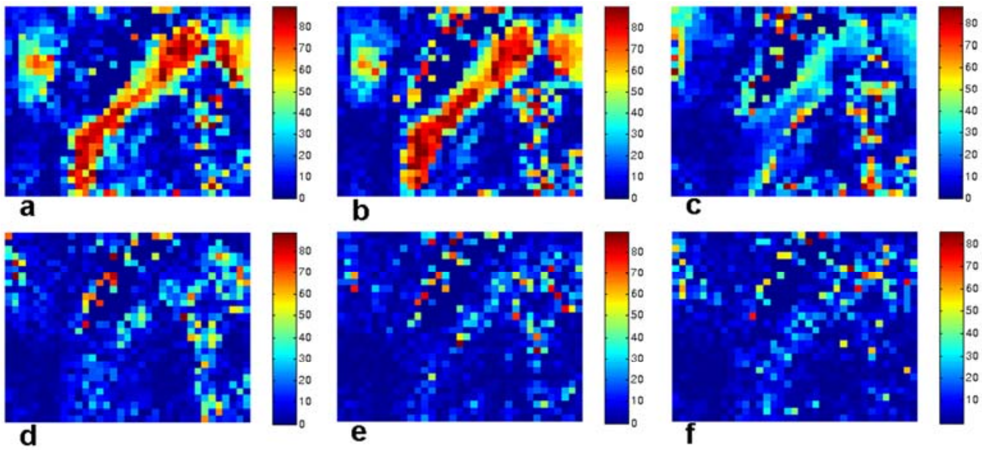

Figure 3.8. Bootstrap and simulation results for the ROI are shown. The coincidence angle map from the bootstrap analysis (200 samples and 6 averages) of actual data using the gradient scheme 'original 6' (a) is in good agreement with simulation results for the same scheme (b). Simulations show the maps of coincidence angle for other gradient schemes: 'rotated 6' (c), 'original 12' (d), 'original 21' (e) and 'original 92' (f). Coincidence angles vary as low-resolution gradient vector sets are rotated (compare b and c). As angular resolution improves, however, coincidence angles converge (d-f).

Both bootstrap (with actual noise) and Monte Carlo simulation (with modeled noise) results indicate nearly 90 degree coincidence angles in the splenium of the corpus callosum. The angular maps with the other sets (Figure 3.8(c-f)), including the 'rotated 6' scheme, show much higher directional coincidence (small angles) across the ROI, including the same regions of the corpus callosum. This implies that coincidence angles are dependent on the number of gradient vectors (angular resolution) as well as the direction of each of the gradient vectors relative to the tensor eigenvectors.

Figure 3.9 shows this relationship in the tensor eigenframe. The variances of the off-diagonal tensor elements (i.e., the elements that produce $\hat{\mathbf{v}}_1$ errors) in the tensor eigenvector frame are shown for a representative voxel in the splenium of the corpus callosum in Figure 3.9.

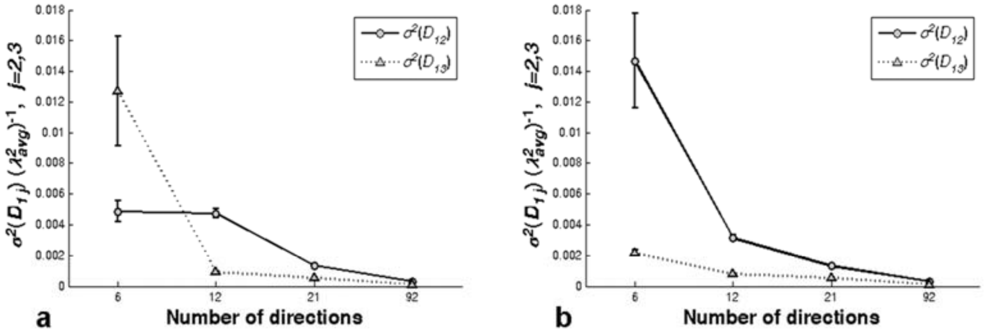

Figure 3.9. Variance of the off-diagonal tensor elements ($\sigma^2(D_{12})$ and $\sigma^2(D_{13})$, scaled by λ_{avg}^2) shown for a representative voxel (10th row and 23rd column in the ROI) in the corpus callosum for 'original' (a) and 'rotated' (b) '6', '12', '21' and '92' gradient vector schemes. These variances, along with eigenvalue contrast, determine the CU cone angles. The variances, and hence cone angles, are dependent on the gradient vector directions at low angular resolution, but converge at high angular resolution.

As expected, the tensor element variances are different for the 'original' and 'rotated' gradient vector schemes at low angular resolution (hence the variation shown in Figure 3.8(b-c)), but converge for high angular resolution gradient sets (as shown in Figure 3.8(d-f)). The limit of infinitely many gradient directions is evaluated in the Appendix A.

3.6. Discussion and Conclusion

In this study, we evaluated the fiber directional uncertainty using bootstrap and perturbation calculations and verified its dependence on diffusion anisotropy and SNR via time domain signal averaging. The notion of time domain averaging for measuring diffusion parameters was suggested by Skare et al. [40] as an alternative to spatial averaging schemes, as used in the Lattice Index (LI) [39,58]. Time domain averaging has the obvious disadvantage of requiring more scanning time, but makes relatively few assumptions as long as a good alignment between diffusion weighted images is guaranteed. Similar improvements in fiber uncertainty are probably achievable using edge-preserving anisotropic spatial smoothing routines developed for DT-MRI [53-55].

The perturbation calculation is in good agreement with the non-parametric bootstrap analysis in estimating fiber directional uncertainty. The slope of the linear fit function and the coefficient of determination are both very close to unity regardless of image SNR. Figures 3.5 and 3.7 show that increasing either image SNR or eigenvalue contrast decreases the fiber directional error in both the major and minor axes, as theory predicts.

We tested the symmetry and normality of the CU as shown in Figures 3.2c and 3.3. Although most of the tested CUs are significantly non-circular (Table 3.1 and Figure

3.2c), some appeared to be nearly symmetric. Most of these near-circular cones, colored dark red in Figure 3.2c, lie in the CSF or regions of likely partial volume averaging of non-parallel fibers. However, in coherent white matter voxels, the cone of uncertainty is generally non-circular. The test for multivariate normal distributions of fiber directional uncertainty is done using the multivariate skewness and kurtosis test [103,104]. When we increased the number of averages from 4 to 12, the number of voxels in the ROI with normal distributions increased from 47 % to 64 % for 200 bootstrap samples. Hence, as SNR increases, the fraction of voxels with multivariate normal error increases. Most of the white matter voxels, however, have normal distributions of $\mathbf{v}_1$ error regardless of the number of averages as shown in Figure 3.3.

The uncertainty in the principal eigenvector is characterized by the major and minor cone angles. As shown in Figures 3.4 and 3.7, the cone angle decreases (i.e., principal eigenvector orientation errors decrease) with increasing voxel SNR and FA. We compared the local fiber orientation when averaging N_A = 2, 6 and 24 acquisitions and using different bootstrap resampling schemes (100, 200, 500 and 1000) over a wide range of FA values (results are shown only for 200 samples). The uncertainties for both the major and minor cone axes decreased with increasing N_A and FA. However, there were no significant changes for any of the bootstrap schemes over 200 samples. The dependence on N_A in our bootstrap analysis agrees with the Monte Carlo simulations by Chang et al. [44].

Figure 3.5 shows the expected dependence of the cone angles on eigenvalue contrast and tensor error. The major and minor cone angles are closely predicted by the eigenvalues of the $\hat{\mathbf{v}}_1$ covariance matrix, $\boldsymbol{\Sigma}_{\mathbf{v}_1}$, defined in (3.9). For the conditions of our experiment, the covariance matrix is nearly diagonal, so the diagonal values are very nearly equal to the eigenvalues. Which of the two diagonal values is larger is determined by the orientation of the gradient vector set relative to the tensor eigenframe for low angular resolution measurements. To understand this phenomenon, consider the case of low angular resolution where one diffusion weighting direction is nearly parallel to $\mathbf{v}_3$, but no measurement direction is correspondingly close to $\mathbf{v}_2$. In this case, the signal is lower for the measurement close to $\mathbf{v}_3$, so the log signal is noisier than that for $\mathbf{v}_2$ (see (A.2) in Appendix A). The increased noise for the log signal produces larger variance in the estimated D_{13} tensor element (see (A.7) and (A.10)). As the number of (uniformly distributed) gradient directions increases, however, directions close to the two eigenvectors, $\mathbf{v}_2$ and $\mathbf{v}_3$, are more equally sampled. In the limit of infinitely high angular resolution, the diagonal values of the $\mathbf{v}_1$ covariance matrix satisfy the relation $\left(\boldsymbol{\Sigma}_{\mathbf{v}_1}\right)_{11} \geq \left(\boldsymbol{\Sigma}_{\mathbf{v}_1}\right)_{22}$, independent of gradient set rotation (see Appendix A). In fact this relation seems to hold for very modest angular resolution measurements. For the gradient schemes tested here, variance of the principal eigenvector in the $\mathbf{v}_2$ direction was larger than the variance in the $\mathbf{v}_3$ direction for all schemes with at least 12 directions (see Figure 3.9). Ignoring very low angular resolution experiments for the moment, the general implication is that fiber tracking errors are always at least as large in the $\mathbf{v}_2$ direction as they are in $\mathbf{v}_3$. Stated differently, the major cone axis is nearly coincident with the major axis of diffusion in the plane perpendicular to $\mathbf{v}_1$.

Lazar and Alexander [49,50] described fiber tract dispersion in the plane perpendicular to the mean fiber axis using the bootstrap method. They quantified tracking errors as a function of distance from the seed point and image SNR. Their analysis showed that the distribution of tract dispersion was typically elliptical rather than circular, and there was high correlation between the direction of the major axis of the ellipse and the second eigenvector of the diffusion tensor. We verified this observation using numerical simulations (Figures 3.6, 8 and 9) and provided a theoretical explanation for the case of many diffusion weighting directions (see the Appendix A). The major axis of the ellipse is not always coincident with the second eigenvector of the tensor at very low angular resolution, for example when one of the gradient vectors is nearly parallel to the third eigenvector of the tensor. This points to an advantage of high angular resolution measurements of the tensor: the orientation of the CU is invariant under rotations of the gradient set. Taken together, the work of Lazar et al. and this study show that the statistical properties of tracking errors can be understood in terms of the cone of uncertainty. This connection has also been made recently by Koay et al. [45].

The CU serves as a convenient conceptual link between local diffusion properties and the reliability of extended fiber paths. In addition, the statistical information contained in the CU can be used to make more realistic probabilistic algorithms for fiber tractography [108] and to evaluate the benefits of diffusion weighted image acquisition and gradient vector schemes for improving fiber path accuracy.

CHAPTER Ⅳ

ROBUST ESTIMATION OF COMPLEX FIBER STRUCTURES

4.1. Overview

Spherical deconvolution has been successful in delineating multiple fiber structures within a voxel in brain white matter *in vivo*. However, in the presence of image noise the estimated fiber orientation distribution (FOD) typically suffers from spurious peaks or lower angular resolution, and hence can be unreliable for further analyses. Given that the deconvolution problem is ill-posed, one method to acquire stabilized solutions is to use numerical regularization. Although there have been several studies of regularization methods for estimation of the FOD, those methods require empirical information, and there is no consensus on the selection of regularization methods for various imaging parameters. In this study, we verified a diverse set of regularization methods for the robust estimation of the FOD using FORECAST. The candidate regularization methods, Tikhonov, truncated and damped singular value decomposition (SVD), are tested with various imaging parameters, constraints, expansion orders and fiber structures with objective determination of the regularization parameter using Monte

Carlo simulation. This study presents robust methods and limitations of estimating the FOD and fiber directions. This may suggest minimum requirements for HARDI studies aimed at the accurate representation of the FOD and fiber tractography over heterogeneous fiber regions.

4.2. Introduction

Diffusion tensor magnetic resonance imaging (DT-MRI) provides information about tissue microstructure *in vivo* based on water molecular diffusion [19-21,26,58,82,109]. However, it is also well known that the diffusion tensor is inaccurate in regions with multiple or heterogeneous fibers, because the diffusion tensor is a voxel-averaged quantity and indicates only a single direction of maximal diffusion [28,29,59-63,65-67]. Many other approaches using high angular resolution diffusion (HARD) encoding, e.g., diffusion spectrum imaging (DSI) [66,68] and q-ball imaging (QBI) [69] etc., can identify multiple fiber directions. Spherical deconvolution (SD) [73] also has been successfully used to characterize multiple fiber orientations within a single voxel [76-79]. Another SD method, named FORECAST (Fiber ORientation Estimated using Continuous Axially Symmetric Tensors), has shown better performance than many of the other methods in representing multiple fibers with relatively higher angular resolution at lower *b*-value [74,75]. However, the reliable estimation of the fiber orientation distribution (FOD) function is difficult in the presence of noise in the diffusion weighted imaging data [76-78]. Noise results in spurious peaks (or alternatively lower angular resolution) in the FOD and hence makes it unreliable for further analyses. Given that the deconvolution problem is typically ill-posed, one way to obtain stabilized solutions is to use numerical regularization [80,110]. There have been many regularization approaches proposed for the reliable estimation of the FOD function [73,76-78]. But those methods require empirical information about filter factors or regularization parameters. Recently, an objective determination of the regularization parameter, i.e., generalized cross validation, has been suggested with use of singular value decomposition [79,89]. Though this method has successfully demonstrated robust estimation of the FOD function, there has not been any consensus on the best selection of regularization method. In this simulation study, we use FORECAST to compare diverse regularization methods used with various imaging parameters, expansion orders and fiber structures with an objective determination of the regularization parameter.

4.3. Methods

4.3.1. Regularization method

The formalism for regularizing FORECAST in this study is given in (4.1)

$$\begin{aligned}\mathbf{x}_\alpha &= \arg\min\left\{\|\mathbf{A}\mathbf{x}-\mathbf{g}\|_2^2 + \alpha^2\|\mathbf{L}\mathbf{x}\|_2^2\right\} \\ &= \left(\mathbf{A}^\mathsf{T}\mathbf{A}+\alpha^2\mathbf{L}^\mathsf{T}\mathbf{L}\right)^{-1}\mathbf{A}^\mathsf{T}\mathbf{g}\end{aligned}, \tag{4.1}$$

here,

$$\mathbf{A} = \mathbf{Y}\cdot\mathbf{C}, \tag{4.2}$$

$$\mathbf{Y} = \begin{bmatrix} Y_{0,0}(\theta_1,\phi_1) & Y_{1,-1}(\theta_1,\phi_1) & Y_{1,0}(\theta_1,\phi_1) & \cdots & Y_{l_{\max},l_{\max}}(\theta_1,\phi_1) \\ Y_{0,0}(\theta_2,\phi_2) & Y_{1,-1}(\theta_2,\phi_2) & \cdots & \cdots & \vdots \\ Y_{0,0}(\theta_3,\phi_3) & \vdots & \ddots & \cdots & \vdots \\ \vdots & \vdots & \vdots & \ddots & \vdots \\ Y_{0,0}(\theta_m,\phi_m) & Y_{1,-1}(\theta_m,\phi_m) & Y_{1,0}(\theta_m,\phi_m) & \cdots & Y_{l_{\max},l_{\max}}(\theta_m,\phi_m) \end{bmatrix}, \tag{4.3}$$

$$\mathbf{C} = S_0\begin{bmatrix} C_0 & 0 & \cdots & \cdots & 0 \\ 0 & C_1 & 0 & \cdots & \vdots \\ \vdots & 0 & \ddots & 0 & \vdots \\ \vdots & \cdots & 0 & \ddots & 0 \\ 0 & \cdots & \cdots & 0 & C_{l_{\max}} \end{bmatrix}, \tag{4.4}$$

$$\mathbf{x} = \begin{bmatrix} p_{0,0} & p_{1,-1} & p_{1,0} & \cdots & p_{l_{\max},l_{\max}} \end{bmatrix}^\mathsf{T}, \tag{4.5}$$

and **g** is the diffusion weighted (DW) signal, **Y** is a matrix of spherical harmonics up to maximum order $l_{\max}$ evaluated at m diffusion gradient orientations, S_0 is the non-DW signal, C_l is the kernel function as in (2.27), **x** gives the spherical harmonic coefficients of the FOD, **L** is a side constraint matrix such as a function of the FOD curvature, gradient, 1st or 2nd order derivative operator or the identity matrix **I**, and α is the regularization parameter. Because toolboxes are readily available for use with real matrices (see [80]), we generated real spherical harmonics based on Ritchie et al. [111]. The solution for this problem can be categorized according to whether **L**=**I** or **L**≠**I** and the use of singular value decomposition (SVD) (without constraint) or generalized singular value decomposition (GSVD) (with constraint). The SVD of **A** is,

$$\mathbf{A} = \mathbf{U} \cdot \mathbf{S} \cdot \mathbf{V}^{\mathrm{T}}, \tag{4.6}$$

where **S** is diagonal with singular values σ_i (i = 1, ..., n).

The GSVD of **A** and **L** are

$$\mathbf{A} = \mathbf{U} \cdot \begin{bmatrix} \mathbf{\Sigma} & \mathbf{0} \\ \mathbf{0} & \mathbf{I} \end{bmatrix} \cdot \mathbf{X}^{-1}, \tag{4.7}$$

$$\mathbf{L} = \mathbf{V} \cdot \begin{bmatrix} \mathbf{M} & \mathbf{0} \end{bmatrix} \cdot \mathbf{X}^{-1}, \tag{4.8}$$

here, **Σ** and **M** are diagonal matrices with singular values σ_i and μ_i (i = 1, ..., n), respectively. The matrices **U** and **V** and singular values σ_i in (4.6) and (4.7)-(4.8) are different. With these approaches it is possible to calculate several regularized solutions, $\mathbf{x}_{\mathrm{reg}}$, for physically meaningful estimates of the FOD as follows.

1. Tikhonov (TIKH) solution:

$$\mathbf{x}_{\mathrm{reg}} = \sum_{i=1}^{n} f_i \frac{\mathbf{U}_i^{\mathrm{T}} \mathbf{g}}{\sigma_i} \mathbf{V}_i, \quad f_i = \frac{\sigma_i^2}{\sigma_i^2 + \alpha^2} \text{ for } \mathbf{L} = \mathbf{I}, \tag{4.9}$$

$$\mathbf{x}_{\mathrm{reg}} = \sum_{i=1}^{p} f_i \frac{\mathbf{U}_i^{\mathrm{T}} \mathbf{g}}{\sigma_i} \mathbf{X}_i + \sum_{i=p+1}^{n} \left(\mathbf{U}_i^{\mathrm{T}} \mathbf{g} \right) \mathbf{X}_i, \quad f_i = \frac{\gamma_i^2}{\gamma_i^2 + \alpha^2} \text{ for } \mathbf{L} \neq \mathbf{I}, \tag{4.10}$$

here, p is the rank of matrix **A**.

2. Truncated SVD (TSVD) (4.11) or Truncated generalized SVD (TGSVD) (4.12) solution:

$$\mathbf{x}_{\mathrm{reg}} = \sum_{i=1}^{k} \frac{\mathbf{U}_i^{\mathsf{T}} \mathbf{g}}{\sigma_i} \mathbf{V}_i \, , \tag{4.11}$$

$$\mathbf{x}_{\mathrm{reg}} = \sum_{i=p-k+1}^{p} \frac{\mathbf{U}_i^{\mathsf{T}} \mathbf{g}}{\sigma_i} \mathbf{X}_i + \sum_{i=p+1}^{n} \left(\mathbf{U}_i^{\mathsf{T}} \mathbf{g} \right) \mathbf{X}_i \, , \tag{4.12}$$

here, $k < p$ is truncation order.

3. Damped SVD (DSVD) (4.13) or Damped generalized SVD (DGSVD) (4.14) solution:

$$\text{same as (4.9) with } f_i = \frac{\sigma_i}{\sigma_i + \alpha} \, , \tag{4.13}$$

$$\text{same as (4.10) with } f_i = \frac{\gamma_i}{\gamma_i + \alpha} \, , \tag{4.14}$$

with generalized singular value $\gamma_i = \sigma_i / \mu_i$, $\sigma_i^2 + \mu_i^2 = 1$.

The candidate methods used in this study are listed below and compared with the standard least square method of calculating **x**,

1. Least-square (LS),
2. TIKH without and with constraint,
3. TSVD without and with (TGSVD) constraint,
4. DSVD without and with (DGSVD) constraint.

Other than these, there were published methods using TIKH [77] and Super-resolution

[78], both with constraint.

4.3.2. Constraint and parameter determination

The constraints for regularization are integration of the square of the Laplacian of the FOD (sqLap) (4.15), integration of the square of the gradient of the FOD (sqGrad) (4.16), or the magnitude of the negative part of the FOD function (negFOD):

$$\int_0^{2\pi}\int_0^{\pi}\left|\nabla^2 P(\theta,\phi)\right|^2 \sin\theta d\theta d\phi = \sum_l \sum_m \left[l(l+1)\right]^2 \left|p_{lm}\right|^2 , \tag{4.15}$$

$$\int_0^{2\pi}\int_0^{\pi}\left|\nabla P(\theta,\phi)\right|^2 \sin\theta d\theta d\phi = \sum_l \sum_m \left[l(l+1)\right] \left|p_{lm}\right|^2 . \tag{4.16}$$

Equations (4.15) and (4.16) can be generalized as,

$$\int_{S^2}\left|f^{(s)}(\omega)\right|^2 d\omega = \sum_l \sum_m \left[l(l+1)\right]^s \left|f_{lm}\right|^2 , \tag{4.17}$$

as shown in [112], and each of the constraint functions has been used for sqLap [113,114] and sqGrad [79]. All the methods, except least-square, can be used with generalized cross validation (GCV) or the L-curve method to determine the regularization parameter without user-interaction or *a prior* knowledge [80,110].

4.3.3. Simulation

Because there are too many combinations of methods for regularization, constraints, parameter determination and imaging parameters, e.g., number of fibers, SNR, expansion order, diffusion encoding direction, etc., two levels of simulations were performed to determine the best methods. The first simulation is done to determine the constraint (sqLap, sqGrad and negFOD) and regularization parameter (GCV and L-curve) with imaging parameters as follows: unit magnitude of non-DW signal, mean diffusivity = 0.7×10^{-3} mm^2/s, *b*-value = 2000 s/mm^2, radial diffusivity normalized by mean diffusivity = (0.5, 0.5) for each of two fibers, volume fraction = (0.5, 0.5), maximum spherical harmonic expansion order of 6 with real and even spherical harmonics used, SNR = 33, 92 diffusion gradient directions, and fiber separation angle of 64 degrees. The simulation is performed 1000 times as shown in Figure 4.1-4.2.

Provided the best constraint and method for determining the regularization parameter from the first simulation, the second simulation is performed with the chosen methods applied to each of the imaging parameters. The following imaging parameters were considered using Monte Carlo simulation; number of fibers = 2 and 3, SNR = 30, 60 and 90, maximum spherical harmonic expansion order for the analysis = 4 and 6 (DW signal is generated at higher order, i.e., 12th order for the approximation of an experimental signal), number of diffusion weighting gradient directions = 92 and 162, *b*-value = 1000, 2000 and 3000 and fiber separation angle = 30, 50 and 70 degrees (between fiber 1-2 and fiber 1-3 for three fiber case) with 200 trials. To apply the negFOD constraint, the negative FOD values were found over 752 directions (5th order tessellation of Dodecahedron with symmetric 376 directions on a unit sphere) at the same order of expansion. Then the estimates of the fiber directions were obtained by searching for local maxima over the FOD in each trial. The search started at the true fiber direction corresponding to each fiber bundle in the simulation.

4.4. Results

4.4.1. Determination of constraint and method for regularization

Simulations were performed with three constraints (sqLap, sqGrad and negFOD) using the methods for estimating the regularization parameter (GCV and L-curve) as shown in Figure 4.1 and 4.2. The regularizations were applied using Hansen's Matlab regularization toolbox [80]. The TSVD method is not included in Figure 4.1 and 4.2 because the primary purpose in this simulation is to evaluate the usefulness of the constraints using GCV and L-curve, but TSVD discards some of the singular values in the regularization making it difficult to fully evaluate the performance due to the combination of the constraint and the method for the determination of a regularization parameter.

Figure 4.1 shows the simulation results using TIKH and DSVD with GCV and constraints. As shown in Figure 4.1a-b, TIKH and DSVD provide FOD functions aligned along the true fiber directions (red and blue bar) with small to intermediate noise around the origin.

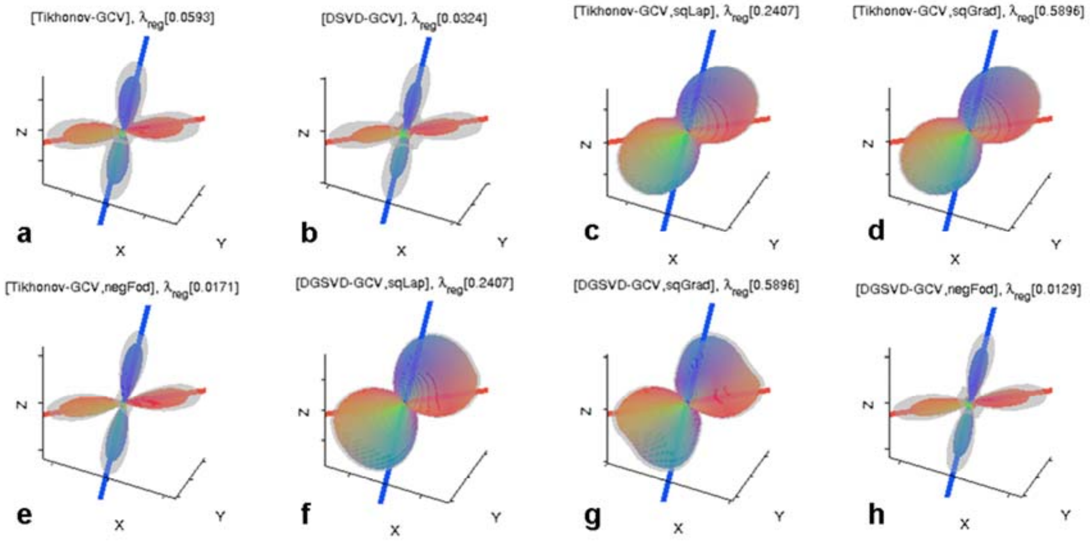

Figure 4.1. Simulation results for FOD plot are shown with and without various constraints using GCV. The true fiber directions are shown in blue and red sticks in each subplot. The regularization methods are TIKH-GCV (a), DSVD-GCV (b), TIKH-GCV-sqLap (c), TIKH-GCV-sqGrad (d), TIKH-GCV-negFOD (e), DSVD-GCV-sqLap (f), DSVD-GCV-sqGrad (g) and DSVD-GCV-negFOD (h). The mean FOD over all trials is shown in color, the mean + one standard deviation is shown as a partially transparent, gray surface. λ_{avg} values are the mean regularization parameters over 1000 trials. Using sqLap and sqGrad constraints FOD shape is over-regularized as there are no noticeable peaks along the true fiber directions as shown in (c)-(d) and (f)-(g) for both of the TIKH and DSVD methods.

However, with sqLap and sqGrad constraints as shown in Figure 4.1c-d and f-g the shape of FOD function is over-regularized and there is no noticeable peak around the true fiber directions. Figure 4.1e and 4.1h are with the negFOD constraint and they reveal sharper FOD peaks and reduced noise around the origin and along the true fiber directions.

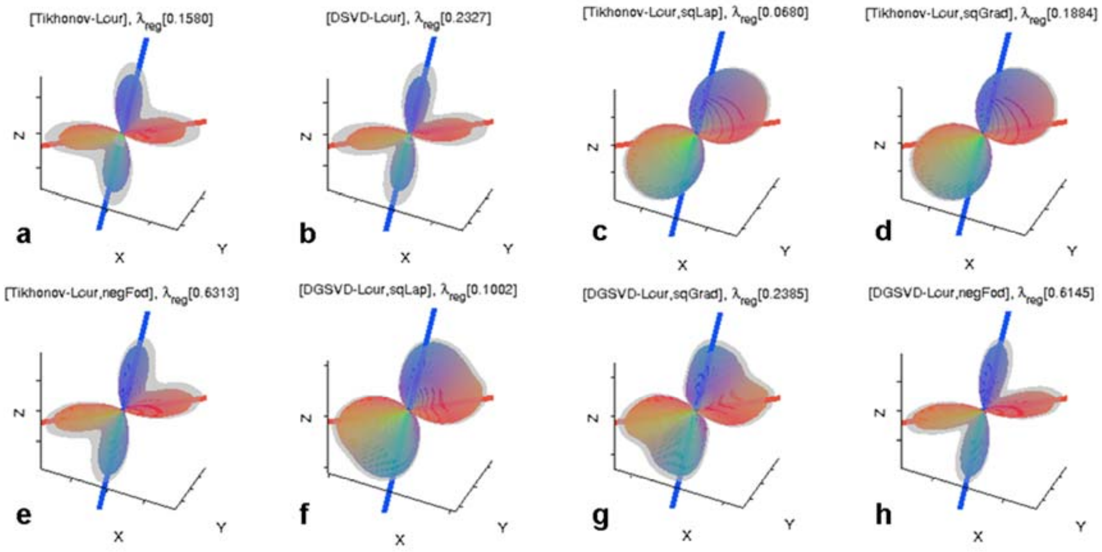

Figure 4.2. Simulation results for FOD plot are shown with and without various constraints using L-curve (Lcur). The true fiber directions are shown in blue and red sticks in each figure. The regularization methods are TIKH-Lcur (a), DSVD-Lcur (b), TIKH-Lcur-sqLap (c), TIKH-Lcur-sqGrad (d), TIKH-Lcur-negFOD (e), DSVD-Lcur-sqLap (f), DSVD-Lcur-sqGrad (g) and DSVD-Lcur-negFOD (h). The mean FOD over all trials is shown in color, the mean + one standard deviation is shown as a partially transparent, gray surface. λ_{avg} values are the mean regularization parameters over 1000 trials. Using sqLap and sqGrad constraints FOD shape is over-regularized as there are no noticeable peaks along the true fiber directions as shown in (c)-(d) and (f)-(g) for both of the TIKH and DSVD methods.

Figure 4.2 shows the simulation results as done in Figure 4.1. Figure 4.2a-b show TIKH and DSVD results using the L-curve method without constraint. They show FOD functions aligned along the true fiber directions with reduced noise at the center but also with decreased resolution for each fiber bundle compared with Figure 4.1a-b. Figure 4.2c-d and f-g with sqLap and sqGrad constraints also show the over-regularized FOD function without any significant fiber peak around the true fiber directions. In Figure 4.2e and 4.2h using the negFOD constraint provides FOD peaks along the true directions and reduced noise as shown in Figure 4.1e and 4.1h.

From Figures 4.1 and 4.2 the FOD shapes using GCV generally have smaller regularization parameters and narrower FOD peaks than those using L-curve when negFOD and no constraints are used. However, with constraints such as sqLap and sqGrad, GCV generates much larger regularization parameter than that using L-curve. In both cases of using GCV and L-curve with sqLap and sqGrad constraint, the FODs are over-regularized and there are no noticeable peaks for the true fiber directions. Therefore, in this study only the negFOD and no constraints cases are considered with the regularizations using TIKH, TSVD and DSVD. Although the L-curve method generates comparable regularization parameters to those of GCV theoretically [80], the simulation results using L-curve generate much smoother FOD functions with relatively lower angular resolution than those using GCV which have negligible spikes around the origin, in general. Considering the fiber tractography, however, having sharper peaks for each fiber bundle with negligible spikes around the origin may be more beneficial than having wider peaks for each bundle with commensurate noise at the origin. Also because the primary purpose of this study is to represent the FOD and fiber direction reliably in the presence of noise, the use of L-curve may suppress possible small fiber bundles due to its characteristic over-regularization relative to GCV. Then in this study, GCV is used for the objective estimation of regularization parameter for all the candidate methods with and without negFOD constraint. Removing the low amplitude bundles around the origin of the FOD function can be done by applying a threshold, e.g., 10 % of the mean FOD amplitude as done in Tournier et al. [78].

4.4.2. Estimation of FOD

Using the most promising methods identified in §4.4.1, more detailed simulations are performed based on the parameters mentioned below.

4.4.2.1. Fiber separation angle

Figure 4.3 shows the simulation results using various regularization methods with varying separation angles (30, 50 and 70 degrees from left, middle and right within each subplot). The simulation is done with the following parameters: two fibers, SNR = 60, 6th order expansion, 92 diffusion encoding directions, and *b*-value = 2000 s/mm^2.

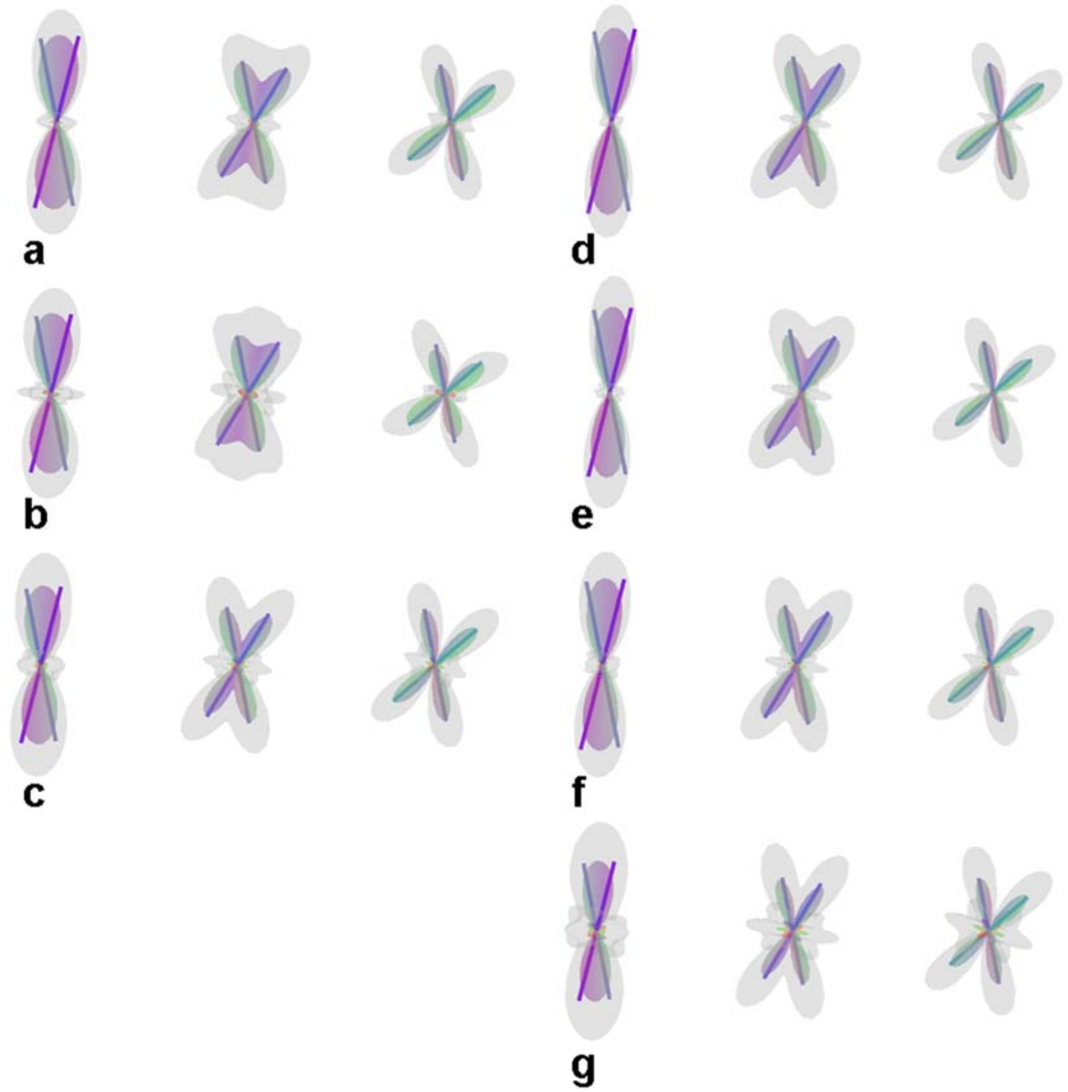

Figure 4.3. The FOD function is shown for each separation angle (30, 50 and 70 degrees in the left, middle and right side in each subplot) using 6th order for each regularization method, i.e., TIKH (a), TSVD (b), DSVD (c), TIKH-negFOD (d), TSVD-negFOD (e), DSVD-negFOD (f) and LS (g). The color of the FOD and fiber is a mixture of red, blue and green based on their direction. The FOD functions for the mean (mixed color) and the mean plus twice the standard deviation (gray) are plotted using 6th order together with

(Figure 4.3. Continued.)
the true fiber direction (colored stick).

In Figure 4.3 each plot represents the mean and twice the standard deviation added to the mean FOD from all the trials with the true fiber directions shown as sticks. The color in the plot varies according to the direction of the mean FOD and true fibers as a mixture of red, blue and green. The mean plus twice the standard deviation of the FOD is shown in gray. Each of the regularization results listed above is plotted in Figure 4.3, i.e., TIKH (a), TSVD (b), DSVD (c), TIKH-negFOD (d), TSVD-negFOD (e), DSVD-negFOD (f) and LS (g). Considering the LS result in Figure 4.3g as a reference, all the other results using regularization show significantly reduced standard deviation for all the separation angles. Though Figure 4.3g shows more FOD noise around the origin than the others, the mean FOD is along the true fiber direction as are the other FODs. All the peaks of the mean FOD indicate the true fiber directions at the angle of 70 degrees as shown in the right side of each subplot, but there are small deviations at 50 degrees in the middle and no distinguishable fiber bundles at 30 degrees in the left side of each subplot (see Figures 4.10 and 4.11 for the estimation of the true fiber directions using LS, TIKH and DSVD with and without constraint).

Figure 4.4 shows FOD plots using the same parameters except the expansion order (using 4th). In Figure 4.4 the LS (Figure 4.4a) and TIKH (Figure 4.4b) results show smaller standard deviation than those shown in Figure 4.3g and 4.3a, respectively. However, the angular resolution represented by the FOD shown in Figure 4.4a and b is much lower than that in Figure 4.3g and a, especially for 50 degrees separation as shown in the middle of each subplot.

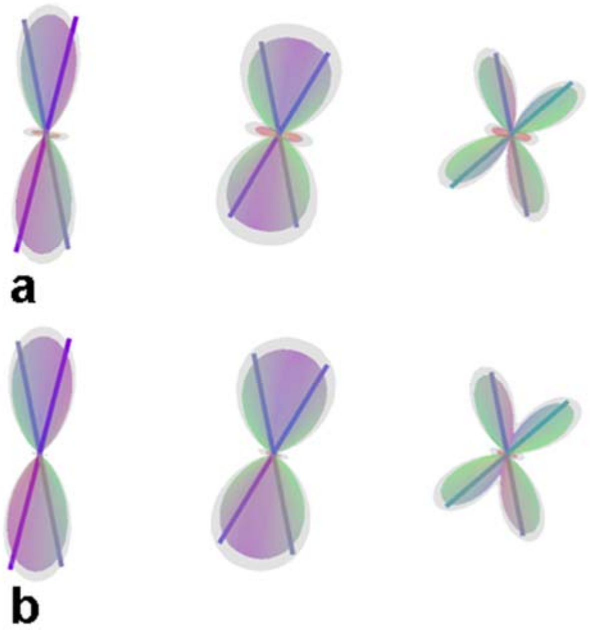

Figure 4.4. The FOD function shows the results for each separation angle (30, 50 and 70 degrees in the left, middle and right side in each subplot) using 4th order expansion for the LS (a) and TIKH (b) regularization methods. The color for the FOD and fiber is a mixture of red, blue and green based on their direction. The FOD functions for the mean (mixed color) and the mean plus twice the standard deviation (gray) are plotted together with the true fiber directions (colored sticks).

Also the direction of the FOD corresponding to each fiber appears to be significantly biased compared to the true fiber directions even at 70 degrees separation using 4th order expansion. Therefore, for the accurate representation of fiber distributions the minimum angular separation between fibers must be greater approximately than 30~50 degrees using 6th order expansion.

4.4.2.2. Expansion order

Figure 4.5 shows the effect of expansion order using 4th and 6th order and two fibers, SNR = 60, 92 diffusion encoding directions, *b*-value = 2000 s/mm^2, and separation angle of 50 degrees. As the expansion order increases, the susceptibility of FOD to image noise increases as shown in each result. Using 4th order, FOD has relatively small standard deviation compared the 6th order function. However, the fiber bundles are poorly (or not at all) distinguished in the FOD. As the expansion order increases from 4 to 6, the mean FOD has discernable fiber peaks along each of the true fiber directions. However, the effect of noise is also amplified as the standard deviation of the FOD increases around the mean FOD. Using the negFOD constraint with 6th order expansion as in Figure 4.5d-f all three FODs show similar and improved shapes.

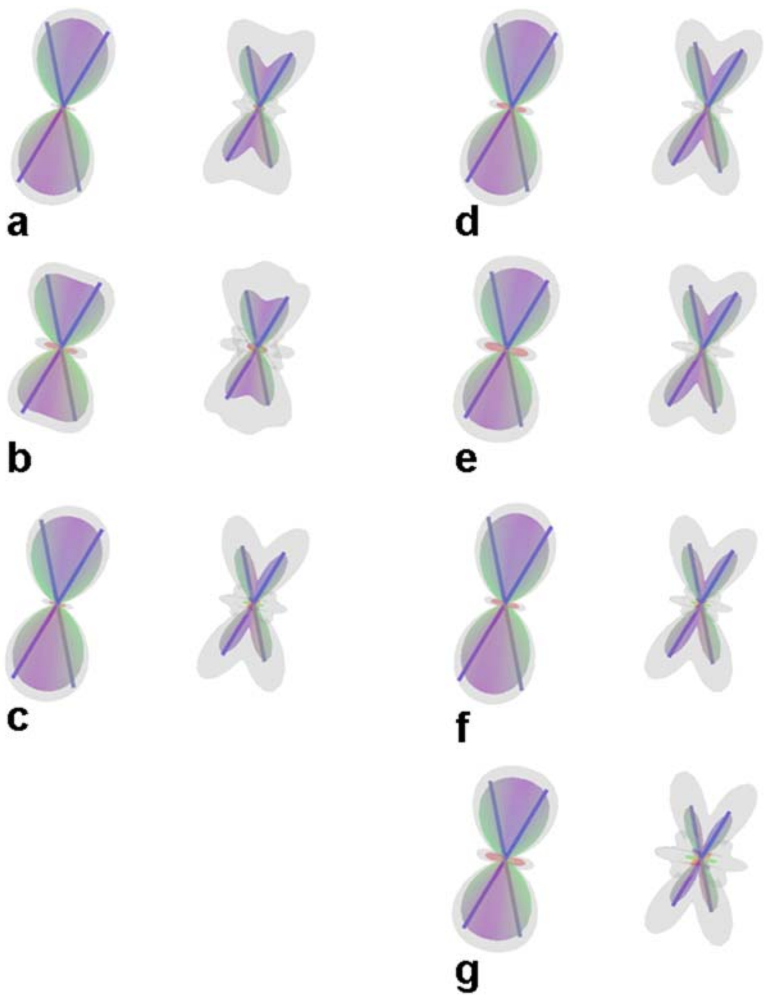

Figure 4.5. The FOD function for each expansion order, 4th and 6th order in the left and the right side in each subplot, for each regularization method: TIKH (a), TSVD (b), DSVD (c), TIKH-negFOD (d), TSVD-negFOD (e), DSVD-negFOD (f) and LS (g). The color for the FOD and fiber is a mixture of red, blue and green based on their direction. The FOD functions for the mean (mixed color) and the mean plus twice the standard deviation (gray) are plotted with the true fiber directions (colored sticks).

4.4.2.3. b-value

Figure 4.6 shows the FOD plots for *b*-values of 1000, 2000 and 3000 s/mm^2 with two fibers, SNR = 60, 6th order expansion, 92 diffusion encoding directions and separation angle of 50 degrees.

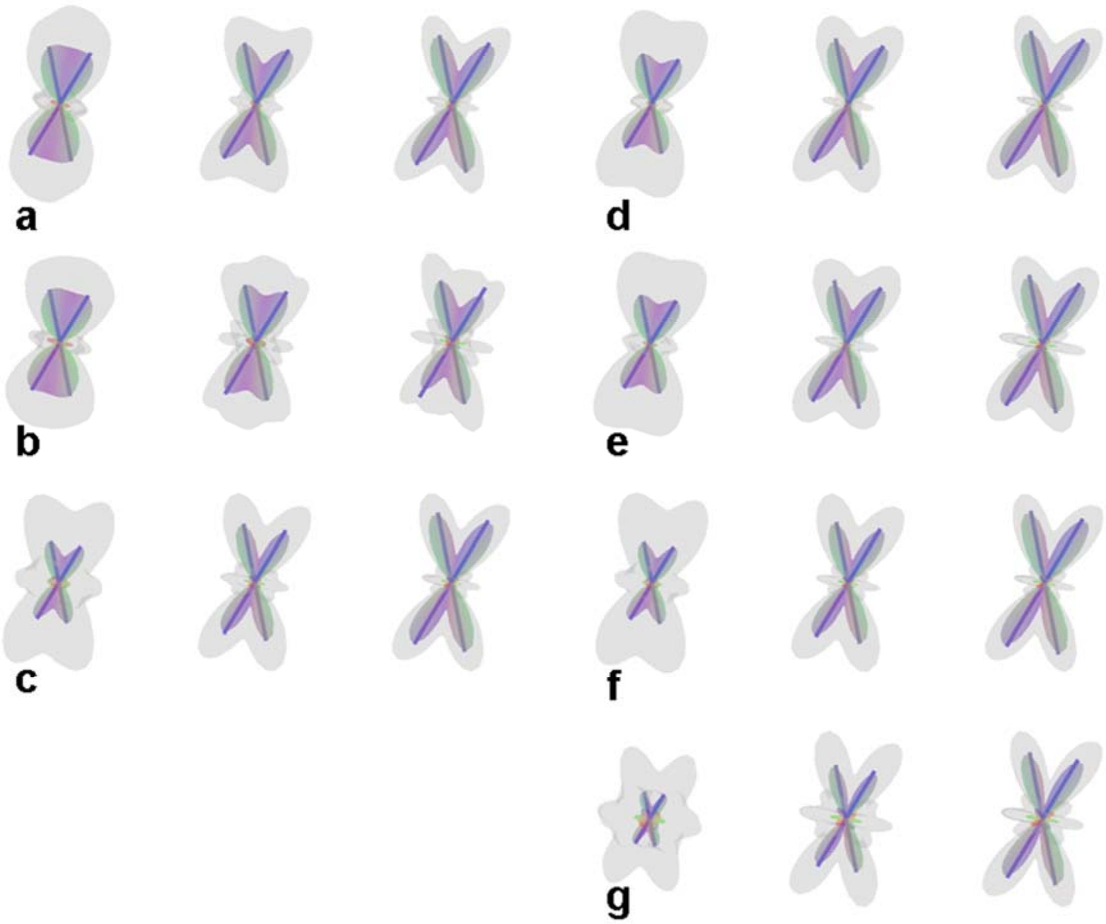

Figure 4.6. The FOD function shows the result for each *b*-value (1000, 2000 and 3000 s/mm^2 in the left, middle and right side in each subplot) using 6th order expansion for each regularization method: TIKH (a), TSVD (b), DSVD (c), TIKH-negFOD (d), TSVD-negFOD (e), DSVD-negFOD (f) and LS (g). The color for the FOD and fiber is a mixture of red, blue and green based on their direction. The FOD functions for the mean (mixed color) and the mean plus twice the standard deviation (gray) are plotted with the true fiber directions (colored sticks). The mean diffusivity of each fiber is 0.7×10^{-3} mm^2/s and the radial diffusivity is 0.5 times the mean.

Most of the results show reduced standard deviation of the FOD as *b*-value increases from 1000 to 3000 s/mm^2. The angular resolution between fibers also increases with increasing *b*-value and with the use of regularization. DSVD and LS as in Figure 4.6c, f and g show relatively higher angular resolution than the other results at *b*-value of 1000 s/mm^2, but they show especially large standard deviations.

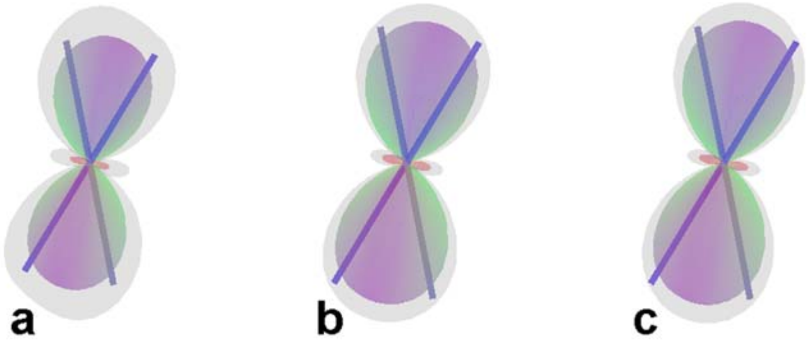

Figure 4.7. The FOD is plotted with 4th order using TIKH-negFOD with varying *b*-value (1000 (a), 2000 (b) and 3000 s/mm^2 (c)). The color for the FOD and fiber is a mixture of red, blue and green based on their direction. The FOD functions for the mean (mixed color) and the mean plus twice the standard deviation (gray) are plotted with the true fiber directions (colored sticks).

Though TSVD results with negFOD (Figure 4.6e) appear to be comparable to the other results, the FOD without the constraint (Figure 4.6b) shows large variations on the function even at *b*-value of 3000 s/mm^2. Using lower expansion order (order 4) does not guarantee any improvements in FOD function. Figure 4.7 shows an example using TIKH-negFOD, and there are no recognizable fiber peaks in the FOD along the true fiber directions. All the other results are similar at the same order (not shown).

4.4.2.4. Diffusion encoding directions

Figure 4.8 shows the results for diffusion encoding directions (92 and 162) with two fibers, SNR = 60, 6th order expansion, *b*-value = 2000 s/mm^2, and separation angle of 50 degrees. TIKH (Figure 4.8a and d) and TSVD (Figure 4.8b and e) show much improved angular resolution and increased standard deviation around the origin with a larger number of diffusion encoding directions and constraint. However, the improvements in DSVD (Figure 4.8c and f) are less marked. The same simulation analyzed at 4th order does not generate any major differences in FOD shape, nor are there noticeable fiber peaks along the true fiber directions (results not shown).

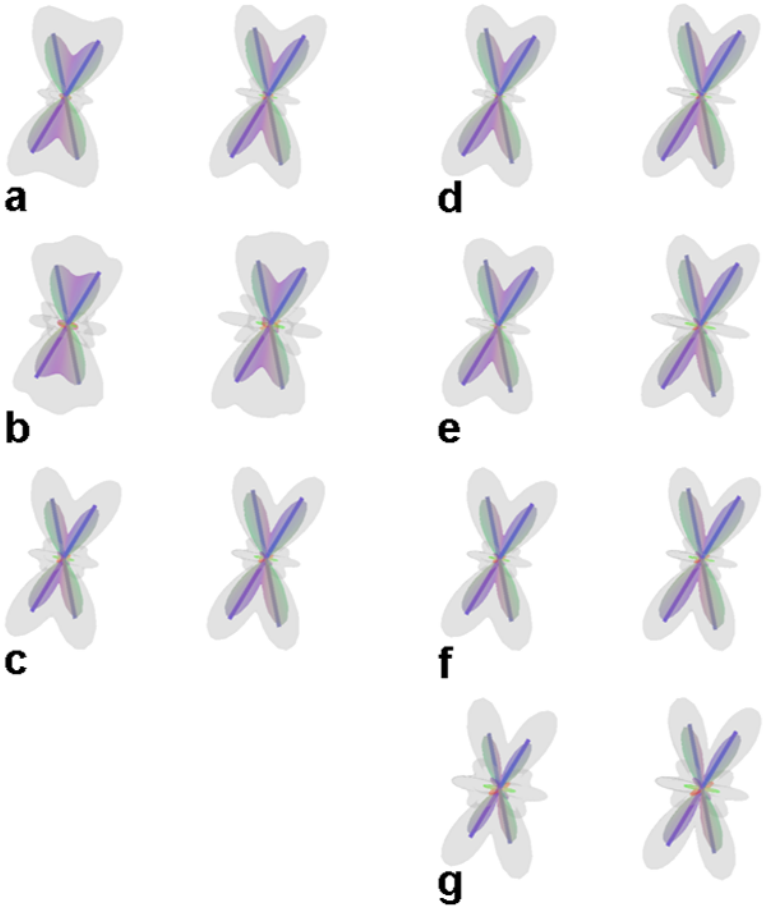

Figure 4.8. The FOD function for 92 and 162 diffusion encoding directions in the left and right side in each subplot, respectively, using 6th order for each regularization method: TIKH (a), TSVD (b), DSVD (c), TIKH-negFOD (d), TSVD-negFOD (e), DSVD-negFOD (f) and LS (g). The color of the FOD and fiber is a mixture of red, blue and green based on their direction. The FOD functions for the mean (mixed color) and the mean plus twice the standard deviation (gray) are plotted with the true fiber directions (colored sticks).

4.4.2.5. Number of fibers

Figure 4.9 represents the results for the number of fibers (2 and 3) with SNR = 60, 6th order expansion, 92 directions, *b*-value = 2000 s/mm^2, and separation angle of 50 degrees. Though there are noticeable differences in FOD between regularization results for two fiber case (e.g., Figure 4.5), no significant differences are observed for three fiber case.

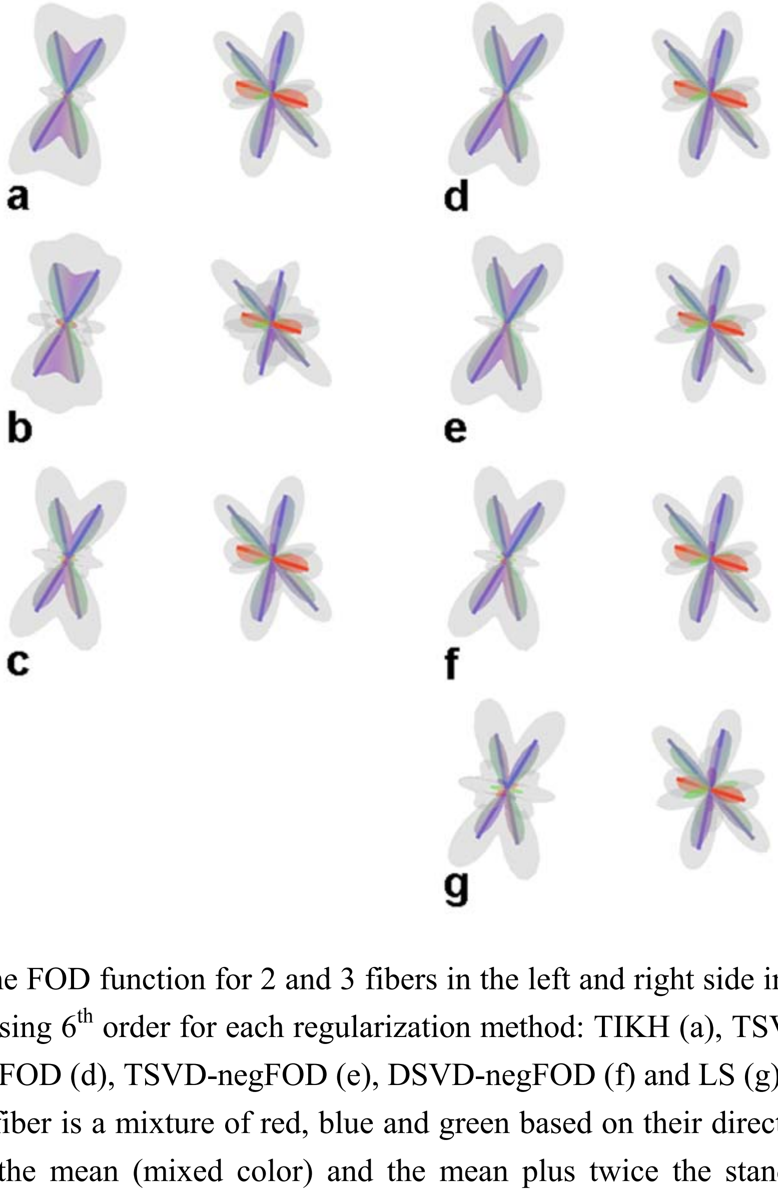

Figure 4.9. The FOD function for 2 and 3 fibers in the left and right side in each subplot, respectively, using 6th order for each regularization method: TIKH (a), TSVD (b), DSVD (c), TIKH-negFOD (d), TSVD-negFOD (e), DSVD-negFOD (f) and LS (g). The color for the FOD and fiber is a mixture of red, blue and green based on their direction. The FOD functions for the mean (mixed color) and the mean plus twice the standard deviation (gray) are plotted with the true fiber directions (colored sticks).

TIKH (Figure 4.9a and d) and DSVD (Figure 4.9c and f) show almost identical FODs for three fibers, and TSVD (Figure 4.8e) and LS (Figure 4.8g) also have three comparable fiber FODs. TSVD (Figure 4.8b) shows even larger standard deviation than that of LS (Figure 4.9g), but the use of constraint (Figure 4.9e) generates a comparable three-fiber FOD as TIKH and DSVD with relatively larger error perpendicular to the third (red) fiber.

4.4.3. Estimation of fiber direction

The true fiber directions are estimated for each regularization result. However, as shown in §4.4.2, TSVD has relatively lower angular resolution and larger standard deviation of the FOD than the other regularization results. Therefore, only the TIKH and DSVD methods are compared on the basis of the accuracy of fiber direction estimates.

4.4.3.1. Fiber separation angle

Figure 4.10 shows the estimation of fiber directions using LS for the two fiber case for varying separation angle for 200 trials. The simulation is done with SNR = 60, 6th order expansion, 92 diffusion encoding directions, and *b*-value = 2000 s/mm^2 as used in §4.4.2.1. Estimates for fiber 1 are in red (*) and fiber 2 in blue (o) with true fiber directions marked in black (×).

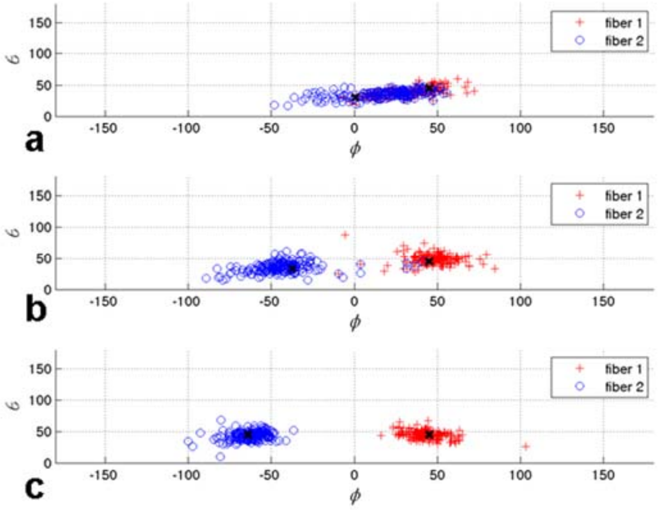

Figure 4.10. Estimates of fiber direction using LS are plotted for each separation angle: 30 degrees (a), 50 degrees (b) and 70 degrees (c). Results for 200 trials are shown for fiber 1 in red (+) and fiber 2 in blue (o) with the true fiber directions (×) with θ (vertical) and ϕ (horizontal) axes in degrees.

Figure 4.11 shows the regularization results with TIKH (a), TIKH-negFOD (b), DSVD (c) and DSVD-negFOD (d). For the separation angle of 30 degrees, the LS result (Figure 4.10a) shows large dispersion of estimations over the true fiber directions. With increased separation angle to 50 degrees, estimations for each fiber direction are crowded around the true directions (Figure 4.10b). At the largest angle (70 degrees) the estimates are concentrated at each fiber direction as presented in Figure 4.3g. At 30 degrees in Figure 4.11, most of the estimations of fiber directions are between the true directions. With increased angles, however, the estimations become more concentrated about each of the true fiber directions as shown in the middle and bottom plots in Figure 4.11.

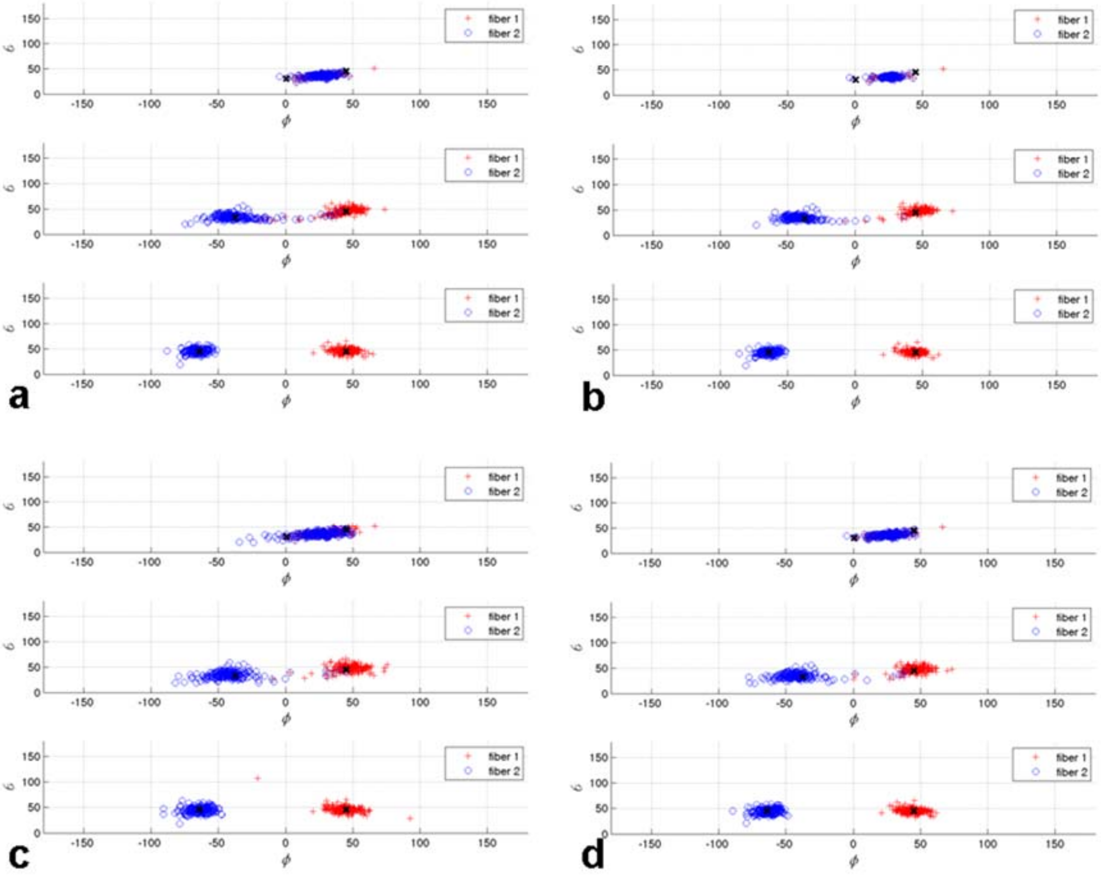

Figure 4.11. Estimates of fiber direction using TIKH (a), TIKH-negFOD (b), DSVD (c) and DSVD-negFOD (d) are plotted for each separation angle: 30 degrees (top), 50 degrees (middle) and 70 degrees (bottom) in each subplot. Results for 200 trials are shown for fiber 1 in red (+) and fiber 2 in blue (o) with the true fiber directions in black (×) on θ (vertical) and ϕ (horizontal) axes in degrees.

Using 4th order expansion with TIKH-negFOD (Figure 4.12), the directional estimates are less scattered than those at 6th order.

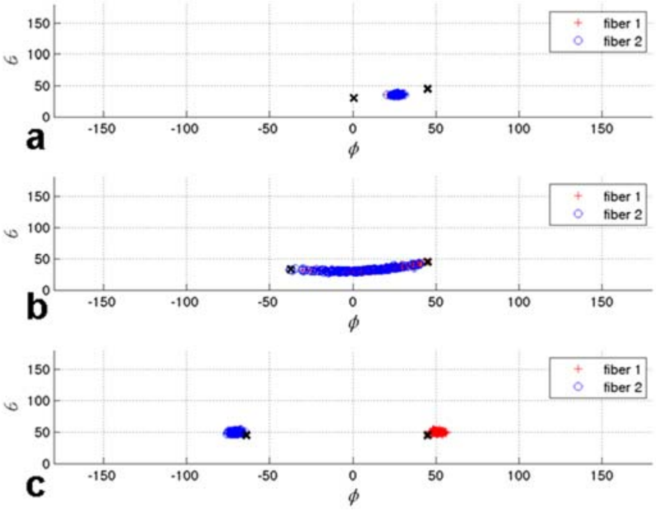

Figure 4.12. Estimates of fiber direction using TIKH-negFOD and 4th order expansion are plotted for each separation angle: 30 degrees (a), 50 degrees (b) and 70 degrees (c). Results are shown for 200 trials for fiber 1 in red (+) and fiber 2 in blue (o) with the true fiber directions (×). Angles are in degrees.

However, the true fiber directions cannot be distinguished even at 50 degrees (Figure 4.12b), and the center of each distribution seems to be biased at 70 degrees (Figure 4.12c). These characteristics (small dispersion and bias around the true fiber direction) are common to all the other regularization results as well as LS result (not shown) when 4th order is used as can be seen from the FOD function in Figure 4.4.

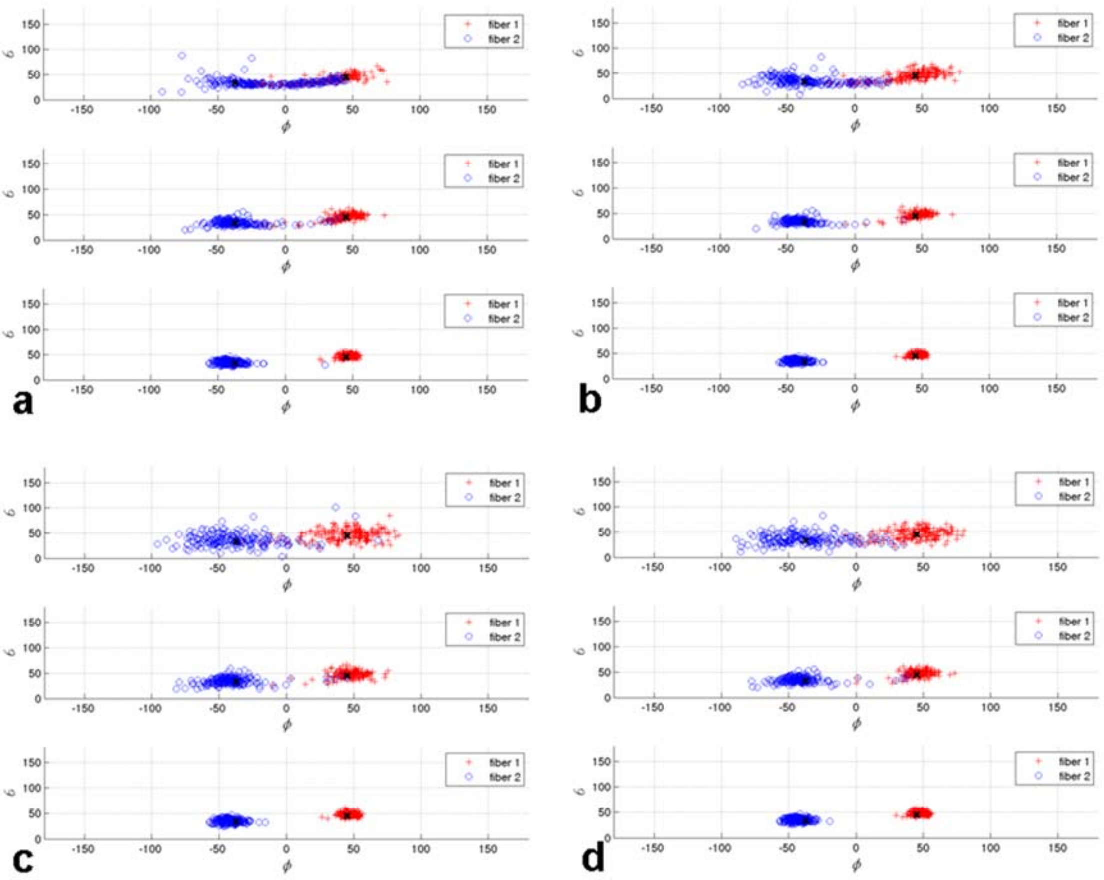

Figure 4.13. Estimates of fiber direction using TIKH (a), TIKH-negFOD (b), DSVD (c) and DSVD-negFOD (d) are plotted for each *b*-value: 1000 (top), 2000 (middle) and 3000 (bottom) s/mm^2. Results for 200 trials are shown for fiber 1 in red (+) and fiber 2 in blue (o) with the true fiber directions in black (×) on θ (vertical) and ϕ (horizontal) axes in degrees.

4.4.3.2. b-value

For 50 degrees separation angle, Figure 4.13 shows the estimates of fiber directions with *b*-values of 1000 (top), 2000 (middle) and 3000 (bottom) s/mm^2 in each subplot with two fibers, SNR = 60, 6th order expansion and 92 diffusion encoding directions for TIKH (a), TIKH-negFOD (b), DSVD (c) and DSVD-negFOD (d). As *b*-value increases from 1000 to 3000 s/mm^2, the distribution of estimates for each fiber direction becomes less dispersed and more concentrated about the true fiber directions as seen in Figure 4.6.

4.4.3.3. Diffusion encoding directions

Figure 4.14 represents fiber orientation estimates for different numbers of diffusion encoding directions and SNR = 60, 6th order expansion, *b*-value = 2000 s/mm^2 and 50 degrees separation angle. With increasing number of diffusion encoding directions (from top to bottom in each subplot), the estimates for each fiber are more concentrated around the true fiber directions for all the regularization methods, as seen in Figure 4.8. There is no significant difference between TIKH (a and b) and DSVD (c and d), and similar estimates are observed for TSVD and LS results (not shown). For 4th order expansion, the estimates of fiber directions are dispersed widely and the two fibers cannot be distinguished in this case (not shown).

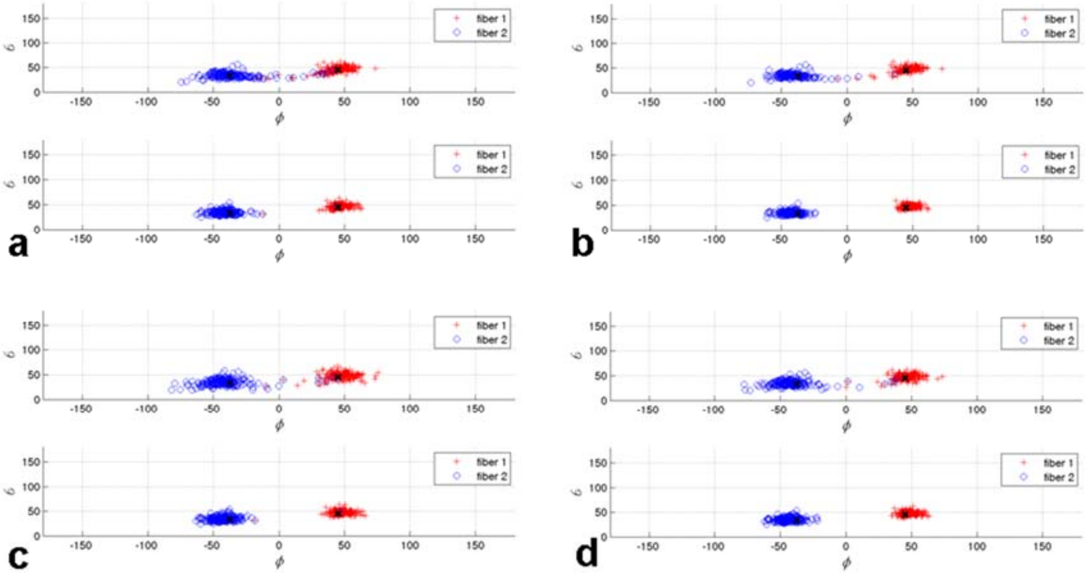

Figure 4.14. Estimates of fiber direction using TIKH (a), TIKH-negFOD (b), DSVD (c) and DSVD-negFOD (d) are plotted for 92 (top) and 162 (bottom) diffusion encoding directions. Results for 200 trials are shown for fiber 1 in red (+) and fiber 2 in blue (o) with the true fiber directions in black (×) on θ (vertical) and ϕ (horizontal) axes in degrees.

4.4.3.4. Number of fibers

Figure 4.15 represents the estimated fiber orientation for two (top) and three (bottom) fibers within a voxel with SNR = 60, 6th order expansion, 92 directions, *b*-value = 2000 s/mm^2 and 50 degrees of separation angle (fiber 1-fiber 2 and fiber 1-fiber 3 for three fiber case). The two fiber estimations are crowded around the true fiber directions with moderate dispersion regardless of the use of constraint as shown in Figure 4.15. For three fibers, estimates for each of the fibers are relatively more concentrated around the true fiber directions than those for two fiber case.

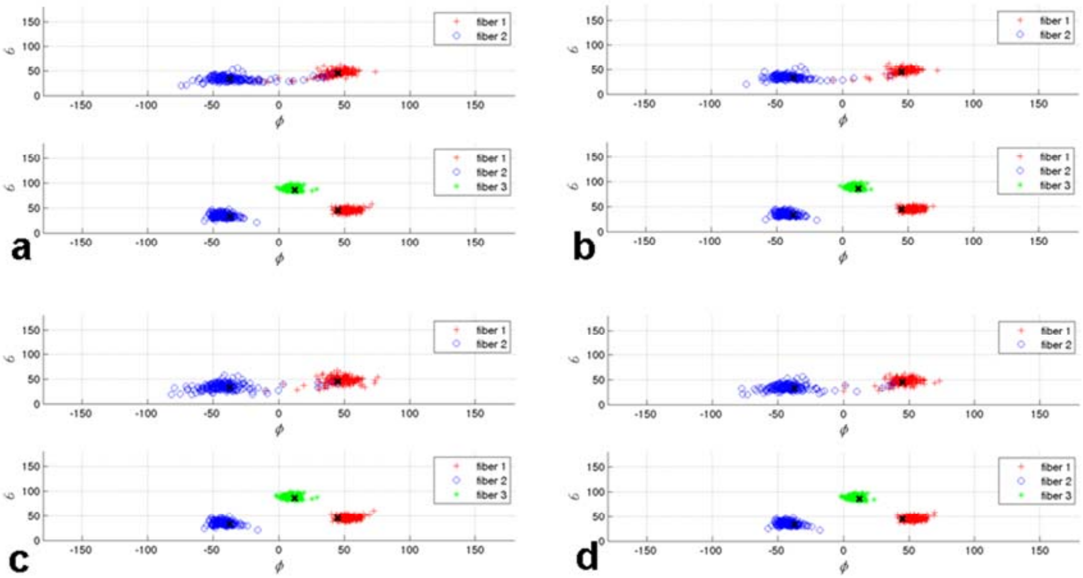

Figure 4.15. Estimates of fiber direction using TIKH (a), TIKH-negFOD (b), DSVD (c) and DSVD-negFOD (d) are plotted for the number of fibers: 2 (top) and 3 (bottom). Results are shown for 200 trials for fiber 1 in red (+), fiber 2 in blue (o) and fiber 3 in green (*) with the true fiber directions in black (×) on θ (vertical) and ϕ (horizontal) axes in degrees.

However, the center of estimates for fiber 1 and fiber 2 appears to be biased from the true fiber direction. Simulations using TSVD and LS show similar results (not shown).

4.4.4. Effect of SNR on FOD and fiber direction

Figure 4.16 shows a comparison between TIKH and DSVD with negFOD results for both the FOD and fiber direction estimates over varying SNR (30, 60 and 90) with 6th order expansion, 92 directions, *b*-value = 2000 s/mm^2, two fibers and 50 degrees of separation angle. TIKH shows less noise at the origin of the FOD and smaller dispersion in the estimates of fiber directions than DSVD at SNR of 30. However, TIKH and DSVD show similar FOD and estimations of fiber directions over the SNR of 60.

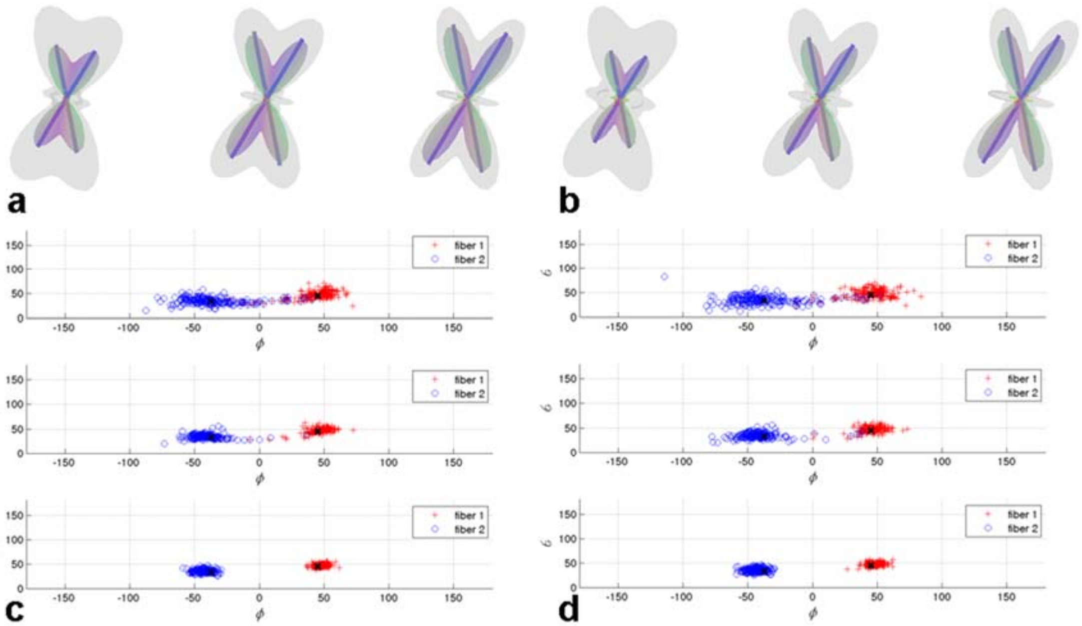

Figure 4.16. The FOD functions for the mean (mixed color) and the mean plus twice the standard deviation (gray) are presented with estimates of fiber direction using TIKH-negFOD (a and c) and DSVD-negFOD (b and d) for the SNR of 30 (left (a,b) and top (c,d), 60 (middle in a-d) and 90 (right (a,b) and bottom (c,d).

4.5. Discussion and Conclusion

The spherical deconvolution method has been widely used to represent FOD functions within a voxel, but the accurate estimation of the function is very difficult as most deconvolution problems are ill-posed and hence susceptible to image noise. In this simulation study, we tested various classes of regularization methods, i.e., TIKH, TSVD and DSVD with and without regularization constraint using objective determinations of the regularization parameter for improved estimates of the FOD and the true fiber directions.

Figures 4.1 and 4.2 show a comparison of the regularization methods as well as various constraints and parameter determination methods. Using sqLap and sqGrad with GCV and L-curve usually generates much lower angular resolution in the FOD than using negFOD or no constraint, effectively smearing all fiber peaks. Because the constraints are related to the curvature or gradient of the FOD function, the regularization parameter tends to decrease the curvature or gradient of the function resulting in an FOD with much lower angular resolution. When the regularization is done without any side constraint and with negative FOD constraint, the regularization parameter from L-curve is much larger than that from GCV generating wider peaks for each fiber bundle relative to those using GCV. However, this may suppress any possible small fibers. Therefore, considering the primary purpose of this study, GCV and negFOD are used as the parameter determination method and constraint as explained previously.

Figure 4.3 shows mean and the mean plus twice the standard deviation for the estimation of the FOD function. For TIKH (Figure 4.3a) and TSVD (Figure 4.3b) results, improved angular resolution and reduced standard deviation of the FOD are observed with use of negFOD as shown in Figure 4.3d and e, respectively. Figure 4.3c shows that the DSVD result provides no significant improvement in angular resolution compared to when the constraint is used (Figure 4.3f). But there is noticeable reduction of standard deviation in small lobes around the origin of the FOD function with use of the constraint. Comparing both cases (with and without constraint) DSVD generates relatively robust FODs compared to the others. At lower expansion order (order 4), FODs usually have smaller errors than those at 6th order. But they also appear to have much lower angular resolution with no noticeable fiber bundles along the true direction, even at 50 degrees fiber separation. This shows that we need higher expansion order to separate the fiber bundles crossing at smaller angles (e.g., 6th order for 50 degrees separation, at least) at the expense of a larger contribution of noise in the FOD as shown in Figures 4.3-4.5. Estimations of the true fiber directions based on the separation angle are shown using LS (Figure 4.10) and TIKH and DSVD (Figures 4.11). As expected, increasing separation angle represents better definition of each fiber direction regardless of the use of constraint. At 4th order, estimations seem to be robust as they are less dispersed (Figure 4.12), but they have large errors (Figure 4.12a-b) or biased cluster centers (Figure 4.12c). Therefore the use of higher expansion order is preferable for identification of multiple fibers with unknown separation angles (possibly a small angle). However, when we analyze the voxels with fibers of known (large) separation angle, e.g., corpus callosum and cingulum bundle crossing at about 90 degrees to each other, using the 4th order may be enough.

Increasing *b*-value improves the FOD as shown in Figure 4.6, in general. Also using the constraint in regularization increases angular resolution, especially at lower *b*-value (1000 s/mm^2). Using lower expansion order (4th) is not helpful resolving multiple fiber structures even at *b*-value of 3000 s/mm^2 (Figure 4.7c). Using larger *b*-value also has better definition for estimating multiple fiber directions as in Figure 4.13. Other simulations show similar results for fiber directions with varying *b*-values including the LS result (now shown). Therefore it is helpful using intermediate (2000 s/mm^2) to relatively large (3000 s/mm^2) *b*-value with regularization (TIKH or DSVD with or without constraint). However, at relatively low *b*-value (e.g., 1000 s/mm^2) we suggest that using regularization with constraint will better estimate the FOD and fiber directions.

The use of larger (more than 92) numbers of diffusion encoding directions seems to be helpful for improving angular resolution for TIKH (Figure 4.8a, d) and TSVD (Figure 4.8b and e) results, but it appears that there is negligible improvement for DSVD.

Figure 4.14 shows that it reduces scatters in fiber directional estimates. However, increasing the number of directions requires the expense of imaging time, e.g., increasing from 92 to 162 requires 1.76 times more imaging time and hence possibly becomes more susceptible to motion artifact. Therefore we suggest that using larger *b*-value (with the same or moderate increase of echo time) will be more beneficial than using larger angular sampling.

Most of the regularization results generate similar FOD functions for three fiber FODs regardless of the use of constraint (Figure 4.9) except for TSVD (Figure 4.9b). On the contrary to the two fiber directional estimates with moderate dispersion (tops in Figure 4.15), the estimates for three fibers appear to be less dispersed but the center of the estimates is significantly biased (bottoms in Figure 4.15). Also, three fiber FODs show much larger erroneous fiber peaks around their origin (Figure 4.9) than two fiber FODs, and those peaks can easily be mistaken for true fibers. When this is the case in specific imaging studies, acquiring high SNR may be the most important factor to reduce the magnitude of erroneous fiber bundles.

The effect of SNR on the estimates of the FOD and fiber directions is shown in Figure 4.16 for both TIKH and DSVD with negFOD. At SNR of 30, TIKH shows less noise and dispersion on the FOD and estimates of fiber direction than DSVD. However, they show similar FOD and fiber directional estimates over the SNR of 60.

In this study we investigated various methods for the robust and reliable estimation of the FOD function which is critical for comparison across groups for fiber tractography. With regularization, more reliable FODs can be calculated with reduced standard deviation for all the cases of imaging and simulation parameters tested here, and hence more accurate fiber tracking may be expected. The use of higher expansion order and *b*-value are recommended for better estimation of the FOD and fiber directions, considering the minimum resolvable fiber separation angle, SNR and imaging time in the experiment. The use of constraint has a small to moderate effect over the regularization results (TIKH and DSVD), but it does not require any additional expense, such as imaging time, and can be performed in post-processing. Therefore, it is recommended to use constraint with regularization for estimating FODs and fiber directions. TSVD shows large variations, especially without constraint, in FOD and fiber direction (not shown) over various parameters tested in this study. TIKH and DSVD outperform TSVD in both FOD reproducibility and estimates of fiber direction. Considering the simulation results with imaging parameters, TIKH may be more preferable at relatively low SNR, but both of the TIKH and DSVD generate comparable results with negFOD for the estimates of the FOD and fiber directions as shown through this study.

CHAPTER Ⅴ

MEASUREMENT OF INTRINSIC FIBER DIFFUSION PROPERTIES USING SPHERICAL DECONVOLUTION OF HARD IMAGING DATA

5.1. Overview

Many approaches using the HARD encoding scheme have been successful in delineating complex fiber architecture within a single voxel of brain white matter. However, they are unable to provide intrinsic diffusion properties of any of the included fibers, and the estimation of those properties within a single voxel has not been studied rigorously. In this study we evaluate a method to estimate fiber-specific diffusion properties within a voxel using FORECAST, a spherical deconvolution method. The simulation results show that our method can estimate radial diffusivity and volume fraction for individual fibers at modest to high SNR level. In *in vivo* studies, individual fiber FODs can be separated and plotted based on an estimate of radial diffusivity and volume fraction for each fiber bundle. The diffusivity for each fiber in single- and crossing-fiber regions is compared to demonstrate that individual fibers' diffusion properties are preserved in the crossing region. However, diffusion properties may be variable between fiber bundles. These studies lay a groundwork for more accurate measurements of white matter fiber properties on a subvoxel level.

5.2. Introduction

Diffusion tensor MR imaging (DT-MRI) has been successful in detecting subtle changes in water molecular diffusion using a series of diffusion weighted images applied in at least six non-collinear directions [19,20,22,26,58]. Although it has been useful in delineating white matter tissue structure, the tensor model is based on the assumption of Gaussian diffusion which is inappropriate within many regions of complex fiber structure [19,56,65,66]. The presence of multiple fiber directions within a single imaging voxel, i.e., a partial volume effect, cannot be characterized accurately by a single tensor because a tensor possesses only a single orientational maximum (shared by opposing directions), i.e., a tensor describes single fiber diffusion [28,56,57,59,60,64,71]. This situation is common for most DT-MRI studies using EPI techniques in which relatively large voxels are used [59]. Alternative models were suggested using multi-component analysis [81-85], such as two (fast and slow) diffusion compartments, and two-tensor models using six [86,87,115] or more [64] non-collinear diffusion gradient directions. However those methods are limited to two components and cannot accurately characterize diffusion with more than two fiber directions, for example.

Many approaches using high angular resolution diffusion (HARD) encoding schemes, e.g., diffusion spectrum imaging (DSI) [66,68] and q-ball imaging (QBI) [69] etc., can identify multiple fiber directions. However, they do not provide any information about the intrinsic diffusion properties of any of the fibers other than a diffusion orientation distribution function (ODF), and the estimates of the properties for each fiber within a voxel have not been studied extensively. Tournier et al. [73] suggested a method that is able to estimate directly the distribution of fiber orientations within a voxel from the HARDI signal using spherical deconvolution (SD) with the following assumptions: there is negligible exchange between distinct fiber bundles and the diffusion characteristics of all fibers in the brain are identical except for fiber orientation. Though there are no extensive studies about the latter assumption, the Tournier study showed the possibility of estimating the volume fraction of each of a known number of fiber compartments, e.g., two fiber compartments. In this method, the response function was found directly from data by measuring the diffusion weighted (DW) signal profile in regions likely to contain a single and coherently oriented fiber population, i.e., regions with high diffusion anisotropy. Another SD method was suggested by Anderson [74,75]. This method, named Fiber ORientation Estimated using Continuous Axially Symmetric

Tensors (FORECAST), provides an analytic expression for the signal response function using the assumptions that each fiber bundle has axially symmetric diffusion and common mean and radial diffusivity within a voxel. This method successfully demonstrated that the fiber orientation distribution (FOD) measurement was possible at relatively low *b*-value (1480 s/mm^2) and diffusion weighting directions (92 directions) with higher angular resolution for the FOD than other methods [74].

Provided an FOD with higher resolution and an analytic kernel function, we may estimate intrinsic diffusion properties for individual fiber bundles within each voxel in brain white matter. In this study we propose and evaluate a method to estimate the intrinsic diffusion properties, i.e., radial diffusivity and volume fraction, for individual fibers within a voxel using the FORECAST model with HARDI.

5.3. Methods

5.3.1. FORECAST for multiple fibers and b-values

FORECAST uses a spherical harmonic expansion of the DW signal, $S(\theta,\phi)$, and FOD function, $P(\theta,\phi)$, as in (5.1) and (5.2),

$$S(\theta,\phi) = \sum_{l=0}^{\infty} \sum_{m=-l}^{l} s_{lm} Y_{lm}(\theta,\phi), \tag{5.1}$$

$$P(\theta,\phi) = \sum_{l=0}^{\infty} \sum_{m=-l}^{l} p_{lm} Y_{lm}(\theta,\phi) \,. \tag{5.2}$$

Spherical harmonic coefficients for an arbitrary function $f(\theta,\phi)$ can be obtained using (5.3),

$$f_{lm} = \int_0^{2\pi} \int_0^{\pi} f(\theta,\phi) Y_{lm}^{*}(\theta,\phi) \sin(\theta) d\theta d\phi \,. \tag{5.3}$$

The relationship between the DW signal and FOD in FORECAST can be expressed similarly as SD methods as in (5.4)-(5.6)

$$s_{lm} = S_0 \cdot c_l \cdot p_{lm} \,, \tag{5.4}$$

where

$$c_l \equiv \frac{4\pi}{2l+1} e^{-b\lambda_{\perp}} A_l \,, \tag{5.5}$$

and

$$A_l = \frac{2l+1}{2} \int_{-1}^{1} e^{-3b(\lambda_{avg}-\lambda_{\perp})\cos^2\alpha} P_l(\cos\alpha) d(\cos\alpha) \,, \tag{5.6}$$

here S_0 is the non-DW signal, *b* is the diffusion weighting *b*-value, λ_{avg} is the mean diffusivity, $\lambda_{\perp}$ is the radial diffusivity, P_l is the Legendre polynomial of order *l* and α is the measurement angle relative to a fiber axis [74]. Taking advantage of the analytical response function from this model, (5.4) can be extended to the case of multiple fibers to provide estimates of radial diffusivity and volume fraction of each fiber. We can expand (5.4) to a system with n_b *b*-values and n_f fibers as shown in Appendix B. In this preliminary study, we primarily focused on two fiber ($n_f = 2$) diffusion as below,

$$\frac{4\pi}{S_0}\begin{bmatrix} S_{avg}(b_1) \\ S_{avg}(b_2) \\ \vdots \\ S_{avg}(b_{nb}) \end{bmatrix} = \begin{bmatrix} c_0(b_1,\lambda_{\perp 1}) & c_0(b_1,\lambda_{\perp 2}) \\ c_0(b_2,\lambda_{\perp 1}) & c_0(b_2,\lambda_{\perp 2}) \\ \vdots & \vdots \\ c_0(b_{nb},\lambda_{\perp 1}) & c_0(b_{nb},\lambda_{\perp 2}) \end{bmatrix} \cdot \begin{bmatrix} f_1 & 1-f_1 \end{bmatrix}^{\mathrm{T}}, \tag{5.7}$$

here S_{avg} is the mean DW signal with $s_{00} = \sqrt{4\pi}S_{avg}$, b_i is the i^{th} b-value and f_j and $\lambda_{\perp j}$ are the j^{th} fiber volume fraction and radial diffusivity, respectively, using $p_{00j} = 1/\sqrt{4\pi}\, f_j$. Since we have interest in finding the radial diffusivities of $\lambda_{\perp 1}$, $\lambda_{\perp 2}$ and volume fraction (f_1) with $\lambda_{\perp 1} < \lambda_{\perp 2}$ by assumption, we try to search over the 3D grid space of ($\lambda_{\perp 1}, \lambda_{\perp 2}$, f_1) using the following cost function,

$$\sum_{i=1}^{n_b}\left[\frac{1}{S_0}\left(S_{avg}(b_i) - S^{\dagger}_{avg}(b_i)\right)\right]^2, \tag{5.8}$$

which is the sum of the squared error between the measured and estimated ($S^{\dagger}_{avg}$, using (5.7)) mean DW signal. The search range for each of the radial diffusivity is determined using the kernel function from a single fiber estimate ($\lambda_{\perp s}$) and λ_{avg} as in (5.9) and (5.10),

$$0 \le \lambda_{\perp 1} < \lambda_{\perp s}, \tag{5.9}$$

$$\lambda_{\perp s} < \lambda_{\perp 2} \le \lambda_{avg}, \tag{5.10}$$

as shown in Appendix C. With the assumptions of axially symmetric diffusion and shared mean diffusivity between fibers, the parallel diffusivity ($\lambda_{\|}$) can be represented simply as

$$\lambda_{\|j} = 3\lambda_{avg} - 2\lambda_{\perp j},\ j=1, \ldots, n_f.$$

5.3.2. Simulation

We simulated the DW signal from a voxel containing two fibers using (5.1) and (5.4) with known fiber orientation, $\lambda_{\perp}$ and f for each fiber using a typical λ_{avg} for brain white matter [58] with varying SNR level equal to 50, 80, 110 and 140. Trial values of $\lambda_{\perp j}/\lambda_{avg}$ and f_j were used to simulate the signal at each point in a 3D grid in which the variables ranged between 0 to 1. The estimated values of $\lambda_{\perp j}/\lambda_{avg}$ and f_1 (for the two fiber case, $f_2 = 1 - f_1$, so only one volume fraction enters the search) are those that produce the lowest error in (5.8). The histogram of search errors of each of the $\lambda_{\perp j}$ and f_1 was plotted for each SNR level to investigate the minimum SNR required for robust estimation. Because the non-DW signal (S_0) was critical in the search as shown in (5.8), the simulations were performed assuming known S_0.

5.3.3. Data acquisition and processing

We used a Philips Achieva 3 Tesla scanner with *b*-values of 1500 and 3000 s/mm^2, TE 65 ms and TR 3000 ms, 3 × 3 × 3 mm^3 voxel size, 96 × 96 image matrix with 13 axial slices and 92 diffusion gradient directions defined by the 3rd order icosahedral tessellation of the unit sphere. In total, seven acquisitions were performed and each acquisition was done within 10 minutes. Every data set was registered using a 3D affine transform, and then averaged to increase the signal to noise ratio (SNR). We selected ROIs on the brain white matter known to include crossing fibers, i.e., the cingulum and corpus callosum fibers. Individual fiber bundle's radial diffusivity and volume fraction were estimated based on the two fiber model for each voxel in the ROI. The kernel function (5.5) is calculated for individual fibers using estimates of each $\lambda_{\perp}$. The fiber specific FOD was calculated using regularization [77], and each fiber's FOD was compared with the FOD from the single fiber solution (with single kernel function using $\lambda_{\perp s}$) and with the principal eigenvector from a single diffusion tensor model for each voxel. All the study protocols were approved by Vanderbilt University's institutional review board.

5.4. Results

Figure 5.1 shows the histogram of the simulation results for the SNR dependence of the search errors (5.8) for radial diffusivity of fiber 1, fiber 2 and volume fraction of fiber 1 with varying SNR of 50, 80, 110 and 140. In the simulation the search errors were significantly decreased between the SNR of 50 and 80 as shown in Figure 5.1a-b. However, it seems that there are no noticeable reductions of error over the SNR of 110 as shown in Figure 5.1c-d.

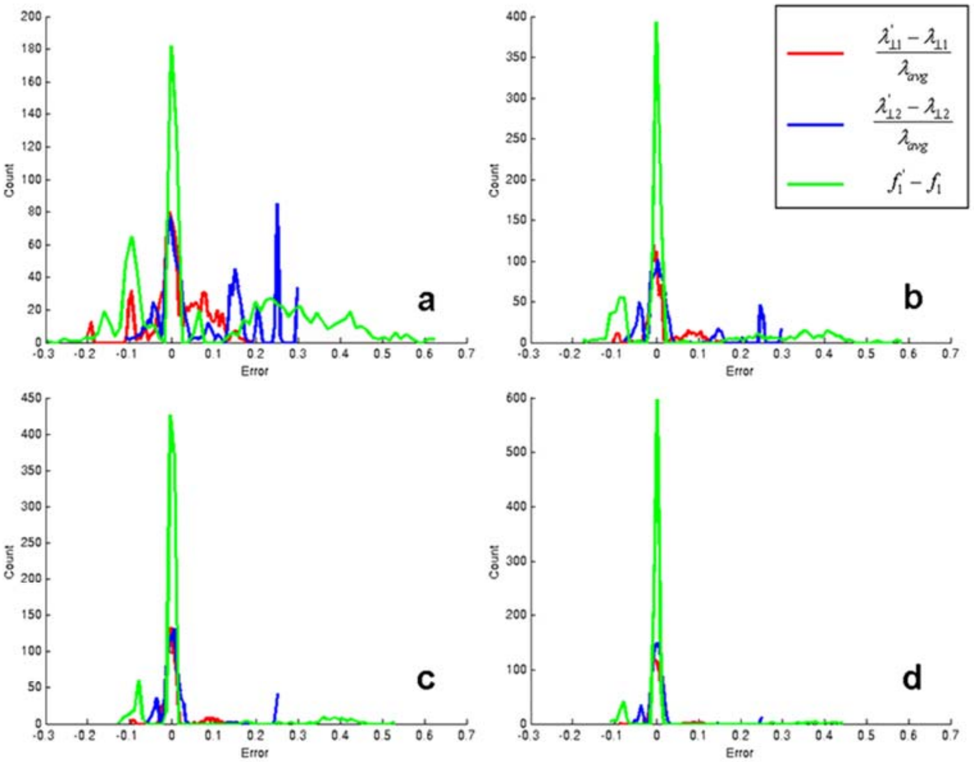

Figure 5.1. The histogram of search errors for the radial diffusivity of fiber 1 (red) and fiber 2 (blue) both normalized by mean diffusivity and volume fraction of fiber 1 (green) as shown in the legend on the upper right side of (b) for SNR of 50 (a), 80 (b), 110 (c) and 140 (d). Over the SNR of 80 the search errors are significantly decreased.

In Figure 5.2a, an ROI is drawn over an FA colormap which contains a mixture of two crossing fibers. The crossing fibers can be seen clearly (on the right in Figure 5.2a) in the FOD using a single kernel function (response function from single fiber estimation) for each voxel. The principal eigenvector (blue line) from the diffusion tensor model is also shown in Figure 5.2a-b.

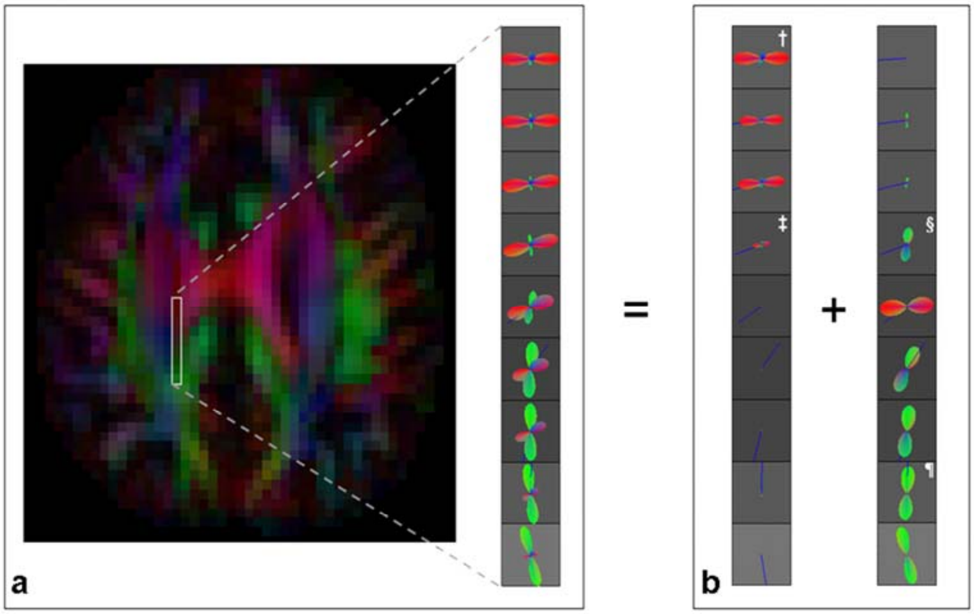

Figure 5.2. An ROI is drawn over an FA colormap on the left in (a). FODs are represented using a single fiber kernel function with the tensor principal eigenvector on the right in (a). The FODs in (a) are separated into individual fibers with smaller (left side in (b)) and larger (right side in (b)) radial diffusivities using estimated individual kernel functions. FODs for the single and crossing fibers are shown in (b) for a voxel marked † (single fiber 1), ¶ (single fiber 2), ‡ (crossing fiber 1) and § (crossing fiber 2). The radial diffusivities are very similar in the case of single and crossing fibers (†:0.5, ‡:0.45 for fiber 1 and ¶:0.62, §: 0.63 for fiber 2 in 10^{-5} cm^2/s unit). Each FOD is normalized to unit sum and then weighted by the corresponding volume fraction.

The orientation of the principal eigenvector is along one fiber (top four and bottom three voxels) or between fibers (5th and 6th voxels from the top). Figure 5.2b shows the FOD for the individual fibers: the fiber with smaller $\lambda_{\perp}$ (on the left) and with larger $\lambda_{\perp}$ (on the right) weighted by the estimation of each fiber's volume fraction. In comparison with the FA colormap in Figure 5.2a and each fiber's FOD in Figure 5.2b, the representation of each individual FOD weighted by its volume fraction seems to match the known anatomical fiber structures. To demonstrate that the estimates of individual fiber diffusivity are accurate in the crossing regions, the radial diffusivities were compared inside and outside the crossing region along the same fiber. An assumption in this test is that radial diffusivity varies slowly with position along a fiber. In Figure 5.2b, the FODs marked as † and ¶ represent the single fibers designated fiber 1 and fiber 2, respectively, since the volume fraction of the other fiber in those voxels appears very small. The FODs marked ‡ and § represent the two crossing fibers, but in this case they appear to have comparable volume fractions as both of the FODs can be clearly seen with similar size. Because we expect a fiber to have nearly uniform radial diffusivity (over small distances at least), regardless of partial volume averaging, we compared the diffusivity of each fiber between voxels with single and crossing fibers. For fiber 1, the radial diffusivities for the single fiber (marked †) and crossing fiber (marked ‡) are 0.5 and 0.45, respectively, and for the fiber 2, they are 0.62 (marked ¶) and 0.63 (marked §) (all in units of 10^{-5} cm^2/s). Those radial diffusivities were well matched between single and crossing fibers for each case. Figure 5.3 shows another ROI at the crossing of the cingulum and corpus callosum fiber bundles. Although there is a small crossing fiber bundle appearing with fiber 2 in the voxel marked ¶, most of the volume of the voxel is taken up by the single fiber 2. The radial diffusivities for the single and crossing fibers are 0.62 (†) and 0.55 (‡) for fiber 1, and 0.62 (¶) and 0.65 (§) for fiber 2. Note that the near equality of radial diffusivity of the two fibers makes the designations 'fiber 1' and 'fiber 2' somewhat arbitrary.

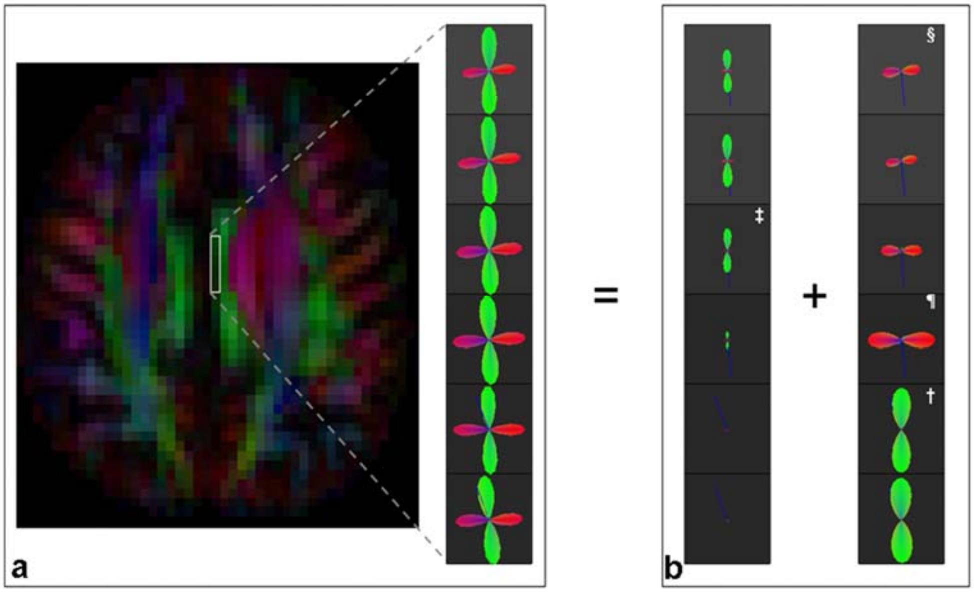

Figure 5.3. An ROI is drawn over an FA colormap on the left in (a). FODs are represented using a single fiber kernel function with the principal eigenvector on the right in (a). The FODs in (a) are separated into individual fibers with smaller (left side in (b)) and larger (right side in (b)) radial diffusivities using estimated individual kernel functions. FODs for the single and crossing fibers are shown in (b) for a voxel marked † (single fiber 1), ¶ (single fiber 2), ‡ (crossing fiber 1) and § (crossing fiber 2). The radial diffusivities are very similar in the case of the single and crossing fibers (†:0.62, ‡:0.55 for fiber 1 and ¶:0.62, §: 0.65 for fiber 2 in 10^{-5} cm^2/s unit). Each FOD is normalized to unit sum and then weighted by the corresponding volume fraction.

From the simulation (Figure 5.1) and *in vivo* results shown in Figures 5.2 and 5.3, our model can find radial diffusivities and volume fractions for crossing fibers with the assumptions of axially symmetric diffusion, negligible water exchange, uniform T2 relaxation time and mean diffusivity between fiber bundles and measured S_0 with reasonably good accuracy.

5.5. Discussion and Conclusion

In this study we developed a method for finding fiber-specific diffusion information such as radial diffusivity and volume fraction within a single voxel assuming axially symmetric diffusion, shared mean diffusivity and slow or no exchange between fibers considering the typical diffusion time scale. These assumptions are reasonable in our experiments and have been used in other HARD imaging studies [64,73]. In addition to these assumptions, Tournier et al. [73] assumed that all the fiber populations have the same diffusion properties except orientations, measuring DW signal attenuation from a single fiber population to estimate a global response function. In our study, however, we omitted the identical diffusivity assumption by estimating each fiber bundle's radial diffusivity to estimate fiber-specific response functions.

The simulation results showed that the minimum requirement of SNR is about 80 for the robust estimation of radial diffusivities and volume fraction. In our experiment, the SNR for each acquisition measured in non-DW data was 40 to 50 and we averaged seven acquisitions to meet the minimum SNR requirement. We selected different ROIs based on known crossing fiber structure with easily separable angles (about 90 degree), i.e., the corpus callosum and cingulum fiber bundles, using moderate angular sampling (92 directions in our experiment). Figure 5.2 and 5.3 show FODs calculated using a single kernel (same radial diffusivity for all fibers) and multiple kernels (individual radial diffusivity for each fiber) with the estimated radial diffusivity and volume fraction for each fiber within each voxel in the ROI. To assure that the diffusion coefficient of a fiber is preserved in crossing regions, we compared the radial diffusivity of each fiber bundle in the single-fiber and crossing regions. In Figure 5.2, the diffusivities between the single- and crossing-fiber voxels are very close, and there is a relatively large difference between fibers. In Figure 5.3, the diffusivity is also quite similar between single and crossing fibers; however it is even closer between single fibers. This case suggests that there may be variations of diffusivity along as well as between fiber bundles. Those characteristics may be validated by segmenting individual fiber bundles and then comparing the radial diffusivity along and between those bundles.

The orientation of the principal eigenvector (blue stick in each voxel in Figures

5.2 and 5.3) from a single diffusion tensor model is closer to the orientation of the fiber bundle whose volume fraction or anisotropy (in the case of comparable volume fraction) is larger than that of the other fiber. In this study, the direction of the principal eigenvector is closer to the right-left direction (top four voxels in red in Figure 5.2b, where the volume fraction of fiber 1 is larger than the other fiber). Also the directions are closer along the anterior-posterior direction (bottom three voxels in Figure 5.2b and two voxels in Figure 5.3b where the volume fractions of the anterior-posterior fibers are much larger than the other fiber bundle). In Figure 5.3b, the top three voxels seem to have comparable volume fractions between fibers, but the principal eigenvectors are aligned in the anterior-posterior direction which is along fiber 1 (in green) whose anisotropy is larger than that of the fiber 2. This observation supports the need of ODF or FOD construction, rather than a single tensor, for reliable fiber tracking through a crossing region.

High angular resolution diffusion imaging has been successful in providing ODF or FOD estimates for the identification of multiple fiber bundles within a single voxel. Though the representations of diffusion orientation along fibers, e.g., the ODF or FOD from QBI, DSI or FORECAST, are not identical, they produce quite similar fiber orientations [74]. Recently these methods have been successfully used as a basis for *in* *vivo* fiber tractography, for example with DSI [116], q-ball [117] and SD [118]. Therefore, our method may be extended to estimate diffusion properties for voxels with more than two fiber bundles.

Although our method depends on the identification of the number of fiber bundles within a voxel, this has not been rigorously studied yet. Hess et al. [72] showed simulation results quantifying the power spectrum of each of the even harmonic orders. Frank [57] used group theory to determine the sufficient spherical harmonic order for representing multiple fibers. In both studies, the maximum order of 4 seemed enough for multiple fibers, but the need for higher order also depends on the separation angle between the fibers with more angular sampling and larger *b*-value required for small angles as described in [57].

With the use of higher order or larger *b*-value, however, the effect of noise increases, and may result in spurious peaks in the FOD or ODF. Recently, low-pass filtering [73], minimum entropy [76] and regularization by minimizing the magnitude of negative peaks [77] have been suggested for more reliable estimation of the FOD. But those methods require *a priori* information about the filter factors [73] and/or regularization parameter [77], or a nonlinear optimization [76] which may take relatively long calculation times. Sakaie et al. [79] recently presented the combined use of the generalized cross validation (GCV) with damped generalized singular value decomposition (DGSVD) for the objective determination of the regularization parameter and the robust estimation of the FOD without *a priori* information or user interaction for the determination of the parameter. With the use of these methods a more reliable identification of multiple fiber bundles may be provided even with higher expansion order to distinguish fibers whose angular separation is relatively small. In this case, more accurate estimations of diffusion properties can be expected.

CHAPTER Ⅵ

ULTRA HIGH FIELD DIFFUSION WEIGHTED MR IMAGING

6.1. Overview

Recently ultra high field *in vivo* data have been used to demonstrate DTI and q-Ball imaging methods for improved visualization of white matter anatomy with parallel imaging and higher order shimming. However, increased B0 inhomogeneity at high field, due to magnetic susceptibility variations in the head, complicates accurate analysis of diffusion weighted images by causing geometric image distortions. Up to this point, there have not been any studies demonstrating the feasibility of the field inhomogeneity correction at 7 Tesla using DTI or HARDI data acquired with the EPI sequence. In this study, the efficacy of the field inhomogeneity correction using a static field map is investigated with *in vivo* HARDI data acquired on a 7 Tesla human scanner. The spatial accuracy of the correction is assessed using normalized mutual information and visual inspection of the FA map and fiber orientation distribution functions for corresponding white matter structures. This study suggests that, after the inhomogeneity correction, more accurate delineation of white matter and corresponding fiber structures can be provided. These methods may be useful for constructing the atlases of human white matter and for accurate fiber tracking in the ultra high field imaging environment.

6.2. Introduction

Diffusion weighted MRI (DW-MRI) has been successfully used for studying human brain white matter based on water molecular diffusion [19-21,26,58]. Most studies have used diffusion tensor MRI (DT-MRI) or high angular resolution diffusion imaging (HARDI) to probe axonal connectivity using fiber tractography techniques [28,29,31,119,120] or detecting the presence of non-parallel fibers within a single voxel [60,65,66,73]. Conventional DW-MRI acquisition uses the EPI sequence to reduce the acquisition time. However, EPI is very sensitive to geometric distortions due to magnetic field inhomogeneity caused by magnetic susceptibility variations in the imaged object and eddy currents due to fast switching gradients. In the affected regions image intensity moves from its original position, causing an apparent stretching, compression or shearing of the image [97,121,122]. Several methods have been suggested for the correction of eddy current effects using an interleaved navigated sequence [122], twice-refocused gradient [123] or image registration [124]. Corrections of the field inhomogeneity effects have been suggested using forward and reverse phase encoding gradients [94] or a field map [97] for EPI data. The field map method has proved quite useful for the correction of fMRI and DW-MRI data [121,125,126]. However to the best knowledge of the authors, most of these studies have been done at moderate field strengths, i.e., much less than 7 Tesla, and no human DW-MRI studies, e.g., DT-MRI or HARDI, have been presented with inhomogeneity correction at ultra high fields such as 7 Tesla. Recently DT-MRI and q-ball imaging [69] studies have been published using 7 Tesla human scanners [89-92] with a transmit head coil and receive coil array with 8 channels [91,92] and 16 channels [90]. However, the effects of increased field inhomogeneity due to high field strength are not compensated in those studies. In this study, therefore, we present the feasibility of human DT-MRI and HARDI at 7 Tesla with corrections for image distortions due to field inhomogeneity and eddy currents using field map and image registration methods. Other sources of artifacts, such as B1 inhomogeneity or gradient nonlinearity effects, which generate intensity variations in an imaged object [98] or errors in interpreting diffusion information [100], may be reduced by using multi-channel excitation [99] or estimating the gradient coil tensor [100], and the effect of correcting these artifacts may be addressed in future studies.

6.3. Methods

6.3.1. Data acquisition

DW-MRI data were acquired on a 7 Tesla Philips Achieva whole body scanner (Philips Medical System, Cleveland, USA) with a 16 channel receive SENSE head coil. Diffusion weighted SE-EPI images were acquired using two protocols, 1). FOV 240×240 mm 96×96 image matrix, 2.75 mm slice thickness, TR/TE = 5500/72 ms, axial orientation and 2). FOV 192×192 mm, 80×80 image matrix, 2.4 mm slice thickness, TR/TE = 5500/69 ms in coronal orientation with SENSE factor 2 and 3, respectively. For both studies the diffusion weighting *b*-value of 0 and 2000 s/mm^2 with 32 diffusion weighting directions and one T2 weighted image were used. The acquisition was repeated for total of three scans for each protocol. In each experiment, field map images were acquired with the same FOV and image matrix using a 3D gradient echo sequence with echo spacing (ΔTE) of 1 ms and 0.5 ms for the scans with axial and coronal orientation, respectively. Also, the high resolution anatomical T1 weighted images were acquired with a 240×240 image matrix in corresponding orientation from each protocol to verify the locations of anatomical white matter structures for fractional anisotropy (FA) maps [26] and fiber orientation distribution (FOD) functions [74]. All the study protocols were approved by Vanderbilt University's institutional review board.

6.3.2. Data processing

Diffusion and T2 weighted images were coregistered using 3D affine transformation in order to correct distortion due to eddy currents. The geometric distortions due to field inhomogeneities were also corrected using a voxel displacement map calculated from the field map [97] for both the diffusion and T2 weighted human brain data. Then all the processed data sets were averaged to increase the SNR for all the *in vivo* data sets. To verify the effects of the correction, the spatial distribution of the voxel intensities was compared using the normalized mutual information (NMI) criterion [127] for images without and with the inhomogeneity correction after image coregistration. Also the anatomical positions of white matter structures and fiber bundles were compared by visually inspecting the FA and FOD maps by overlaying them on the high resolution T1 anatomical image for both the data without and with the correction. Before overlapping the two data sets, the size of the FA map (96×96 and 80×80 matrix) is linearly interpolated (to a 240×240 matrix) to match the size of the anatomical image. The FOD was calculated for each voxel using the FORECAST (Fiber ORientation Estimated using Continuous Axially Symmetric Tensors) model [74] with Tikhonov regularization penalizing negative values in the FOD [77] with an objective determination of regularization parameter [79,80] using 4th order spherical harmonic expansion.

6.4. Results

Figure 6.1 shows the $b = 0$ image, FA, and the FA overlaid on the T1 weighted image for one slice acquired with anterior fat shift direction (from bottom to top of the image) phase encoding in the axial orientation.

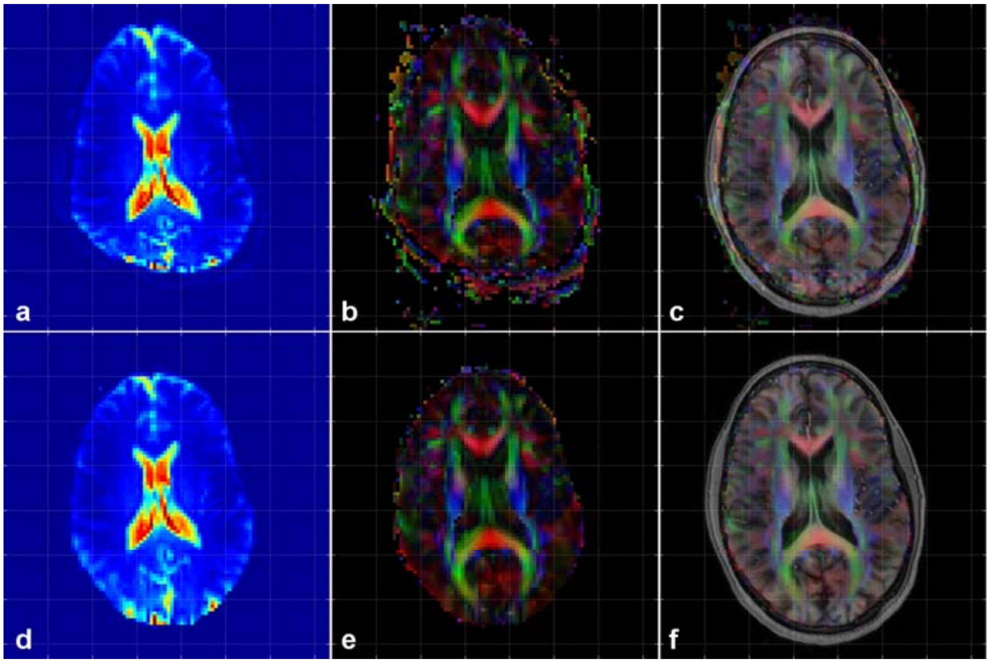

Figure 6.1. The original images with anterior phase encoding direction are shown for $b = 0$ (a), FA map (b) and FA map overlaid on the T1 weighted anatomical image (c). The correction images are shown for $b = 0$ (d), FA map (e) and FA map overlaid on the T1 weighted anatomical image (f). White dotted grid lines are shown on each image to verify

(Figure 6.1. Continued.)
the anatomical positions of white matter structures from FA map.

The images after the distortion correction are also shown. Figure 6.2 shows the $b = 0$ image, FA and the FA over T1 weighted image acquired with posterior fat shift direction (from top to bottom of the image) phase encoding in the same slice orientation of the same subject as in Figure 6.1. Each of the images after the distortion correction is shown in Figure 6.2d-f.

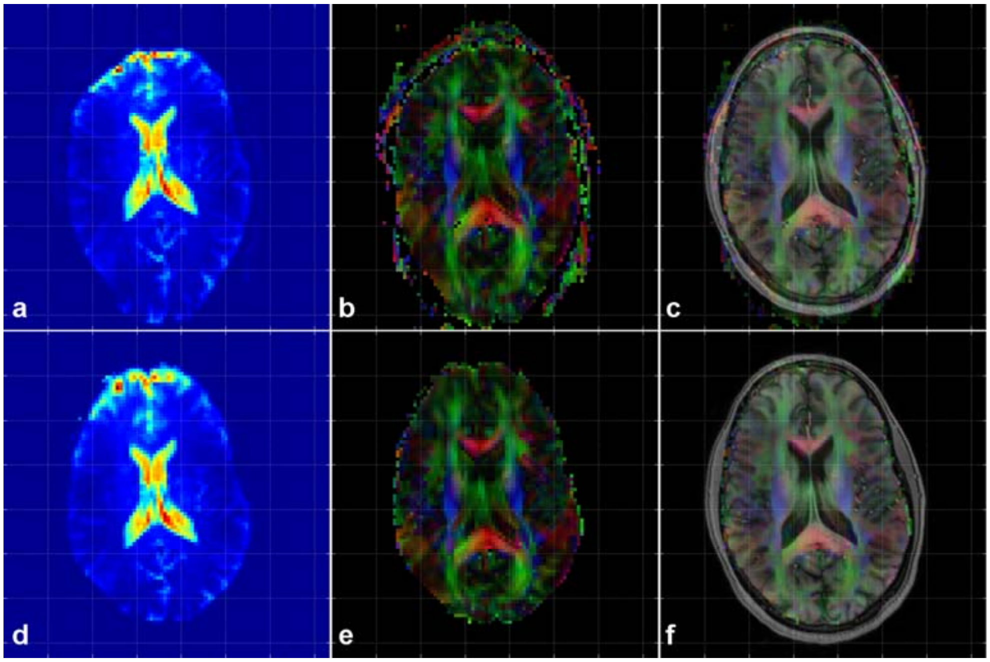

Figure 6.2. The original images with posterior phase encoding direction are shown for $b = 0$ (a), FA map (b) and FA map overlaid on the T1 weighted anatomical image (c). The correction images are shown for $b = 0$ (d), FA map (e) and FA map overlaid on the T1 weighted anatomical image (f). White dotted grid lines are shown on each image to verify the anatomical positions of white matter structures from FA map.

Figure 6.3 shows the magnified FA maps before and after the distortion correction taken from Figures 6.1and 6.2. Comparison of the corrected images shows that the outline of the brain is nearly the same, indicating that spatial distortions have largely been corrected.

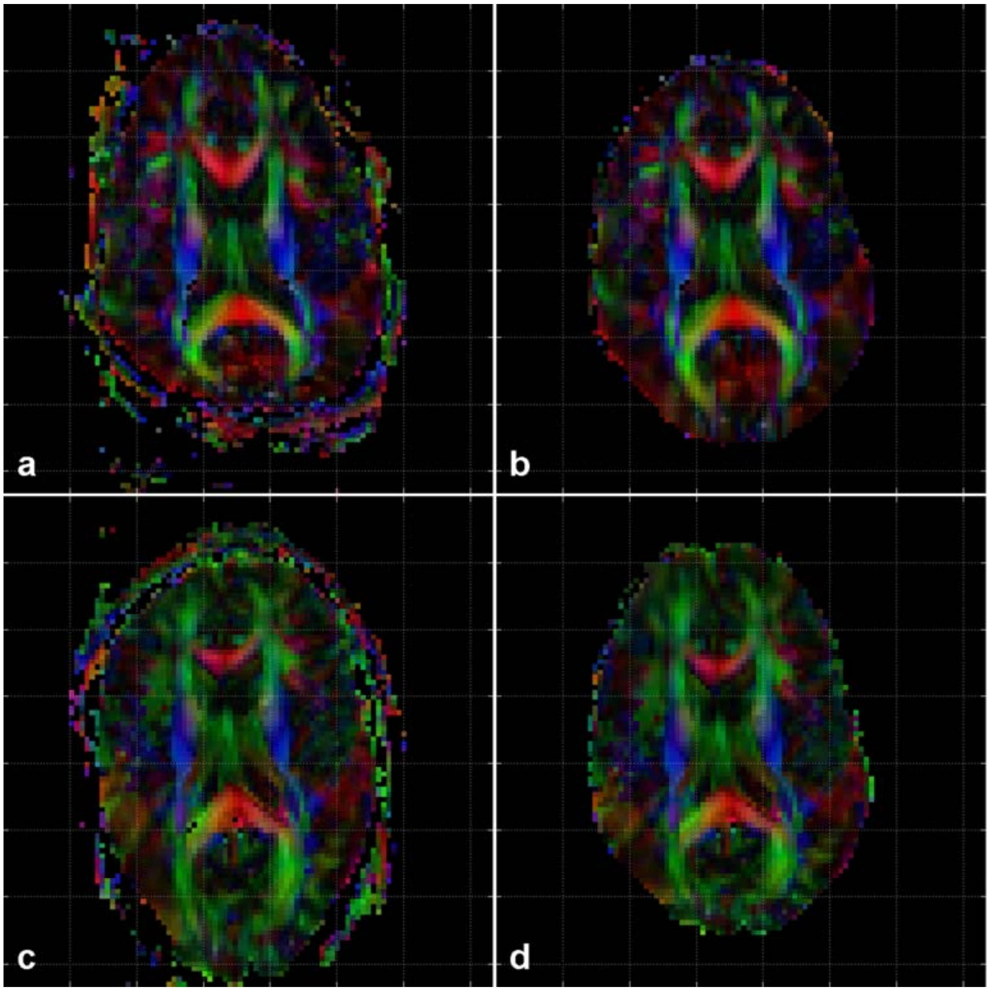

Figure 6.3. The magnified FA maps taken from Figure 6.1b and 6.1e (anterior fat shift direction) are shown in (a) and (b), and those from Figure 6.2b and 6.2e (posterior fat shift) in (c) and (d), respectively. Although the subject's head has moved slightly in the through-plane direction between scans, the anterior and posterior edges of the brain are in good agreement.

A shown in Figure 6.3, the magnified FA maps clearly show the image distortion due to the effect of field inhomogeneity and its correction for both data with anterior and posterior fat shift direction phase encoding. Figure 6.4 shows the FA map of an image slice overlaid on the anatomical T1 weighted image without (Figure 6.4a) and with (Figure 6.4b) the field inhomogeneity correction in the coronal orientation. The FA map is calculated from the DW data set with the phase encoding in the left fat shift direction for the subject.

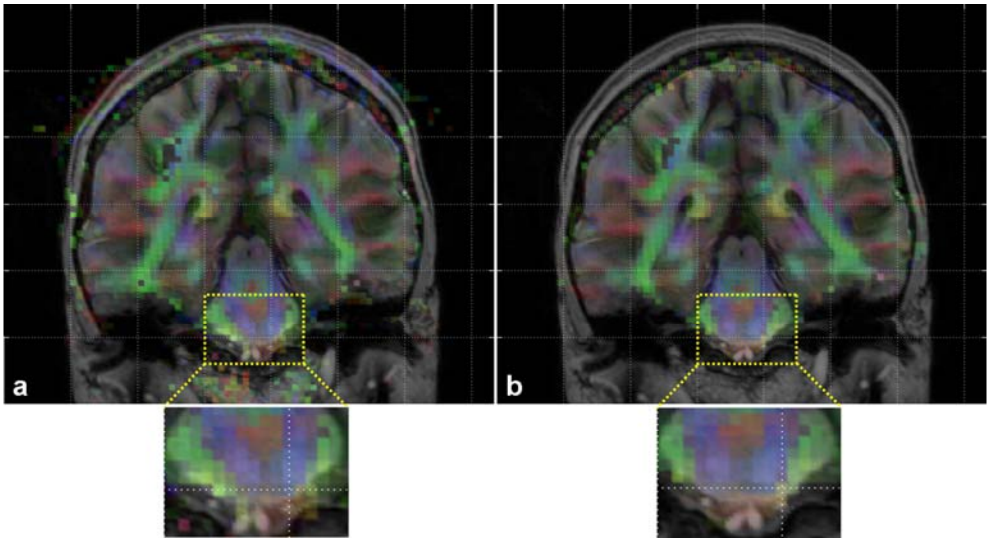

Figure 6.4. The FA maps overlaid on the T1 weighted anatomical image are shown without (a) and with the distortion correction (b). The FA map is calculated from the DW data set with the phase encoding in the left direction for the subject. An ROI and its magnification are drawn in each figure to verify the correction of the distortion. White grid dotted lines are also shown in each figure to compare the anatomical position of white matter structures shown in both of the FA maps.

The two ROIs and their magnification in each of Figure 6.4a and 6.4b show that the anatomical location of the white matter structures are corrected after the inhomogeneity correction.

The position of white matter structures before and after the correction can be more easily verified using an FOD map. Figure 6.5 shows the map of FOD function for the same image slice as used in Figure 6.4. FODs are color coded according to their orientation, represented in red (left-right), blue (inferior-superior) and green (anterior-posterior) for the subject.

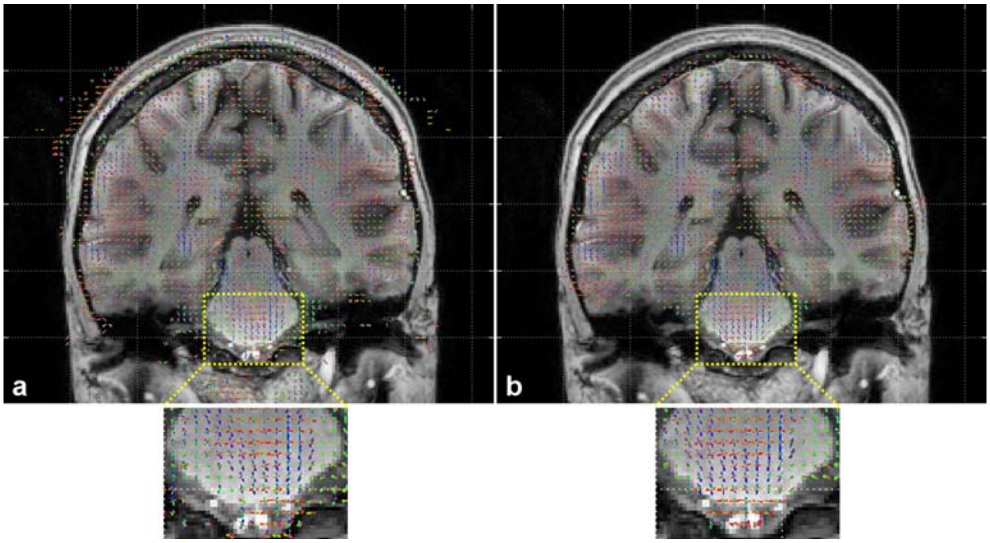

Figure 6.5. The FOD maps overlaid on the T1 weighted anatomical image are shown without (a) and with the distortion correction (b). The FOD map is calculated from the DW data set with the phase encoding in the left direction for the subject. An ROI and its magnification are drawn in each figure to verify the correction of the distortion. White

(Figure 6.5. Continued.)
grid dotted lines are also shown in each figure to compare the anatomical position of white matter structures shown in both of the FOD maps.

After the correction of the field inhomogeneity effect as shown in Figure 6.5b, the FOD map represents more accurate alignment of the anatomical structures of the white matter fibers than those without the correction (Figure 6.5a) as shown on the T1 weighted image.

6.5. Discussion and Conclusion

This study demonstrates the feasibility and usefulness of field maps for the correction of image distortions due to magnetic field inhomogeneity at 7 Tesla. As shown in Figures 6.1a and 6.2a, there are especially large geometric distortions due to field inhomogeneity effects. However, most of the distortions are corrected with the use of the fieldmap (Figures 6.1d and 6.2d) for both the anterior and posterior phase encoding, and more accurate delineation of white matter anatomical structures can be achieved as seen from the FA maps (Figures 6.1e, 6.2e, 6.3b, 6.3d and 6.4b) as well as the FOD map (Figure 6.5b). After correction, the NMI index is increased from 1.11 to 1.15 for the whole image volume between T1 weighted and FA map indicating an increase in the accuracy of image registration.

We conclude that using the fieldmap is very helpful in DW-MRI for more accurate representation of FA and FOD maps and may also be beneficial for constructing atlases of human white matter [128] as well as fiber tractography. With the correction of other sources of artifacts, such as gradient nonlinearity or B1 inhomogeneity, further improvements in structural and functional imaging may be possible at 7 Tesla.

CHAPTER Ⅶ

CONCLUSION

In this thesis we have developed the methods for improved imaging of brain white matter using diffusion tensor imaging (DTI) and high angular resolution diffusion imaging (HARDI), which provide information on the microstructure of a tissue based on water molecular diffusion. We characterized the effect of image noise on the estimation of local fiber direction in terms of the ‘cone of uncertainty’ (CU) using DTI. The CU is especially useful for understanding the uncertainty of the observed fiber path characterized by the major and minor cone angles. We showed that the uncertainty in the fiber path or the cone angle is dependent on the image SNR, eigenvalue contrast, tensor error, and FA. We also demonstrated that the angular coincidence between the CU and tensor is determined by the diffusion weighting gradient vector set relative to the tensor eigenframe with simulation and *in vivo* results.

We studied the presence of multiple fibers in a single voxel using HARDI with a spherical deconvolution (SD) method. Because the tensor model is a voxel-averaged quantity and it has only a single directional maximum, it is inaccurate in regions with multiple or nonparallel fibers. We investigated the optimum method for representing multiple fibers by means of the fiber orientation distribution function (FOD) using the SD method, especially the FORECAST (Fiber ORientation Estimated using Continuous Axially Symmetric Tensors) model, using several regularization methods and constraint functions. Because the use of each of the regularization methods in the FOD reconstruction has not been studied extensively yet, we demonstrated that the FOD can be represented more robustly and reliably over diverse imaging parameters, i.e., SNR, the number of diffusion weighting directions, *b*-value, fiber separation angle, maximum spherical harmonic expansion order, and number of fibers.

The main benefits of using the FORECAST model are that the FOD can be represented with higher angular resolution at relatively lower *b*-value, it is less computationally demanding and provides an analytic expression for the signal response or kernel function for a single fiber. Using the analytic kernel expression, we showed that the diffusion properties, e.g., volume fraction and radial diffusivity, for an individual fiber bundle could be estimated within a voxel. In addition, the FOD and diffusion properties for each fiber bundle could be isolated in voxels containing two crossing fiber bundles, i.e., the cingulum and corpus callosum. Moreover, in a region containing two fiber bundles, the orientation of a principal eigenvector of a diffusion tensor is closer to the orientation of the fiber whose volume fraction is larger and diffusion anisotropy is higher (in the case of comparable volume fraction). We assumed, however, that the accurate measurement of non-DW signal (S_0) and relatively high SNR (above 80) could be achieved in our experiments. In a future study we may relax those assumptions with an improved model, e.g., Bayesian estimation.

Although there is a boost of SNR in ultra high field MR data, there are increased RF power requirements and artifacts due to nonuniform B0 and B1. These artifacts become more significant with the use of the EPI sequence. In this study, however, we demonstrated the feasibility of DTI and HARDI in a 7 Tesla human scanner with corrections of geometric distortions due to eddy currents and B0 field inhomogeneities. The field inhomogeneity artifact was corrected using a field map, and then the correction was verified using data acquired with two opposite phase encoding directions. Also the corrections in FA and FOD maps were verified by overlaying those maps on the high resolution T1 weighted anatomical image in both the axial and coronal orientations. With the field map correction, more accurate delineation of anatomical white matter structures could be achieved. The corrections of other sources of artifacts, e.g., B1 inhomogeneity or gradient nonlinearity, may provide improved structural and functional information performed from ultra high field MR scanners.

We have investigated improved human brain white matter imaging methods using DTI and HARDI in 3 Tesla and 7 Tesla. The study about the CU provides more accurate information on the estimation of fiber tracking using DTI, and the HARDI study provides complementary information that DTI cannot. If analyzed together, more accurate fiber tracking in the region of crossing fibers and fiber specific information can be provided, their combination may enable us to better infer the changes of structure and connectivity due to certain brain dysfunctions, development or aging.

APPENDICES

A. EIGENVECTOR COVARIANCE IN THE LIMIT OF HIGH ANGULAR RESOLUTION

We assume that the measured DTI signal in a voxel in the brain is

$$S = S_0 \cdot \exp\left(-b \sum_{i,j=1}^{3} n_i n_j D_{ij} \right) + \varepsilon \,, \tag{A.1}$$

where S_0 is the non-diffusion weighted signal, *b* is the scalar diffusion weighting factor, and n_i is the i^{th} component of a unit vector along the diffusion weighting direction (n_1, n_2, and n_3 are the x, y, and z components, respectively). The D_{ij} are elements of the diffusion tensor and ε a random sample of normally distributed (mean zero, variance σ^2) noise. Assuming the signal-to-noise ratio in the diffusion weighted images is $>> 1$, this relation can be linearized as follows

$$S = S_0 \cdot \exp\left(-b \sum_{i,j=1}^{3} n_i n_j D_{ij} \right) \cdot \left(1 + \frac{\varepsilon}{\langle S \rangle} \right),$$

$$\begin{aligned} \ln(S) &= \ln(S_0) - b \sum_{i,j=1}^{3} n_i n_j D_{ij} + \ln\left(1 + \frac{\varepsilon}{\langle S \rangle} \right) \\ &\cong \ln(S_0) - b \sum_{i,j=1}^{3} n_i n_j D_{ij} + \frac{\varepsilon}{\langle S \rangle} \end{aligned} \,, \tag{A.2}$$

where $\langle S \rangle$ is the expectation value of the signal. Suppose N measurements are made using the same diffusion weighting factor, b, but different directions. Writing (A.2) explicitly for the k^{th} measurement,

$$\begin{aligned}\ln(S_k) \cong \ln(S_0) - b[x_k^2 D_{xx} + y_k^2 D_{yy} + z_k^2 D_{zz} + \\ 2x_k y_k D_{xy} + 2x_k z_k D_{xz} + 2y_k z_k D_{yz}] + \eta_k\end{aligned}, \tag{A.3}$$

where $\eta_k \equiv \varepsilon_k / \langle S_k \rangle$ is a random variable equal to the image noise scaled by the mean signal for that measurement direction. Since the variance of η_k will generally depend on direction, a weighted least squares calculation should be used to estimate the D_{ij}. Let $\boldsymbol{y}$ be a column vector of elements $y_k = \ln(S_k)$ and $\boldsymbol{\eta}$ be a column vector of values η_k. The variables we wish to estimate can be placed in a column vector $\boldsymbol{\beta}$ with elements

$$\boldsymbol{\beta}^{\mathrm{T}} = \begin{pmatrix} \ln(S_0) & bD_{xx} & bD_{yy} & bD_{zz} & bD_{xy} & bD_{xz} & bD_{yz} \end{pmatrix}. \tag{A.4}$$

Finally, the design matrix, $\tilde{\boldsymbol{A}}$, relates $\boldsymbol{\beta}$ to $\boldsymbol{y}$. The k^{th} row of $\tilde{\boldsymbol{A}}$ is

$$A_{k:} = \begin{pmatrix} 1 & -x_k^2 & -y_k^2 & -z_k^2 & -2x_k y_k & -2x_k z_k & -2y_k z_k \end{pmatrix}. \tag{A.5}$$

So (A.3) can be written simultaneously for all k as [20]

$$\boldsymbol{y} = \tilde{\boldsymbol{A}} \cdot \boldsymbol{\beta} + \boldsymbol{\eta}. \tag{A.6}$$

Defining a diagonal matrix $\tilde{\boldsymbol{V}}$ with nonzero elements equal to the signal-to-noise ratio (SNR) of the k^{th} measurement,

$$V_{kk} = \frac{\langle S_k \rangle}{\sigma}, \tag{A.7}$$

where σ^2 is the variance of the ε_k, we can multiply (A.6) by $\tilde{V}$ from the left:

$$\tilde{\boldsymbol{V}}\boldsymbol{y} = \tilde{\boldsymbol{V}}\tilde{\boldsymbol{A}} \cdot \boldsymbol{\beta} + \tilde{\boldsymbol{V}}\boldsymbol{\eta} . \tag{A.8}$$

The last term on the right is a random vector, each element of which has zero mean and unit variance. The linear least-squares solution to this uniform-variance problem is

$$\boldsymbol{\beta} = \left(\tilde{\boldsymbol{A}}^T\tilde{\boldsymbol{V}}^2\tilde{\boldsymbol{A}}\right)^{-1} \tilde{\boldsymbol{A}}^T\tilde{\boldsymbol{V}}^2\boldsymbol{y} . \tag{A.9}$$

The covariance matrix for $\boldsymbol{\beta}$ is

$$\tilde{\boldsymbol{\Sigma}}_\beta = \left(\tilde{\boldsymbol{A}}^T\tilde{\boldsymbol{V}}^2\tilde{\boldsymbol{A}}\right)^{-1} . \tag{A.10}$$

We can use the approach of Batchelor et al. [129] to evaluate elements of the covariance matrix in the limit of many diffusion encoding directions. Let the number of diffusion weighting directions, *N*, approach infinity and the directions be uniformly distributed in space. In this case, the labeling of the coordinate axes is arbitrary, so we are free to make $\hat{z}$ (the unit vector in the Z direction) parallel to the major eigenvector, $\mathbf{v}_1$, of the tensor. Similarly, we take $\hat{x}$ and $\hat{y}$ in the $\mathbf{v}_2$ and $\mathbf{v}_3$ directions, respectively. In this coordinate system,

$$\begin{aligned} V_{kk} &= \frac{S_0}{\sigma} \cdot \exp\left[-b\sum_{i,j=1}^{3} n_i\left(k\right)n_j\left(k\right)D_{ij}\right] \\ &= \frac{S_0}{\sigma} \cdot \exp\left[-b\left(\lambda_2 x_k^2 + \lambda_3 y_k^2 + \lambda_1 z_k^2\right)\right] \end{aligned} . \tag{A.11}$$

The first term on the right hand side is the SNR in an unweighted image. Consider the matrix

$$\begin{aligned}\tilde{\boldsymbol{M}} &\equiv \frac{\boldsymbol{4\pi}}{\boldsymbol{N}}\cdot\tilde{\boldsymbol{\Sigma}}_{\beta}^{-1}\\ &= \frac{\boldsymbol{4\pi}}{\boldsymbol{N}}\cdot\tilde{\boldsymbol{A}}^{\boldsymbol{T}}\tilde{\boldsymbol{V}}^{\boldsymbol{2}}\tilde{\boldsymbol{A}}\end{aligned}, \tag{A.12}$$

the matrix elements of which are

$$\begin{aligned}M_{ij} &= \frac{4\pi}{N}\cdot\sum_{k,l=1}^{N}\left(\tilde{\boldsymbol{A}}^{\boldsymbol{T}}\right)_{ik}\left(\tilde{\boldsymbol{V}}^{2}\right)_{kl}\left(\tilde{\boldsymbol{A}}\right)_{lj}\\ &= \frac{4\pi}{N}\cdot\sum_{k=1}^{N}A_{ki}V_{kk}^{2}A_{kj}\end{aligned}, \tag{A.13}$$

since $\tilde{\boldsymbol{V}}$ is diagonal. The sum is over diffusion weighting directions, each of which corresponds to a point $\left(x_k, y_k, z_k\right)$ on the unit sphere. The rows of $\tilde{\boldsymbol{A}}$ correspond to different directions and the columns to different functions of those directions. We can write

$$A_{ki} = a_i\left(x_k, y_k, z_k\right), \tag{A.14}$$

where

$$a_i = \begin{cases} 1 & for \quad i=1\\ -x^2 & \quad\quad\ i=2\\ -y^2 & \quad\quad\ i=3\\ -z^2 & \quad\quad\ i=4\\ -2xy & \quad\quad\ i=5\\ -2xz & \quad\quad\ i=6\\ -2yz & \quad\quad\ i=7\end{cases}. \tag{A.15}$$

Hence,

$$M_{ij} = \frac{4\pi}{N}\sum_{k=1}^{N}a_i\left(x_k, y_k, z_k\right)\cdot V_{kk}^{2}\cdot a_j\left(x_k, y_k, z_k\right). \tag{A.16}$$

As $N \to \infty$, we can define $ds = 4\pi/N$ as the area on the unit sphere surrounding each measurement direction $\left(x_k, y_k, z_k\right)$, and replace the summation in (A.16) with an integral over the unit sphere:

$$M_{ij} = \left(\frac{S_0}{\sigma}\right)^2 \cdot \iint a_i(x,y,z)a_j(x,y,z)\exp[-2b(\lambda_2 x^2 + \lambda_3 y^2 + \lambda_1 z^2)]ds, \tag{A.17}$$

where (A.11) was used to substitute for V_{kk}. Note that the a_i for $i = 1,2,3,4$ and the exponential term are even functions in *x*, *y*, and *z*. On the other hand, the a_i for $i = 5,6,7$ are odd in two of the three coordinates. This implies that

$$M_{ij} = 0 \text{ for } i \in \{1,2,3,4\} \text{ and } j \in \{5,6,7\}, \tag{A.18}$$

or vice versa. Hence $\tilde{\boldsymbol{M}}$ is block diagonal and can written as

$$\tilde{\boldsymbol{M}} = \begin{pmatrix} \tilde{\boldsymbol{P}} & \tilde{\boldsymbol{0}}_{4\times 3} \\ \tilde{\boldsymbol{0}}_{3\times 4} & \tilde{\boldsymbol{Q}} \end{pmatrix}, \tag{A.19}$$

where $\tilde{\boldsymbol{P}}$ is 4×4, $\tilde{\boldsymbol{Q}}$ is 3×3 and $\tilde{\boldsymbol{0}}_{n\times m}$ is an *n*×*m* matrix of zeros. Furthermore, $\tilde{\boldsymbol{Q}}$ is diagonal, since the product of any two of the functions xy, xz, and yz is also odd in two of the coordinates. The diagonal elements of $\tilde{\boldsymbol{Q}}$ are

$$Q_{11} = \left(\frac{2S_0}{\sigma}\right)^2 \cdot \iint x^2 y^2 \exp\left[-2b\left(\lambda_2 x^2 + \lambda_3 y^2 + \lambda_1 z^2\right)\right]ds, \tag{A.20}$$

$$Q_{22} = \left(\frac{2S_0}{\sigma}\right)^2 \cdot \iint x^2 z^2 \exp\left[-2b\left(\lambda_2 x^2 + \lambda_3 y^2 + \lambda_1 z^2\right)\right]ds, \tag{A.21}$$

$$Q_{33} = \left(\frac{2S_0}{\sigma}\right)^2 \cdot \iint y^2 z^2 \exp\left[-2b\left(\lambda_2 x^2 + \lambda_3 y^2 + \lambda_1 z^2\right)\right]ds. \tag{A.22}$$

Next, we show that $Q_{33} \geq Q_{22}$. We can rewrite the Q_{ii} explicitly in terms of the polar and azimuthal angles, θ and ϕ, describing each diffusion weighting direction. First, note that

$$\begin{aligned}\lambda_2 x^2 + \lambda_3 y^2 + \lambda_1 z^2 &= \lambda_2 \cos^2\phi \sin^2\theta + \lambda_3 \sin^2\phi \sin^2\theta + \lambda_1 \cos^2\theta \\ &= \lambda_2 \cos^2\phi \sin^2\theta + \lambda_3\left(1-\cos^2\phi\right)\sin^2\theta + \lambda_1\left(1-\sin^2\theta\right). \\ &= \lambda_1 + \sin^2\theta\left[\left(\lambda_2-\lambda_3\right)\cos^2\phi - \left(\lambda_1-\lambda_3\right)\right]\end{aligned} \quad \text{(A.23)}$$

Hence the lower two diagonal elements are

$$\begin{gathered}Q_{22} = \left(\frac{2S_0}{\sigma}\right)^2 \cdot \int_0^{\pi} \left[\int_0^{2\pi} \cos^2\phi \exp\left\{-2b\sin^2\theta\cos^2\phi\left(\lambda_2-\lambda_3\right)\right\} d\phi\right] \cdot \\ \sin^3\theta\cos^2\theta\exp\left\{-2b\left[\lambda_1 - \sin^2\theta\left(\lambda_1-\lambda_3\right)\right]\right\} d\theta\end{gathered}, \quad \text{(A.24)}$$

$$\begin{gathered}Q_{33} = \left(\frac{2S_0}{\sigma}\right)^2 \cdot \int_0^{\pi} \left[\int_0^{2\pi} \sin^2\phi \exp\left\{-2b\sin^2\theta\cos^2\phi\left(\lambda_2-\lambda_3\right)\right\} d\phi\right] \cdot \\ \sin^3\theta\cos^2\theta\exp\left\{-2b\left[\lambda_1 - \sin^2\theta\left(\lambda_1-\lambda_3\right)\right]\right\} d\theta\end{gathered}. \quad \text{(A.25)}$$

These differ only in the ϕ integrals. The ϕ integrals for Q_{22} and Q_{33} are

$$H_{22}(\alpha) \equiv \int_0^{2\pi} \cos^2\phi \cdot e^{-\alpha\cdot\cos^2\phi} d\phi, \quad \text{(A.26)}$$

$$H_{33}(\alpha) \equiv \int_0^{2\pi} \sin^2\phi \cdot e^{-\alpha\cdot\cos^2\phi} d\phi, \quad \text{(A.27)}$$

respectively, with $\alpha = 2b\left(\lambda_2-\lambda_3\right)\sin^2\theta \geq 0$. These integrals can be expressed as modified Bessel functions using the relation

$$I_0(z) = \frac{1}{\pi}\int_0^{\pi} e^{\pm z\cdot\cos\phi'} d\phi', \quad \text{(A.28)}$$

$I_0(z)$ is the modified Bessel function of order zero. Making the change of variables to $\phi = \phi'/2$ and using the half angle relation $\cos(2\phi) = 2\cos^2\phi - 1$ we have

$$\begin{aligned} I_0(z) &= 2\frac{e^z}{\pi}\cdot\int_0^{\pi/2} e^{-2z\cos^2\phi}d\phi \\ &= \frac{e^z}{2\pi}\cdot\int_0^{2\pi} e^{-2z\cos^2\phi}d\phi \end{aligned}. \tag{A.29}$$

Hence

$$I_0(z/2) = \frac{e^{z/2}}{2\pi}\cdot\int_0^{2\pi} e^{-z\cdot\cos^2\phi}d\phi. \tag{A.30}$$

Differentiating both sides of this relation with respect to *z* gives

$$\frac{d}{dz}I_0(z/2) = \frac{e^{z/2}}{4\pi}\cdot\int_0^{2\pi} e^{-z\cdot\cos^2\phi}d\phi - \frac{e^{z/2}}{2\pi}\cdot\int_0^{2\pi}\cos^2\phi\cdot e^{-z\cdot\cos^2\phi}d\phi. \tag{A.31}$$

The zero order modified Bessel function obeys the relation

$$\frac{d}{dz}I_0(z) = I_1(z), \tag{A.32}$$

where $I_1(z)$ is the first order modified Bessel function. Using this relation and (A.30) in (A.31), we have

$$\frac{1}{2}I_1(z/2) = \frac{1}{2}I_0(z/2) - \frac{e^{z/2}}{2\pi}\cdot\int_0^{2\pi}\cos^2\phi\cdot e^{-z\cdot\cos^2\phi}d\phi, \tag{A.33}$$

or

$$\int_0^{2\pi}\cos^2\phi\cdot e^{-z\cdot\cos^2\phi}d\phi = \pi e^{-z/2}\left[I_0(z/2) - I_1(z/2)\right]. \tag{A.34}$$

Similarly,

$$\begin{aligned}\int_0^{2\pi} \sin^2\phi \cdot e^{-z\cdot\cos^2\phi} d\phi &= \int_0^{2\pi} \left(1-\cos^2\phi\right)\cdot e^{-z\cdot\cos^2\phi} d\phi \\ &= \int_0^{2\pi} e^{-z\cdot\cos^2\phi} d\phi - \int_0^{2\pi} \cos^2\phi \cdot e^{-z\cdot\cos^2\phi} d\phi \\ &= 2\pi e^{-z/2} I_0\left(z/2\right) - \pi e^{-z/2}\left[I_0\left(z/2\right)-I_1\left(z/2\right)\right] \\ &= \pi e^{-z/2}\left[I_0\left(z/2\right)+I_1\left(z/2\right)\right]\end{aligned} \quad , \tag{A.35}$$

using (A.30) and (A.34) on the second line. Substituting (A.34) and (A.35) in (A.26) and (A.27), respectively,

$$H_{22}\left(\alpha\right) \equiv \pi e^{-\alpha/2}\left[I_0\left(\alpha/2\right)-I_1\left(\alpha/2\right)\right], \tag{A.36}$$

$$H_{33}\left(\alpha\right) \equiv \pi e^{-\alpha/2}\left[I_0\left(\alpha/2\right)+I_1\left(\alpha/2\right)\right]. \tag{A.37}$$

Since the modified Bessel functions are real and positive for $\alpha \geq 0$, we have

$$H_{33}\left(\alpha\right) \geq H_{22}\left(\alpha\right). \tag{A.38}$$

The equality holds if and only if $\alpha = 0$ (since $I_1\left(0\right)=0$). Because these terms are the only difference between the integrands of Q_{22} and Q_{33} (and the integrands are non-negative), we have

$$Q_{33} \geq Q_{22}. \tag{A.39}$$

For the case of interest ($b > 0$) the equality holds only when $\lambda_2 = \lambda_3$.

Since the matrix $\tilde{\boldsymbol{M}}$ is block diagonal ((A.19)), its inverse is also block diagonal:

$$\tilde{\boldsymbol{M}}^{-1} = \begin{pmatrix} \tilde{\boldsymbol{P}}^{-1} & \tilde{\mathbf{0}}_{4\times3} \\ \tilde{\mathbf{0}}_{3\times4} & \tilde{\boldsymbol{Q}}^{-1} \end{pmatrix}, \tag{A.40}$$

and since $\tilde{\boldsymbol{Q}}$ is diagonal,

$$\tilde{\boldsymbol{Q}}^{-1} = \begin{pmatrix} \frac{1}{Q_{11}} & 0 & 0 \\ 0 & \frac{1}{Q_{22}} & 0 \\ 0 & 0 & \frac{1}{Q_{33}} \end{pmatrix}. \tag{A.41}$$

Substituting (A.40) and (A.41) into (A.12) and solving for the covariance matrix, we find

$$\tilde{\boldsymbol{\Sigma}}_\beta = \frac{4\pi}{\boldsymbol{N}} \cdot \tilde{\boldsymbol{M}}^{-1} = \frac{4\pi}{\boldsymbol{N}} \cdot \left(\begin{array}{c:ccc} \tilde{\boldsymbol{P}}^{-1} & & \tilde{\mathbf{0}}_{\mathbf{4x3}} & \\ \hdashline & \frac{1}{\boldsymbol{Q}_{11}} & 0 & 0 \\ \tilde{\mathbf{0}}_{\mathbf{3x4}} & 0 & \frac{1}{\boldsymbol{Q}_{22}} & 0 \\ & 0 & 0 & \frac{1}{\boldsymbol{Q}_{33}} \end{array} \right), \tag{A.42}$$

where

$$\frac{1}{Q_{22}} \geq \frac{1}{Q_{33}}. \tag{A.43}$$

Referring to the order of tensor elements in (A.4), this shows that the variance of D_{xz} is greater than or equal to the variance of D_{yz}. In terms of the principal axis indices, we have

$$\sigma^2\left(D_{12}\right) \geq \sigma^2\left(D_{13}\right). \tag{A.44}$$

The equality holds only when $\lambda_2 = \lambda_3$. Further, since the lower-right block of $\tilde{\boldsymbol{\Sigma}}_\beta$ is diagonal, the errors in D_{12} are uncorrelated with errors in D_{13}. A similar calculation shows that the same results hold if the tensor is calculated using standard (unweighted) linear least squares estimation. To summarize, in the case of many, uniformly distributed measurement directions and $\lambda_2 > \lambda_3$, the errors in D_{12} are larger than the errors in D_{13}, and the two are uncorrelated.

B. REPRESENTATION OF SPHERICAL HARMONIC COEFFICIENTS OF FOD IN MATRIX FORM

In the case of two $\lambda_\perp$ values in a voxel, the FORECAST model relating signal to FOD coefficients is

$$s_{lm}(b) = S_0\left[c_l(\lambda_{\perp 1}, b)\, p_{lm1} + c_l(\lambda_{\perp 2}, b)\, p_{lm2}\right]. \tag{B.1}$$

If measurements are made at two *b*-values, we have

$$\begin{bmatrix} s_{lm}(b_1) \\ s_{lm}(b_2) \end{bmatrix} = S_0 \begin{bmatrix} c_l(b_1, \lambda_{\perp 1}) & c_l(b_1, \lambda_{\perp 2}) \\ c_l(b_2, \lambda_{\perp 1}) & c_l(b_2, \lambda_{\perp 2}) \end{bmatrix} \cdot \begin{bmatrix} p_{lm1} \\ p_{lm2} \end{bmatrix}. \tag{B.2}$$

Defining

$$\tilde{\mathbf{c}}_l = \begin{bmatrix} c_l(b_1, \lambda_{\perp 1}) & c_l(b_1, \lambda_{\perp 2}) \\ c_l(b_2, \lambda_{\perp 1}) & c_l(b_2, \lambda_{\perp 2}) \end{bmatrix}, \tag{B.3}$$

we have

$$\begin{bmatrix} s_{lm}(b_1) \\ s_{lm}(b_2) \end{bmatrix} = S_0 \tilde{\mathbf{c}}_l \begin{bmatrix} p_{lm1} \\ p_{lm2} \end{bmatrix}. \tag{B.4}$$

The spherical harmonic coefficients of the FOD can be represented as,

$$\tilde{\mathbf{p}}_{lm} = \frac{1}{S_0}\tilde{\mathbf{E}}\cdot\tilde{\mathbf{C}}\cdot\tilde{\mathbf{H}}\,, \tag{B.5}$$

here $\tilde{\mathbf{E}}$, $\tilde{\mathbf{C}}$ and $\tilde{\mathbf{H}}$ are $n_f \times (n_f \cdot n_t)$, $(n_f \cdot n_t) \times (n_b \cdot n_t)$ and $(n_b \cdot n_t) \times n_t$ dimensional matrices, respectively, with n_t the number of all spherical harmonic expansion terms, n_f the number of fibers (i.e., $\lambda_\perp$ values) to be estimated and n_b the number of b-values.

$\tilde{\mathbf{p}}_{lm}$ is $n_f \times n_t$. $\tilde{\mathbf{H}}$ is a matrix of signal coefficients, $s_{lm}(b)$, for each of two b-values,

$$\tilde{\mathbf{H}} = \left[\begin{array}{c|c|c|c|c}
s_{0,0}(b_1) & 0 & 0 & 0 & \cdots \\
s_{0,0}(b_2) & 0 & 0 & 0 & \cdots \\
\hline
0 & s_{1,-1}(b_1) & 0 & 0 & \cdots \\
0 & s_{1,-1}(b_2) & 0 & 0 & \cdots \\
\hline
0 & 0 & s_{1,0}(b_1) & 0 & \cdots \\
0 & 0 & s_{1,0}(b_2) & 0 & \cdots \\
\hline
0 & 0 & 0 & s_{1,1}(b_1) & \cdots \\
0 & 0 & 0 & s_{1,1}(b_2) & \cdots \\
\hline
\vdots & \vdots & \vdots & \vdots & \cdots
\end{array}\right], \tag{B.6}$$

and this can be written as $\tilde{\mathbf{H}} = \bigcap_{k=1}^{n_t} h_k$, here $\bigcap$ is matrix concatenation operator and h_k is $(n_b \times n_t)$ dimensional matrix whose k^{th} column is $\left[s_{lm'}(b_1), s_{lm'}(b_2), s_{lm'}(b_3), \ldots, s_{lm'}(b_{n_b})\right]^{\mathrm{T}}$ for corresponding l, m', and b-values and is otherwise zero. In case of two b-values, the k^{th} column only contains $[s_{lm'}(b_1), s_{lm'}(b_2)]^{\mathrm{T}}$. Here $l \in \left\{\mathbb{Z} \mid \sqrt{k} - 1 \le \mathbb{Z} < \sqrt{k}\right\}$, $m \in \{\mathbb{Z} \mid -l \le \mathbb{Z} \le l\}$, and m' is the $(k - l^2)^{\text{th}}$ element in m, where $\mathbb{Z}$ is an integer in both cases.

The matrix $\tilde{\mathbf{C}}$ includes the elements of $\tilde{\mathbf{c}}_l^+ = \left(\tilde{\mathbf{c}}_l^{\mathrm{T}}\tilde{\mathbf{c}}_l\right)^{-1}\tilde{\mathbf{c}}_l^{\mathrm{T}}$ as below,

$$\tilde{\mathbf{C}} = \left[\begin{array}{cc|cccccc}
c_0^+(b_1,\lambda_{\perp 1}) & c_0^+(b_2,\lambda_{\perp 1}) & 0 & 0 & 0 & 0 & \cdots \\
c_0^+(b_1,\lambda_{\perp 2}) & c_0^+(b_2,\lambda_{\perp 2}) & 0 & 0 & 0 & 0 & \cdots \\
\hline
0 & 0 & c_1^+(b_1,\lambda_{\perp 1}) & c_1^+(b_2,\lambda_{\perp 1}) & 0 & 0 & \cdots \\
0 & 0 & c_1^+(b_1,\lambda_{\perp 2}) & c_1^+(b_2,\lambda_{\perp 2}) & 0 & 0 & \cdots \\
0 & 0 & 0 & 0 & c_1^+(b_1,\lambda_{\perp 1}) & c_1^+(b_2,\lambda_{\perp 1}) & \cdots \\
0 & 0 & 0 & 0 & c_1^+(b_1,\lambda_{\perp 2}) & c_1^+(b_2,\lambda_{\perp 2}) & \cdots \\
\vdots & \vdots & \vdots & \vdots & \vdots & \vdots & \ddots
\end{array}\right]. \quad \text{(B.7)}$$

This can be written $\tilde{\mathbf{C}} = diag\left[\tilde{\mathbf{M}}_0, \tilde{\mathbf{M}}_1, \tilde{\mathbf{M}}_2, ..., \tilde{\mathbf{M}}_L\right]$ where $\tilde{\mathbf{M}}_l = \tilde{\mathbf{I}}_{2l+1} \otimes \tilde{\mathbf{c}}_l^+$ with $c_l^+\left(b_i, \lambda_{\perp j}\right)$, i=1, ..., n_b and j=1, ..., n_f, is a matrix element of $\tilde{\mathbf{c}}_l^+$. Here $\tilde{\mathbf{I}}_{2l+1}$ is the (2l+1) × (2l+1) identity matrix and $\otimes$ is Kronecker tensor (i.e., outer) product.

$\tilde{\mathbf{E}}$ is a rearrangement matrix multiplying the left side of $\tilde{\mathbf{C}} \cdot \tilde{\mathbf{H}}$ as below,

$$\tilde{\mathbf{E}} \cdot \tilde{\mathbf{C}} \cdot \tilde{\mathbf{H}} = \underbrace{\left[\begin{array}{cc|cc|cc|cc|c}
1 & 0 & 1 & 0 & 1 & 0 & 1 & 0 & \cdots \\
0 & 1 & 0 & 1 & 0 & 1 & 0 & 1 & \cdots
\end{array}\right]}_{\tilde{\mathbf{E}}} \cdot \underbrace{\left[\begin{array}{c|ccc|c}
p_{0,0}(\lambda_{\perp 1}) & 0 & 0 & 0 & \cdots \\
p_{0,0}(\lambda_{\perp 2}) & 0 & 0 & 0 & \cdots \\
\hline
0 & p_{1,-1}(\lambda_{\perp 1}) & 0 & 0 & \cdots \\
0 & p_{1,-1}(\lambda_{\perp 2}) & 0 & 0 & \cdots \\
\hline
0 & 0 & p_{1,0}(\lambda_{\perp 1}) & 0 & \cdots \\
0 & 0 & p_{1,0}(\lambda_{\perp 2}) & 0 & \cdots \\
\hline
0 & 0 & 0 & p_{1,1}(\lambda_{\perp 1}) & \cdots \\
0 & 0 & 0 & p_{1,1}(\lambda_{\perp 2}) & \cdots \\
\hline
\vdots & \vdots & \vdots & \vdots & \cdots
\end{array}\right]}_{\tilde{\mathbf{C}} \cdot \tilde{\mathbf{H}} / S_0}, \quad \text{(B.8)}$$

here $\tilde{\mathbf{E}} = \tilde{\mathbf{1}}_{n_t}^{\mathrm{T}} \otimes \tilde{\mathbf{I}}_{n_f \times n_f}$ and $\tilde{\mathbf{1}}_{n_t}^{\mathrm{T}}$ is a column vector of n_t ones, as shown on the left side of above matrix multiplication.

Then the FOD function for all fibers, $\tilde{\mathbf{P}}(\theta,\phi)$, which is ($n_g$ × n_f) dimensional matrix is,

$$\begin{aligned}\tilde{\mathbf{P}}(\theta,\phi) &= \tilde{\mathbf{Y}}\cdot\left(\tilde{\mathbf{p}}_{lm}\right)^{\mathrm{T}} \\ &= \frac{1}{S_0}\tilde{\mathbf{Y}}\cdot\left(\tilde{\mathbf{E}}\cdot\tilde{\mathbf{C}}\cdot\tilde{\mathbf{H}}\right)^{\mathrm{T}},\end{aligned} \tag{B.9}$$

here $\tilde{\mathbf{Y}}$ is the n_g directional ($n_g \times n_t$) spherical harmonic matrix.

C. RANGE OF RADIAL DIFFUSIVITY FOR INDIVIDUAL FIBERS

For voxels containing fibers with two different $\lambda_\perp$ values, the zeroth order expansion term from (5.4) is

$$\begin{aligned} s_{0,0} &= S_0 \cdot c_0 \cdot p_{0,0} \\ &= S_0\left[c_0(\lambda_{\perp,1})p_{0,0,1} + c_0(\lambda_{\perp,2})p_{0,0,2}\right] \\ &= S_0\left[c_0(\lambda_{\perp,1})p_{0,0,1} + c_0(\lambda_{\perp,2})\left(\frac{1}{\sqrt{4\pi}} - p_{0,0,1}\right)\right]\end{aligned}, \tag{C.1}$$

here $p_{l,m,j}$ is the FOD spherical harmonic coefficient for order l, m and the j^{th} fiber. We have used the fact that the combined volume fraction of the two fibers equals one, so $p_{0,0,1} + p_{0,0,2} = \frac{1}{\sqrt{4\pi}}$. Rearranging (C.1) for $p_{0,0,1}$ gives,

$$p_{0,0,1} = \frac{\frac{s_{0,0}}{S_0} - \frac{c_0(\lambda_{\perp,2})}{\sqrt{4\pi}}}{c_0(\lambda_{\perp,1}) - c_0(\lambda_{\perp,2})}. \tag{C.2}$$

Because the mean DW signal is

$$\begin{aligned}\bar{\mathbf{S}} &= \frac{\iint \mathbf{S}(\theta,\phi)\sin(\theta)d\theta d\phi}{\iint \sin(\theta)d\theta d\phi} \\ &= \frac{1}{4\pi}\iint \mathbf{S}(\theta,\phi)\sin(\theta)d\theta d\phi\end{aligned}, \tag{C.3}$$

and considering $s_{lm} = \iint Y^*_{lm}(\theta,\phi)\mathbf{S}(\theta,\phi)\sin(\theta)d\theta d\phi$, we have $s_{0,0} = \sqrt{4\pi}\,\overline{\mathbf{S}}$. Therefore, (C.2) becomes,

$$\begin{aligned} p_{0,0,1} &= \frac{\frac{\sqrt{4\pi}\,\overline{\mathbf{S}}}{S_0} - \frac{c_0(\lambda_{\perp,2})}{\sqrt{4\pi}}}{c_0(\lambda_{\perp,1}) - c_0(\lambda_{\perp,2})} \\ &= \frac{1}{\sqrt{4\pi}}\left(\frac{\frac{4\pi\overline{\mathbf{S}}}{S_0} - c_0(\lambda_{\perp,2})}{c_0(\lambda_{\perp,1}) - c_0(\lambda_{\perp,2})}\right) \end{aligned} \qquad \text{(C.4)}$$

Because $0 < p_{0,0,1} < \frac{1}{\sqrt{4\pi}}$, (C.4) can be expressed as

$$0 < \left(\frac{\frac{4\pi\overline{\mathbf{S}}}{S_0} - c_0(\lambda_{\perp,2})}{c_0(\lambda_{\perp,1}) - c_0(\lambda_{\perp,2})}\right) < 1. \qquad \text{(C.5)}$$

Now $c_0(\lambda_\perp)$ is a monotonically decreasing function of $\lambda_\perp$. If we assume $\lambda_{\perp,1} < \lambda_{\perp,2}$, then $c_0(\lambda_{\perp,2}) < \frac{4\pi\overline{\mathbf{S}}}{S_0}$ from above. This places a lower bound on $\lambda_{\perp,2}$. Similarly, $\frac{4\pi\overline{\mathbf{S}}}{S_0} < c_0(\lambda_{\perp,1})$, which gives an upper bound for $\lambda_{\perp,1}$.

Using (C.1) for the single $\lambda_\perp$ case,

$$\frac{4\pi\overline{\mathbf{S}}}{S_0} = c_0\left(\lambda_{\perp,s}\right). \qquad \text{(C.6)}$$

Hence, $c_0\left(\lambda_{\perp,2}\right) < c_0\left(\lambda_{\perp,s}\right)$ and $c_0\left(\lambda_{\perp,s}\right) < c_0\left(\lambda_{\perp,1}\right)$. Using (C.6), Equation (C.5) becomes,

$$0 < \left(\frac{c_0\left(\lambda_{\perp,s}\right) - c_0\left(\lambda_{\perp,2}\right)}{c_0\left(\lambda_{\perp,1}\right) - c_0\left(\lambda_{\perp,2}\right)}\right) < 1. \qquad \text{(C.7)}$$

Again considering that $c_0\left(\lambda_\perp\right)$ is a decreasing function, the possible range for each radial diffusivity is

$$0 \leq \lambda_{\perp,1} < \lambda_{\perp,s}, \tag{C.8}$$

$$\lambda_{\perp,s} < \lambda_{\perp,2} \leq \bar{\lambda}, \tag{C.9}$$

for the case of two fiber diffusion.

REFERENCES

1. Einstein A. *Investigations on the theory of the Brownian movement*. New York: Dover Publications; 1956.

2. Callaghan PT. *Principles of nuclear magnetic resonance microscopy*. New York: Oxford University Press; 1991.

3. Karger J, Heink W. The propagator representation of molecular transport in microporous crystallites. *J Magn Reson* 1983;51:1-7.

4. McNaught AD, Wilkinson A, Jenkins AD. *IUPAC compendium of chemical terminology: the gold book*. Research Triangle Park, NC: International Union of Pure and Applied Chemistry; 2006. [Web; http://goldbook.iupac.org/].

5. Tuch DS. *Diffusion MRI of complex tissue structure*. Cambridge: Harvard University-Massachusetts Institute of Technology; 2002. [Ph. D. thesis].

6. Mori S. *Introduction to diffusion tensor imaging*. New York: Elsevier; 2007.

7. Hahn EL. Spin echoes. *Phys Rev* 1950;80:580-594.

8. Carr HY, Purcell EM. Effects of diffusion on free precession in nuclear magnetic resonance experiments. *Phys Rev* 1954;94:630-638.

9. Stejskal EO, Tanner JE. Spin diffusion measurements: Spin echoes in the presence of a time-dependent field gradient. *J Chem Phys* 1965;42:288-292.

10. Torrey HC. Bloch equations with diffusion terms. *Phys Rev* 1956;104:563-565.

11. Bloch F. Nuclear induction. *Phys Rev* 1946;70:460-474.

12. Cleveland GG, Chang DC, Hazlewood CF, Rorschach HE. Nuclear magnetic

resonance measurement of skeletal muscle: anisotrophy of the diffusion coefficient of the intracellular water. *Biophys J* 1976;16:1043-1053.

13. Le Bihan D, Breton E, Lallemand D, Grenier P, Cabanis E, Laval-Jeantet M. MR imaging of intravoxel incoherent motions: application to diffusion and perfusion in neurologic disorders. *Radiology* 1986;161:401-407.

14. Moseley ME, Cohen Y, Kucharczyk J, Mintorovitch J, Asgari HS, Wendland MF, Tsuruda J, Norman D. Diffusion-weighted MR imaging of anisotropic water diffusion in cat central nervous system. *Radiology* 1990;176:439-445.

15. Zhong JH, Gore JC. Studies of restricted diffusion in heterogeneous media containing variations in susceptibility. *Magn Reson Med* 1991;19(2):276-284.

16. Beaulieu C. The basis of anisotropic water diffusion in the nervous system - a technical review. *NMR Biomed* 2002;15:435-455.

17. Beaulieu C, Allen PS. Water diffusion in the giant axon of the squid: implications for diffusion-weighted MRI of the nervous system. *Magn Reson Med* 1994;32:579-583.

18. Beaulieu C, Allen PS. Determinants of anisotropic water diffusion in nerves. *Magn Reson Med* 1994;31:394-400.

19. Basser PJ, Mattiello J, LeBihan D. MR diffusion tensor spectroscopy and imaging. *Biophys J* 1994;66:259-267.

20. Basser PJ, Mattiello J, LeBihan D. Estimation of the effective self-diffusion tensor from the NMR spin echo. *J Magn Reson Ser B* 1994;103:247-254.

21. Basser PJ. Inferring microstructural features and the physiological state of tissues from diffusion-weighted images. *NMR Biomed* 1995;8:333-344.

22. Basser PJ, Mattiello J, LeBihan D. Diagonal and off-diagonal components of the self-diffusion tensor: their relation to and estimation from the NMR spin-echo signal. In: *Proceedings of the 11th Annual Meeting of SMRM*, Berlin, Germany,

1992. p 1222.

23. Basser PJ, Pierpaoli C. A simplified method to measure the diffusion tensor from seven MR images. *Magn Reson Med* 1998;39:928-934.

24. Jones DK, Horsfield MA, Simmons A. Optimal strategies for measuring diffusion in anisotropic systems by magnetic resonance imaging. *Magn Reson Med* 1999;42:515-525.

25. Koay CG, Chang LC, Carew JD, Pierpaoli C, Basser PJ. A unifying theoretical and algorithmic framework for least squares methods of estimation in diffusion tensor imaging. *J Magn Reson* 2006;182:115-125.

26. Basser PJ, Pierpaoli C. Microstructural and physiological features of tissues elucidated by quantitative-diffusion-tensor MRI. *J Magn Reson Ser B* 1996;111:209-219.

27. Basser PJ. Fiber-tractography via diffusion tensor MRI (DT-MRI). In: *Proceedings of the 6th Annual Meeting of ISMRM*, Sydney, Australia, 1998. p 1226.

28. Basser PJ, Pajevic S, Pierpaoli C, Duda J, Aldroubi A. In vivo fiber tractography using DT-MRI data. *Magn Reson Med* 2000;44:625-632.

29. Mori S, Crain BJ, Chacko VP, van Zijl PC. Three-dimensional tracking of axonal projections in the brain by magnetic resonance imaging. *Ann Neurol* 1999;45:265-269.

30. Mori S, van Zijl PC. Fiber tracking: principles and strategies - a technical review. *NMR Biomed* 2002;15:468-480.

31. Behrens TE, Johansen-Berg H, Woolrich MW, Smith SM, Wheeler-Kingshott CA, Boulby PA, Barker GJ, Sillery EL, Sheehan K, Ciccarelli O, Thompson AJ, Brady JM, Matthews PM. Non-invasive mapping of connections between human thalamus and cortex using diffusion imaging. *Nat Neurosci* 2003;6:750-757.

32. Le Bihan D. Looking into the functional architecture of the brain with diffusion MRI. *Nat Rev Neurosci* 2003;4:469-480.

33. Edelman RR, Gaa J, Wedeen VJ, Loh E, Hare JM, Prasad P, Li W. In vivo measurement of water diffusion in the human heart. *Magn Reson Med* 1994;32:423-428.

34. Damon BM, Ding Z, Anderson AW, Freyer AS, Gore JC. Validation of diffusion tensor MRI-based muscle fiber tracking. *Magn Reson Med* 2002;48:97-104.

35. Lansdown DA, Ding Z, Wadington M, Hornberger JL, Damon BM. Quantitative diffusion tensor MRI-based fiber tracking of human skeletal muscle. *J Appl Physiol* 2007;103:673-681.

36. Thoeny HC, De Keyzer F, Oyen RH, Peeters RR. Diffusion-weighted MR imaging of kidneys in healthy volunteers and patients with parenchymal diseases: initial experience. *Radiology* 2005;235:911-917.

37. Takahara T, Imai Y, Yamashita T, Yasuda S, Nasu S, Van Cauteren M. Diffusion weighted whole body imaging with background body signal suppression (DWIBS): technical improvement using free breathing, STIR and high resolution 3D display. *Radiat Med* 2004;22:275-282.

38. Bastin ME, Armitage PA, Marshall I. A theoretical study of the effect of experimental noise on the measurement of anisotropy in diffusion imaging. *Magn Reson Imaging* 1998;16:773-785.

39. Pierpaoli C, Basser PJ. Toward a quantitative assessment of diffusion anisotropy. *Magn Reson Med* 1996;36:893-906.

40. Skare S, Li TQ, Nordell B, Ingvar M. Noise considerations in the determination of diffusion tensor anisotropy. *Magn Reson Imaging* 2000;18:659-669.

41. Anderson AW. Theoretical analysis of the effects of noise on diffusion tensor imaging. *Magn Reson Med* 2001;46:1174-1188.

42. Basser PJ, Pajevic S. Statistical artifacts in diffusion tensor MRI (DT-MRI) caused by background noise. *Magn Reson Med* 2000;44:41-50.

43. Basser PJ. Quantifying errors in fiber-tract direction and diffusion tensor field maps resulting from MR noise. In: *Proceedings of the 5th Annual Meeting of ISMRM*, Vancouver, Canada, 1997. p 1740.

44. Chang LC, Koay CG, Pierpaoli C, Basser PJ. Variance of estimated DTI-derived parameters via first-order perturbation methods. *Magn Reson Med* 2007;57:141-149.

45. Koay C, Chang L-C, Basser PJ. The cone of uncertainty is elliptical: Implications for DTI tractography. In: *Proceedings of the 15th Annual Meeting of ISMRM*, Berlin, Germany, 2007. p 1602.

46. Hext GR. The estimation of second-order tensors, with related tests and designs. *Biometrika* 1963;50:353-373.

47. Jeong H-K, Lu Y, Ding Z, Anderson AW. Characterizing cone of uncertainty in diffusion tensor MRI. In: *Proceedings of the 13th Annual Meeting of ISMRM*, Miami Beach, USA, 2005. p 1317.

48. Jones DK. Determining and visualizing uncertainty in estimates of fiber orientation from diffusion tensor MRI. *Magn Reson Med* 2003;49:7-12.

49. Lazar M, Alexander AL. Bootstrap white matter tractography (BOOT-TRAC). *Neuroimage* 2005;24:524-532.

50. Lazar M, Lee JH, Alexander AL. Axial asymmetry of water diffusion in brain white matter. *Magn Reson Med* 2005;54:860-867.

51. Efron B. Bootstrap methods: another look at the jackknife. *Ann Stat* 1979;7:1-26.

52. Pajevic S, Basser PJ. Parametric and non-parametric statistical analysis of DT-MRI data. *J Magn Reson* 2003;161:1-14.

53. Chen B, Hsu EW. Noise removal in magnetic resonance diffusion tensor imaging. *Magn Reson Med* 2005;54:393-407.

54. Ding Z, Gore JC, Anderson AW. Reduction of noise in diffusion tensor images using anisotropic smoothing. *Magn Reson Med* 2005;53:485-490.

55. Parker GJ, Schnabel JA, Symms MR, Werring DJ, Barker GJ. Nonlinear smoothing for reduction of systematic and random errors in diffusion tensor imaging. *J Magn Reson Imaging* 2000;11:702-710.

56. Frank LR. Anisotropy in hign angular resolution diffusion-weighted MRI. *Magn Reson Med* 2001;45:935-939.

57. Frank LR. Characterization of anisotropy in high angular resolution diffusion-weighted MRI. *Magn Reson Med* 2002;47:1083-1099.

58. Pierpaoli C, Jezzard P, Basser PJ, Barnett A, Di Chiro G. Diffusion tensor MR imaging of the human brain. *Radiology* 1996;201:637-648.

59. Alexander AL, Hasan KM, Lazar M, Tsuruda JS, Parker DL. Analysis of partial volume effects in diffusion-tensor MRI. *Magn Reson Med* 2001;45:770-780.

60. Anderson AW, Ding Z. Sub-voxel measurement of fiber orientation using high angular resolution diffusion tensor imaging. In: *Proceedings of the 10th Annual Meeting of ISMRM*, Honolulu, USA, 2002. p 440.

61. Conturo TE, Lori NF, Cull TS, Akbudak E, Snyder AZ, Shimony JS, McKinstry RC, Burton H, Raichle ME. Tracking neuronal fiber pathways in the living human brain. *P Natl Acad Sci USA* 1999;96:10422-10427.

62. Frank LR. Characterization of anisotropy in high angular resolution diffusion weighted MRI. In: *Proceedings of the 9th Annual Meeting of ISMRM*. Glasgow, Scotland, 2001. p 1531.

63. Le Bihan D, van Zijl P. From the diffusion coefficient to the diffusion tensor. *NMR Biomed* 2002;15:431-434.

64. Tuch DS, Reese TG, Wiegell MR, Makris N, Belliveau JW, Wedeen VJ. High angular resolution diffusion imaging reveals intravoxel white matter fiber heterogeneity. *Magn Reson Med* 2002;48:577-582.

65. Tuch DS, Weisskoff RM, Belliveau JW, Wedeen VJ. High angular resolution diffusion imaging of the human brain. In: *Proceedings of the 7th Annual Meeting of ISMRM*, Philadelphia, USA, 1999. p 321.

66. Wedeen VJ, Reese TG, Tuch DS, Weigel MR, Dou J-G, Weiskoff RM, Chesler D. Mapping fiber orientation spectra in cerebral white matter with Fourier transform diffusion MRI. In: *Proceedings of the 8th Annual Meeding of ISMRM*, Denver, USA, 2000. p 82.

67. Wiegell MR, Larsson HB, Wedeen VJ. Fiber crossing in human brain depicted with diffusion tensor MR imaging. *Radiology* 2000;217:897-903.

68. Wedeen VJ, Hagmann P, Tseng WY, Reese TG, Weisskoff RM. Mapping complex tissue architecture with diffusion spectrum magnetic resonance imaging. *Magn Reson Med* 2005;54:1377-1386.

69. Tuch DS, Reese TG, Wiegell MR, Wedeen VJ. Diffusion MRI of complex neural architecture. *Neuron* 2003;40:885-895.

70. Tuch DS. Q-ball imaging. *Magn Reson Med* 2004;52:1358-1372.

71. Alexander DC, Barker GJ, Arridge SR. Detection and modeling of non-Gaussian apparent diffusion coefficient profiles in human brain data. *Magn Reson Med* 2002;48:331-340.

72. Hess CP, Mukherjee P, Han ET, Xu D, Vigneron DB. Q-Ball reconstruction of multimodal fiber orientations using the spherical harmonic basis. *Magn Reson Med* 2006;56:104-117.

73. Tournier JD, Calamante F, Gadian DG, Connelly A. Direct estimation of the fiber orientation density function from diffusion-weighted MRI data using spherical

deconvolution. *Neuroimage* 2004;23:1176-1185.

74. Anderson AW. Measurement of fiber orientation distributions using high angular resolution diffusion imaging. *Magn Reson Med* 2005;54:1194-1206.

75. Anderson AW, Ding Z. Comparison of methods for high angular resolution diffusion imaging. In: *Proceedings of the 12th Annual Meeting of ISMRM*, Kyoto, Japan, 2004. p 1199.

76. Tournier JD, Calamante F, Connelly A. Improved characterisation of crossing fibres: optimisation of spherical deconvolution parameters using a maximum entropy principle. In: *Proceedings of the 13th Annual Meeting of ISMRM*, Miami Beach, USA, 2005. p 384.

77. Tournier JD, Calamante F, Connelly A. Improved characterisation of crossing fibres: spherical deconvolution combined with Tikhonov regularisation. In: *Proceedings of the 14th Annual Meeting of ISMRM*, Seattle, USA, 2006. p 645.

78. Tournier JD, Calamante F, Connelly A. Robust determination of the fibre orientation distribution in diffusion MRI: non-negativity constrained super-resolved spherical deconvolution. *Neuroimage* 2007;35:1459-1472.

79. Sakaie KE, Lowe MJ. An objective method for regularization of fiber orientation distributions derived from diffusion-weighted MRI. *Neuroimage* 2007;34:169-176.

80. Hansen PC. Regularization tools: a Matlab package for analysis and solution of discrete ill-posed problems. *Numer Algorithms* 1994;6:1–35.

81. Clark CA, Le Bihan D. Water diffusion compartmentation and anisotropy at high b values in the human brain. *Magn Reson Med* 2000;44:852-859.

82. Le Bihan D. Molecular diffusion, tissue microdynamics and microstructure. *NMR Biomed* 1995;8:375-386.

83. Mulkern RV, Gudbjartsson H, Westin C-F, Zengingonul HP, Gartner W, Guttmann CRG, Robertson RL, Kyriakos W, Schwartz R, Holtzman D, Jolesz FA, Maier SE.

Multi-component apparent diffusion coefficients in human brain. *NMR Biomed* 1999;12:51-62.

84. Mulkern RV, Vajapeyam SV, Robertson RL, Caruso PA, Rivkin MJ, Maier SE. Biexponential apparent diffusion coefficient parameterization in adult vs newborn brain. *Magn Reson Imaging* 2001;19:659-668.

85. Niendorf T, Dijkhuizen RM, Norris DG, van Lookeren Campagne M, Nicolay K. Biexponential diffusion attenuation in various states of brain tissue: Implications for diffusion-weighted imaging. *Magn Reson Med* 1996;36:847-857.

86. Clark CA, Hedehus M, Moseley ME. In vivo mapping of the fast and slow diffusion tensors in human brain. *Magn Reson Med* 2002;47:623-628.

87. Maier SE, Vajapeyam SV, Mamata H, Westin C-F, Jolesz FA, Mulkern RV. Biexponential diffusion tensor analysis of human brain diffusion data. *Magn Reson Med* 2004;51:321-330.

88. Jeong H-K, Anderson AW. Measurement of intrinsic fiber diffusivity using spherical deconvolution of high angular resolution diffusion data. In: *Proceedings of the 15th Annual Meeting of ISMRM*, Berlin, Germany, 2007. p 905.

89. Mukherjee P, Hess CP, Xu D, Han ET, Kelley DA, Vigneron DB. Development and initial evaluation of 7-T q-ball imaging of the human brain. *Magn Reson Imaging* 2008;26:171-180.

90. Reischauer C, Jaermann T, Staempfli P, Pruessmann KP, Thompson MR, Beosiger P. 16-Channel parallel DTI at 7T: Initial Experiments. In: *Proceedings of the 15th Annual Meeting of ISMRM*, Berlin, Germany, 2007. p 3539.

91. Wiggins CJ, Benner T, Wiggins GC, Triantafyllou C, Wald L. In-vivo, human diffusion tensor imaging at 7T: First results. In: *Proceedings of the 15th Annual Meeting of ISMRM*, Berlin, Germany, 2007. p 1497.

92. Xu D, Han ET, Hess CP, Kelley DA, Vigneron DB, Metcalf M, Mukherjee P. 7T diffusion tensor imaging and Q-ball imaging of the human brain in vivo. In:

Proceedings of the 15th Annual Meeting of ISMRM, Berlin, Germany, 2007. p 1466.

93. Chang H, Fitzpatrick JM. A technique for accurate magnetic resonance imaging in the presence of field inhomogeneities. *IEEE T Med Imaging* 1992;11:319-329.

94. Bowtell RW, McIntyre DJO, Commandre M-J, Glover PM, Mansfield P. Correction of geometric distortion in echo planar images. In: *Proceedings of the 2nd Annual Meeting of ISMRM*, San Francisco, USA, 1994. p 411.

95. Morgan PS, Bowtell RW, McIntyre DJO, Worthington BS. Correction of spatial distortion in EPI due to inhomogeneous static magnetic fields using the reversed gradient method. *J Magn Reson Imaging* 2004;19:499-507.

96. Andersson JLR, Skare S, Ashburner J. How to correct susceptibility distortions in spin-echo echo-planar images: application to diffusion tensor imaging. *Neuroimage* 2003;20:870-888.

97. Jezzard P, Balaban RS. Correction for geometric distortion in echo planar images from B0 field variations. *Magn Reson Med* 1995;34:65-73.

98. Vaughan JT, Garwood M, Collins CM, Liu W, DelaBarre L, Adriany G, Andersen P, Merkle H, Goebel R, Smith MB, Ugurbil K. 7T vs. 4T: RF power, homogeneity, and signal-to-noise comparison in head images. *Magn Reson Med* 2001;46:24-30.

99. Adriany G, Van de Moortele PF, Wiesinger F, Moeller S, Strupp JP, Andersen P, Snyder C, Zhang X, Chen W, Pruessmann KP, Boesiger P, Vaughan T, Ugurbil K. Transmit and receive transmission line arrays for 7 Tesla parallel imaging. *Magn Reson Med* 2005;53:434-445.

100. Bammer R, Markl M, Barnett A, Acar B, Alley MT, Pelc NJ, Glover GH, Moseley ME. Analysis and generalized correction of the effect of spatial gradient field distortions in diffusion-weighted imaging. *Magn Reson Med* 2003;50:560-569.

101. Johnson RA, Wichern DW. *Applied multivariate statistical analysis*, 4th ed. New Jersey: Prentice Hall; 1998. pp160-164.

102. Jackson JE. *A user's guide to principal components*. New York: John WiIey & Sons; 1991. p 33.

103. Mardia KV. Measures of multivariate skewness and kurtosis with applications. *Biometrika* 1970;57:519-530.

104. Mardia KV, Kent JT, Bibby JM. *Multivariate analysis*. New York: Academic Press; 1979. p 148.

105. Papadakis NG, Xing D, Huang CL-H, Hall LD, Carpenter A. A comparative study of acquisition schemes for diffusion tensor imaging using MRI. *J Magn Reson* 1999;137:67-82.

106. Wolfram S. *The Mathematica Book*, 3rd ed. Champaign, IL: Wolfram Media/Cambridge University Press; 1996.

107. Westin C-F, Peled S, Gudbjartsson H, Kikinis R, Jolesz FA. Geometrical diffusion measures for MRI from tensor basis analysis. In: *Proceedings of the 5th Annual Meeting of the ISMRM*, 1997, Vancouver, Canada, 1997. p 1742.

108. Lu Y, Aldroubi A, Gore JC, Anderson AW, Ding Z. Improved fiber tractography with Bayesian tensor regularization. *Neuroimage* 2006;31:1061-1074.

109. Mori S, Barker PB. Diffusion magnetic resonance imaging: its principle and applications. *Anat Rec* 1999;257:102-109.

110. Aster R, Borchers B, Thurber C. *Parameter estimation and inverse problems*. Burlington: Elsevier Academic Press; 2005.

111. Ritchie DW, Kemp GJL. Fast computation, rotation and comparison of low resolution spherical harmonic molecular surfaces. *J Comput Chem* 1999;20:383-395.

112. Hendriks H. Nonparametric estimation of a probability density on a Riemannian manifold using Fourier expansions. *Ann Stat* 1990;18:832-849.

113. Descoteaux M, Angelino E, Fitzgibbons S, Deriche R. Apparent diffusion coefficients from high angular resolution diffusion imaging: estimation and applications. *Magn Reson Med* 2006;56:395-410.

114. Descoteaux M, Angelino E, Fitzgibbons S, Deriche R. Regularized, fast, and robust analytical Q-ball imaging. *Magn Reson Med* 2007;58:497-510.

115. Bossart EL, Inglis BA, Buckley DL, Wirth Ⅲ ED, Mareci TH. Multiple component diffusion tensor imaging in excised fixed CNS tissue. In: *Proceedings of the 7th Annual Meeting of ISMRM*, Philadelpia, USA, 1999. p 328.

116. Schmahmann JD, Pandya DN, Wang R, Dai G, D'Arceuil HE, de Crespigny AJ, Wedeen VJ. Association fibre pathways of the brain: parallel observations from diffusion spectrum imaging and autoradiography. *Brain* 2007;130:630-653.

117. Perrin M, Poupon C, Cointepas Y, Rieul B, Golestani N, Pallier C, Riviere D, Constantinesco A, Le Bihan D, Mangin JF. Fiber tracking in q-ball fields using regularized particle trajectories. *Lect Notes Comput Sc: Inform Process Med Imaging* 2005;19:52-63.

118. Kaden E, Knosche TR, Anwander A. Parametric spherical deconvolution: inferring anatomical connectivity using diffusion MR imaging. *Neuroimage* 2007;37:474-488.

119. Behrens TE, Woolrich MW, Jenkinson M, Johansen-Berg H, Nunes RG, Clare S, Matthews PM, Brady JM, Smith SM. Characterization and propagation of uncertainty in diffusion-weighted MR imaging. *Magn Reson Med* 2003;50:1077-1088.

120. Jones DK, Simmons A, Williams SC, Horsfield MA. Non-invasive assessment of axonal fiber connectivity in the human brain via diffusion tensor MRI. *Magn Reson Med* 1999;42:37-41.

121. Hutton C, Bork A, Josephs O, Deichmann R, Ashburner J, Turner R. Image distortion correction in fMRI: A quantitative evaluation. *Neuroimage* 2002;16:217-240.

122. Jezzard P, Barnett AS, Pierpaoli C. Characterization of and correction for eddy current artifacts in echo planar diffusion imaging. *Magn Reson Med* 1998;39:801-812.

123. Reese TG, Heid O, Weisskoff RM, Wedeen VJ. Reduction of eddy-current-induced distortion in diffusion MRI using a twice-refocused spin echo. *Magn Reson Med* 2003;49:177-182.

124. Rohde GK, Barnett AS, Basser PJ, Marenco S, Pierpaoli C. Comprehensive approach for correction of motion and distortion in diffusion-weighted MRI. *Magn Reson Med* 2004;51:103-114.

125. Cusack R, Brett M, Osswald K. An evaluation of the use of magnetic field maps to undistort echo-planar images. *Neuroimage* 2003;18:127-142.

126. Lee J, Lazar M, Lee J, Holden J, Terasawa-Grilley E, Alexander AL. Correction of B0 EPI distortions in diffusion tensor imaging and white matter tractography. In: *Proceedings of the 12th Annual Meeting of ISMRM*, Kyoto, Japan, 2004. p 2172.

127. Maes F, Collignon A, Vandermeulen D, Marchal G, Suetens P. Multimodality image registration by maximization of mutual information. *IEEE T Med Imaging* 1997;16:187-198.

128. Wakana S, Jiang H, Nagae-Poetscher LM, van Zijl PC, Mori S. Fiber tract-based atlas of human white matter anatomy. *Radiology* 2004;230:77-87.

129. Batchelor PG, Atkinson D, Hill DL, Calamante F, Connelly A. Anisotropic noise propagation in diffusion tensor MRI sampling schemes. *Magn Reson Med* 2003;49:1143-1151.